BNWL-235-3

AEC
RESEARCH
and
DEVELOPMENT
REPORT

PACIFIC NORTHWEST LABORATORY ANNUAL REPORT FOR 1965 IN THE PHYSICAL SCIENCES to the USAEC Division of Biology and Medicine VOLUME 3: EARTH SCIENCES

MAY, 1966

BATTELLE-NORTHWEST

BATTELLE MEMORIAL INSTITUTE / PACIFIC NORTHWEST LABORATORY

LEGAL NOTICE

PACIFIC NORTHWEST LABORATORY
RICHLAND, WASHINGTON
operated by
BATTELLE MEMORIAL INSTITUTE
for the
UNITED STATES ATOMIC ENERGY COMMISSION UNDER CONTRACT AT(45-1)-1830

BNWL-235 3
UC-48
Biology and Medicine

PACIFIC NORTHWEST LABORATORY

ANNUAL REPORT FOR 1965

IN THE PHYSICAL SCIENCES

to the

USAEC Division of Biology and Medicine

VOLUME 3: EARTH SCIENCES

By

Staff Members of
Environmental and Radiological Sciences Department
Earth Sciences Section

Edited by
D. W. Pearce and J. K. Green

May, 1966

PACIFIC NORTHWEST LABORATORY
RICHLAND, WASHINGTON

Printed in USA. Price $3.00. Available from the
Clearinghouse for Federal Scientific and Technical Information,
Rational Bureau of Standards
U.S. Department of Commerce, Springfield, Virginia

TABLE OF CONTENTS

TABLE OF CONTENTS (Contd)

PACIFIC NORTHWEST LABORATORY
ANNUAL REPORT FOR 1965
IN THE PHYSICAL SCIENCES

VOLUME 3: EARTH SCIENCES

GEOLOGY AND HYDROLOGY

THE STRATIGRAPHY OF THE UPPERMOST PART OF THE BASALT SEQUENCE AND ITS IMPLICATIONS— R. E. Brown

The stratigraphy of the basalt sequence was carried beneath the Hanford nrea and into the Rattlesnake No. 1 well of the standard Oil Company of California to a depth of 1000 ft. Region-wide data then further confirmed two Oregon sources of the basalt flows. Diversion and ponding of the Columbia River by flows encroaching on it from the southeast were important in the deposition of beds (now aquifers) of the Beverly Member of the Ellensburg Formation. Anticlinal ridges began to rise at various times to affect the Columbia River course, the deposition of its sediments, and the extent of the basalt flows. Knowledge of tho stratigraphy permits determination of the hydrologic characteristics of the basalt sequence and of individual aquifers. The feasibility of disposal or storage of wastes with maximum safety in the basalt can, in turn, be bettar appraised.

Regional geologic studies continued to determine the extent and continuity of the stratigraphic units of the basalt sequence beneath the Hanford area and their characteristics from place to place. Waste waters in the uppermost confined aquifer in the sequence (the upper part of the Beverly Member) and interest in possible storage of wastes thousands of feet deep in the basalt have increased the need Tor better knowledge of the sequence and the occurrence and movement of water within it.

The defined stratigraphic section of the uppermost 1000 ft of the sequence was carried beneath the Manford area from the very recently completed work of others in adjoining areas on opposite sides of Hanford. Fifteen basalt flows and sedimentary interbeds between flows constitute that part of the section. Four of these units are significant aquifers that are used in some sites for water supplies.

An isopach map of the Priest Rapids Member (four basalt flows) was constructed covering about 6000 mi^2 in which thicknesses are available. The sequence steadily and rapidly thickens southward from Hanford and, together with known cast and west limits of the member, indicates northward movernent from sources in north central Oregon. The member is generally a poor aquifer,

and that only where the flows are highly altered in as-yet undetermined regional patterns. Knowledge of its source and thickness trends now permits improved estimates of its thickness and continuity at sites where it cannot be observed, such as beneath the Hanford area.

Above the Priest Rapids Member are the stream-deposited sediments of the Beverly Member of the Ellensburg Formation. Figure 1 shows the generalized piezometric heads encountered in the upper part of the Beverly Member aquifer and indicated directions of flow. The sand and gravel portion of the bed represents a main stream deposit of the Columbia River. The sediments become finer-grained and generally thinner away from the gravel zone, grade into silts and clays, then pinch out. Ground water flow directions, flow rates and flow volumes are the integrated effects of aquifer thickness (not shown), the lithology (the permeable gravel versus the less permeable silt and clay), structure (the folded aquifers), current sites of natural and artificial recharge, and the respective amounts of recharge at various sites. Waste waters entering the aquifer in the middle of the map area on the Hanford Project probably migrate into an overlying highly jointed basalt flow as they move southeastward toward steadily less permeable sediments and a thinner bed. Entrance into the Columbia River probably occurs near the Snake River junction (just southeast of the map area) over a widely dispersed area.

In part intercalated within and in part overlying the Beverly Member beds are basalt flows of the Saddle Mountains Member that, according to the recent work of others, originated in northeastern Oregon and spread westward to northwestward across central Washington. They thus moved nearly at right angles to the direction of the earlier Priest Rapids flows and encroached upon the Columbia River to force its course farther westward. The south to southwestward course of the Columbia River from Hanford, indicated by the Beverly Member bed, appears to be due to the northwestward land surface gradient imposed by the encroaching lava flows. The youngest flow of the member beneath Hanford is the Elephant Mountain flow through which the waste waters evidently ultimately move.

The earliest sediments of the Ringold Formation were deposited in a shallow lake, probably caused by ponding of the Columbia River by flows of the Saddle Mountains Member later than those diverting the river in Beverly Member time. Anticlinal uplift of the Horse Heaven Hills, classically believed to have caused deposition of the entire Ringold Formation, now appears to have begun subsequent to deposition of the lowermost sediments.

Anticlinal uplift evidently began at different times in the different ridges and possible in different parts of the same ridges, as indicated by the distribution of flows and sediments over the ridges. In the Pasco Basin, Umtanum Ridge began the rise,

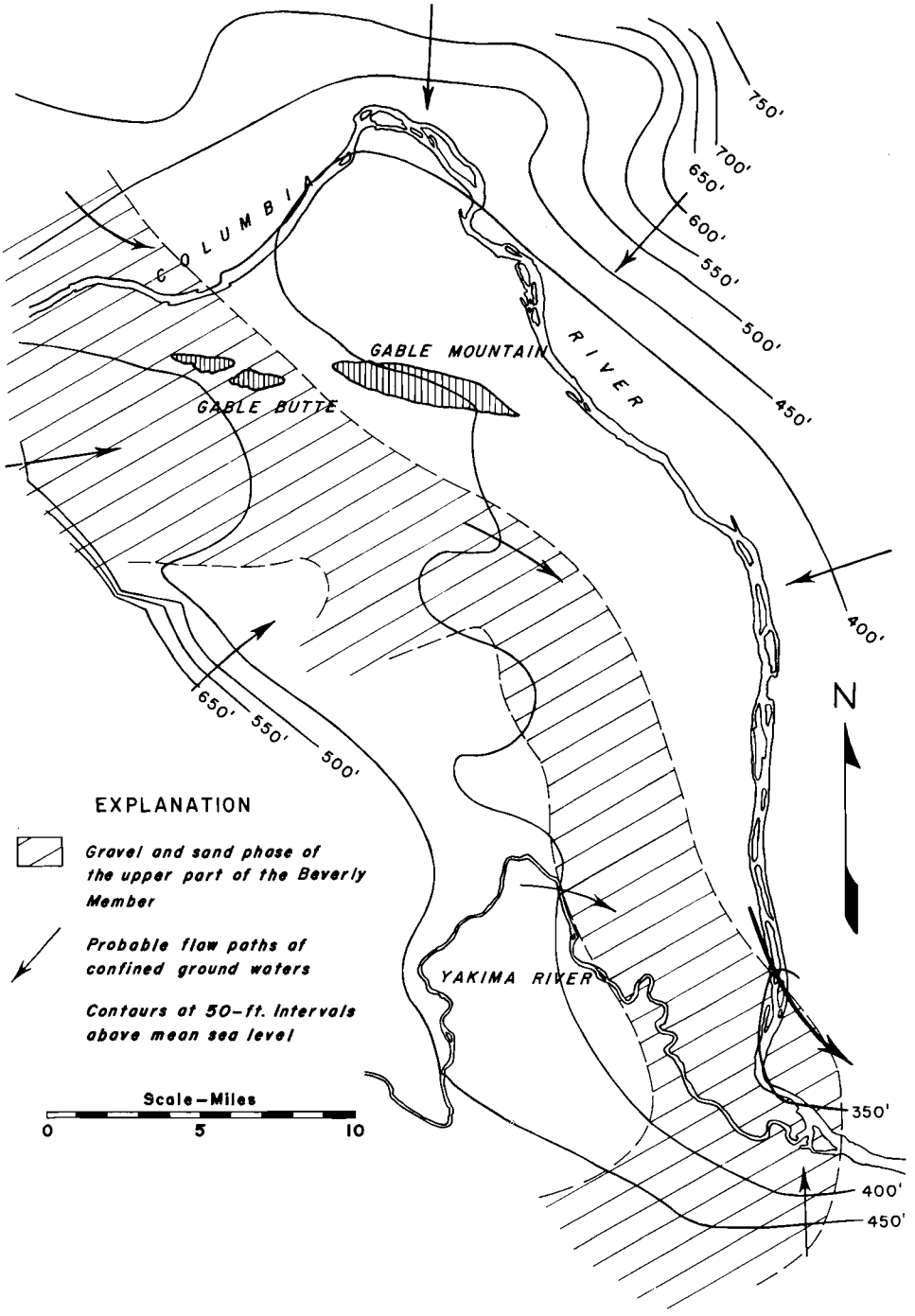

FIGURE 1. Generalized Piezometric Heads in the Upper Part of the Beverly Member, Pasco Basin, Washington

followed by Rattlesnake Hills, Yakima Ridge, and the Saddle Mountains (at about the same time), and lastly by Horse Heaven Hills. Uplift thus may have progressed southward although whether the progression continued into Oregon and is significant, is problematical.

Purchase of three highly sensitive strong-motion type seismographs was authorized during the year. The use of these instruments will help answer earthquake engineering problems and dedetermine the seismic characteristics of the region. With detailed knowledge of the regional geology and geologic history they well may lead to improved knowledge of origin and development.

Drilling of deep irrigation wells for ranches west of Hanford provided abundant samples of the basalt sequence to a depth of 1700 ft. Those samples and other available information permitted resolution of the stratigraphy in the Standard Oil Company of California Rattlesnake No. 1 test well to 1000 ft depth, The reservoir rock in the Rattlesnake Hills Gas Field was determined to be Sand Hollow basalt flow of the Frenchman Springs Member, and the cap rock is the Squaw Creek bed of altered volcanic tuff. In other sites the Sand Hollow basalt flow is an important aquifer.

Resolution is anticipated of the stratigraphic sequence in the Rattlesnake No. 1 well to considerably more than 1000 ft to which it has been identified.

VARIATIONS IN THE EARTH'S GRAVITY FIELD AT HANFORD— D. E. Peterson

Several hundred measurements of the acceleration of gravity were made to determine the nature of the gravity field in the Hanford area. Observed values range from 980.4786 cm/sec^2, at the point of highest altitude in the Rattlesnake Hills, to 980.7120 cm/sec^2 at the horn of the Columbia River. Bouguer anamalies reduced from the observed values are being correlated with geologic information, including depth to basalt, to obtain a more complete picture of the geologic environment at Hanford. In 1965, dense basalt was encountered by a drill approximately 170 ft above the depth at which basalt normally occurs in section 2 of T12N, R26E. Gravity observations compared with gravity values from a theoretical model of a basalt high indicate that a field of large boulders is the probable explanation for the anomalous basalt.

A study of the earth's gravity field in the Hanford area was begun in October, 1965. Because a well defined bedrock surface is required for utilization of existing three-dimensional computer programs for the prediction of ground water movement within the area, the primary goal of the survey was to supplement available geologic information to improve the contour map of the basalt bedrock. The success of this undertaking was predicated upon information from well logs which indicated that a relatively constant density difference of 0.8 exists between the sed-

imentary deposits and the underlying basalt flows. Bouguer anomalies, which are differences between the observed and the theoretical values of the acceleration of gravity at a given point (the observed gravity is adjusted to sea level datum), are of particular value in delineating variations in density within the earth's crust.

The observed gravity survey was completed in January, 1966, with a precision of 10^{-7} normal gravity. The data were collected with a gravimeter yielding relative values; however, the values were converted to an absolute base by a tie between the local base station at the Richland, Washington, Airport (g = 980.6724 cm/sec^2) and an international gravity network station at the Pendleton, Oregon, Airport (g = 980.51118 cm/sec^2). The absolute acceleration of gravity in the Hanford area ranges from 980.4786 cm/sec^2 at the point of greatest altitude (3581 ft, T11N, R25E, Section 25) in the Rattlesnake Hills to 980.7120 cm/sec^2 at the horn of the Columbia River (380 ft, T14N, R26E, Section 12). Theoretical gravity is obtained from the International formula of 1930. This and other semiempirical expressions for normal gravity at sea level stem from a derivation (neglecting infinitesimals of greater than second order) by early geodesists based upon the assumptions that the mass of the earth is concentrated at its center, that the surface is an equipotential (niveau) surface, and that the earth behaves as a nonrigid body with the same general density distribution as the real earth. The resulting equation is of the form:

$$g_\psi = g_e (1 + \beta \sin^2 \psi + \varepsilon \sin^2 2\psi) \quad \ldots (1)$$

where: g_ψ = acceleration of gravity at any given latitude

g_e = acceleration of gravity at the equator

ψ = latitude

β = gravitational flattening of the earth

ε = a coefficient which is a function of the geometric flattening of the earth, the equatorial centrifugal acceleration, and the equatorial gravity.

The international formula, Equation (2), which was adopted by the International Geodetic and Geophysical Union in 1930, is the variation of Equation (1) that is presently applied in most gravity analyses:

$$g_\psi = 978.0490(1 + 0.0052884 \sin^2\psi - 0.0000059 \sin^2 2\psi). \quad (2)$$

In the Hanford area, Bouguer anomalies of approximately -50 ± 5 milligals (1 milligal = 10^{-3} cm/sec^2) are observed. These values primarily reveal deeply seated variations within the earth's crust, e.g., the nature of the Mohorovicic Discontinuity. The local anomalies, those within the ± 5 milligal range, are currently being computed and will help determine the configuration of the basalt bedrock.

In 1965, a drilling rig operating in Section 2 of T12N R26E encountered dense basalt approximately 330 ft below land surface. Basalt had been encountered at 500 ft in a well 600 ft to the south, and another well, 300 ft to the north, was bottomed in clay at 400 ft. Evidence from other wells dril-

led in the vicinity indicated that the basalt surface locally had an aproximately uniform dip of 1° toward the south. This newer information indicated that either a small buried hill existed at the well site or that the anomalous basalt was due to a lens of large boulders. To test the hypothesis of a buried hill a theoretical model was constructed, which consisted of three spherical masses, each 50 ft diam, stacked so that they formed a 150 ft body, the crown of which was 350 ft below land surface. A density differential of 0.8 was assumed between the basalt and the ambient sediments. The resulting calculations indicated that a maximum gravity anomaly of 0.2 milligal could be expected directly above the hypothetical mass. The effect of the body was less than 0.02 milligal at 1000 ft. A 2200 ft north-south gravity traverse, with 100 ft spacing between stations, was established to ascertain the nature of the gravity field near the well. Station 14 (1400 ft from the south end of the traverse) was located near the well. The resulting Bouguer anomalies ranged from -51.7 milligal at the north end of the line to -52.7 milligal at the south end. Variations about a uniform trend were 0.1 milligal or less. These variations were within the resolution imposed upon the survey by an uncertainty of approximately 2.0 ft in altitude control. The results indicate that it is unlikely that a hill of these dimensions exists on the buried basalt slope, because the 0.2 milligal maximum to be expected from the feature was not observed near the well itself. No statement can presently be made (based on gravity data alone) concerning the existence of a hill with the same 150 ft vertical dimension but with a small diameter, since the gravitational effect of such a body would be less than the resolution (0.1 milligal) of the observed anomalies. However, improved altitude control is being secured which will reduce the resolution limitation to 0.01 milligal.

Aside from the primary purpose of this study, these gravity data are of value where instrumental accuracy depends upon a precise determination of the absolute acceleration of gravity. If the location and altitude of an instrument are known (this applies to the Hanford area only) it should be possible to calculate the gravity at the point to 10^{-6} normal gravity. An exception to this would be instruments situated on steep slopes; 10^{-5} accuracy or better could be expected at these locations. The data are also of importance for studies of the earth's crust in that few gravity measurements have been obtained previously from south-central Washington. Determination of major structural trends, deviations from isostatic equilibrium, and deflection of vertical determinations are examples of crustal studies that depend upon an accumulation of gravity data.

PREDICTION OF VERTICAL INFILTRATION AS INFLUENCED BY ERRORS IN MEASURING CAPILLARY PRESSURE— L. G. King

The soil characteristics (permeability, capillary pressure, and saturation) measured during steady flow or equilibrium conditions were used to solve the one-dimensional, transient boundary-value problems for vertically downward flow during infiltration. The calculated results were compared with experimental data from actual transient flow columns. Predicted and experimental results agreed very well after the capillary pressure values of the measured permeability and capillary pressure relationship were corrected for manometer errors.

The transient flow of liquid through a partially saturated porous medium is described by the partial differential equation,

$$\text{div}\ (D\ \text{grad}\ S) + \frac{\rho g}{\mu\phi}\frac{\partial k}{\partial z} = \frac{\partial S}{\partial t} \qquad (1)$$

where:

$$D = -\frac{k}{\mu\phi}\frac{dp_c}{dS} \qquad (2)$$

Both the diffusivity, D, and the permeability, k, are functions of the saturation, S. The ability (or inability) of this equation to predict experimentally measured results has been the subject of considerable research over the past 2 decades. If the equation actually describes the physical flow, then the diffusivity can be calculated [by Equation (2)] as a function of S from the product of the slope of the saturation-capillary pressure relationship and the permeability at each value of saturation.

For this study, all measurements were made during imbibition[1] with Soltrol C* as the liquid. The word "imbibition" is used to denote a history such that any change of saturation is an increase of saturation and does not specify whether the present state flow is steady or transient. The measurements of permeability as a function of capillary pressure were made during steady downward flow,[1] while the saturation-capillary pressure relationships were measured on separate small samples during equilibrium conditions.[1] These data were used to calculate the diffusivity and permeability as functions of saturation for use as input to Philip's[2-4] methods for solving Equation (1) together with the appropriate boundary conditions.

For the transient flow measurements, a column of 1 cm lengths of plastic cyclinder was taped together and packed with an air-dry soil. During any one run, the saturation at the top of the column was held constant by maintaining a constant capillary pressure at the inflow barrier through which the liquid entered the column. At time t = 0, the inflow barrier was brought into contact with the soil. Simultaneous observations were made of the downward advance of the (visual) wetted front, the volume of liquid inflow, and the time. When the wetted front was still several centimeters from the dry end of the column, the flow was

*A core test fluid obtained from Phillips Petroleum Company.

stopped and the column was immediately sectioned into 1 cm lengths and weighed to determine the saturation profile at that time.

After all experimental data were collected, it was discovered that the type of manometers used to measure capillary pressure for the permeability-capillary pressure relationships could have caused the measured values of capillary pressure to have been as much as 2 mbars less than the true values. The nature of the manometer error is such that the error is expected to be greater for coarse-textured soils than for fine-textured soils. The capillary pressure values were adjusted by adding a constant to each observed P_C value. Figure 2 shows a 0.55 mbar adjustment for Crab Creek sand and no adjustment for G. E. No. 2 sand. The curves of Figure 2, together with the curves of Figure 3 of King [5] were used for input for all the transient flow calculations.

Figure 3 shows the comparison of calculated and measured saturation profiles. Figures 4 and 5 show the elevation of wetted front and the accumulated volume of inflow as functions of time since the flow began. Figures 3 and 5 show that the 0.55 mbar adjustment of P_C values gives good agreement between calculated and measured results for Crab Creek sand. The value t_A is the time at which the exponential equation [4] replaced the series solution for infiltration rate; the + designations on Figures 4 and 5 show the value of time near which a minimum in the series solution for infiltration rate occurred

It is concluded that Equation (1) does adequately describe the vertical infiltration of liquid into relatively dry soil. Extreme care should be taken in measuring the soil characteristics, especially capillary pressure, since a small error in capillary pressure can cause a large error in predicted flow results.

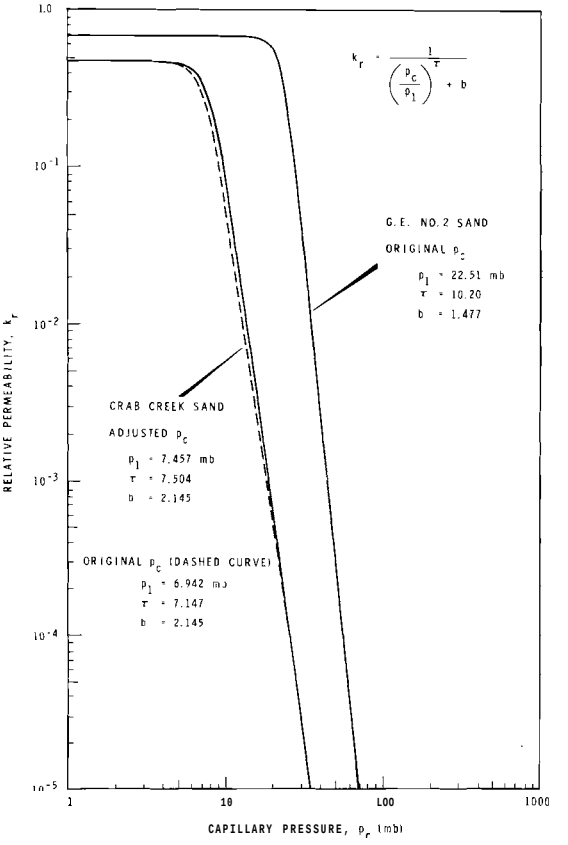

FIGURE 2. Relative Permeability as a Function of Capillary Pressure.

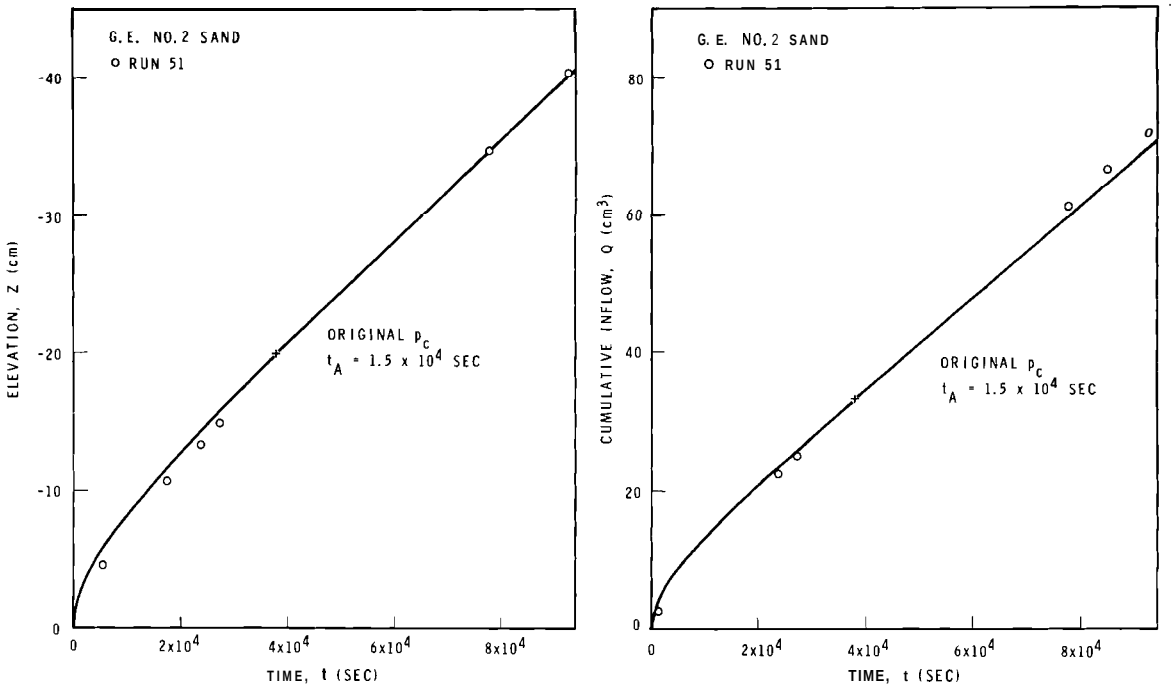

FIGURE 3. Comparison of Calculated and Measured Saturation Profiles Showing Effects of Adjusted p_c on the Calculated Values

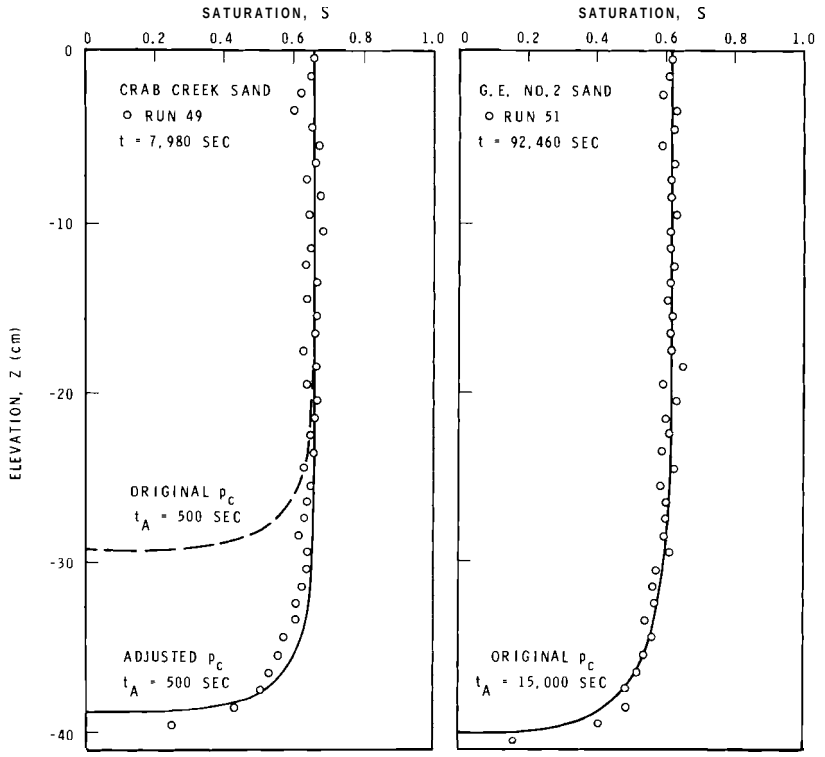

FIGURE 4. Evaluation of Wetted Front and Cumulative Inflow as Functions of Time for G.E. No. 2 Sand

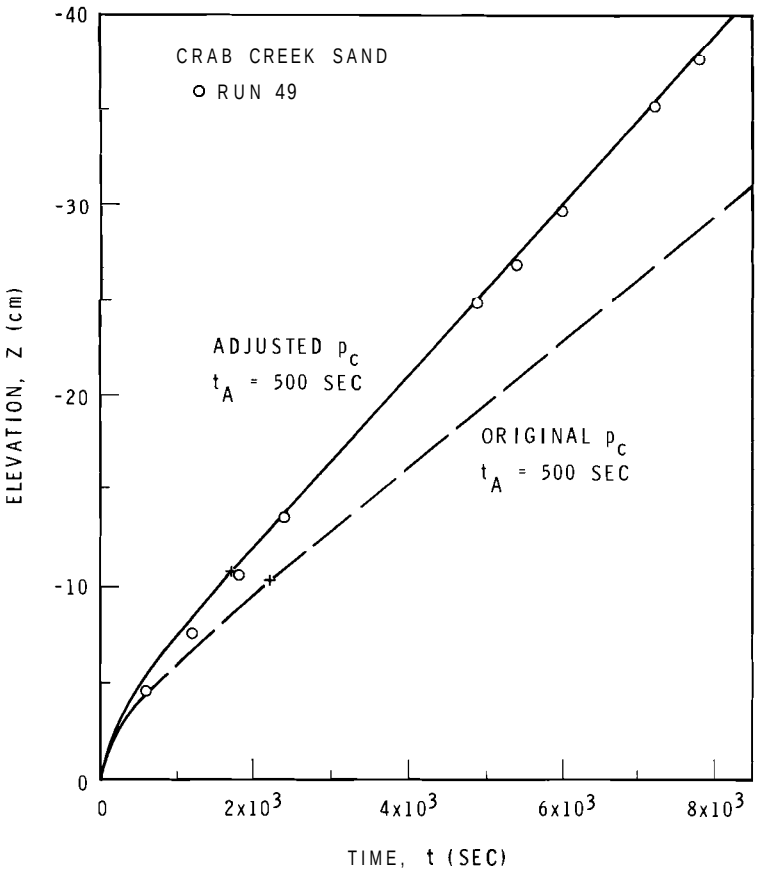

FIGURE 5. Elevation of Wetted Front as a Function of Time for Crab Creek Sand

HORIZONTAL INFILTRATION OF LIQUIDS INTO POROUS SOLIDS - L. G. King

The diffusivity functions computed from steady flow and equilibrium measurements of permeability, capillary pressure, and saturation were used to solve the one-dimensional, transient boundary value problems for horizontal flow during infiltration. Strictly linear flow in the horizontal direction cannot occur even for samples which are quite thin in the vertical direction. In the actual physical system, vertical components of flow do exist. The importance of the vertical components is greater for coarse-textured soils than for fine-textured soils.

For transient flow of liquid through a partially saturated medium in the horizontal direction only, the equation[6] describing the flow reduces to

$$\frac{\partial}{\partial x}\left(D\,\frac{\partial S}{\partial x}\right) = \frac{\partial S}{\partial t} \qquad (1)$$

where the diffusivity, D, is a function of the saturation, S. The diffusivity[6] was used as input to Philip's method for solving Equation (1) together with the appropriate boundary conditions. The calculated results were

compared with experimental data from actual transient systems.

For the transient flow measurements, plastic cylinders *3.2* cm diam were packed with air-dry soil and placed with their axes horizontal. During any one p_c difference, S cannot be constant in the centerline of the inflow barrier was held constant. At time t = 0, the inflow barrier was brought into contact with the end of the soil sample. When the wetted front was still several centimeters from the dry end of the sample, the flow was stopped and the cylinder was immediately sectioned into 1 cm lengths and weighed to determine the distribution of saturation at that time.

Figure 6 compares experimental and calculated results for Crab Creek sand and G. E. No. 2 sand. The abscissa, λ, is the Boltzmann transformation variable: $\lambda = x/\sqrt{t}$, where x is the horizontal distance from the inflow barrier to a particular value of S, and t is time since contact of inflow barrier and soil. Each calculated curve assumes strictly linear flow with a boundary saturation given by the indicated value at $\lambda = 0$, i.e., at the inflow barrier. That the boundary saturation is not constant with vertical depth of sample is immediately evident. For the liquid[6] used, the 3.2 cm vertical depth corresponds to a p_c difference from top to bottom of the sample equal to nearly 2.4 mbars. From Figure 7 it is seen that for this much p_c difference, S cannot be constant in the vertical direction. Linear flow could still be possible if this static equilibrium p_c difference would be maintained throughout the length of the wetted sample. That this is not the, case will be shown below.

If strictly linear horizontal flow exists, it is possible to calculate separately the flow in any horizontal lamina independent of any other horizontal lamina. Saturation distributions calculated for three such laminas (top, centerline, and bottom of sample) are shown in Figure 6. For Crab Creek sand, the distributions were calculated using the p_c values adjusted for manometer errors.[6] The flow is not adequately predicted by using the boundary saturation at the centerline of the sample; this calculated distribution lags the experimental distribution for both soils.

For strictly linear horizontal flow, the vertical component of the gradient of potential must equal zero everywhere throughout the sample. From Figures 6 and 7 the vertical component was calculated as a function of λ by taking differences over the *3.2* cm distance from top to bottom of the sample. The horizontal component was calculated along the centerline as a function of λ using a 3 cm distance centered on each value of λ. A measure of the tendency for vertical flow is given by ratio of vertical to horizontal components of

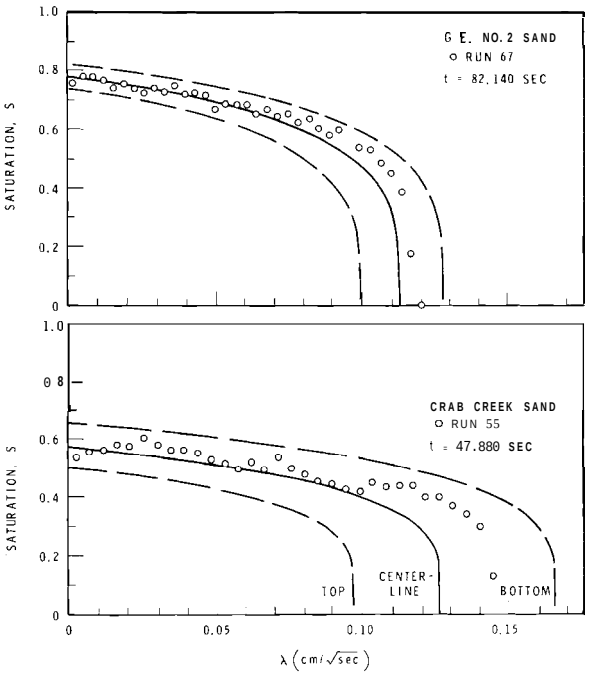

FIGURE 6. Experimental Saturation Distributions Compared to Distributions Calculated on the Assumption of Strictly Linear Horizontal Flow

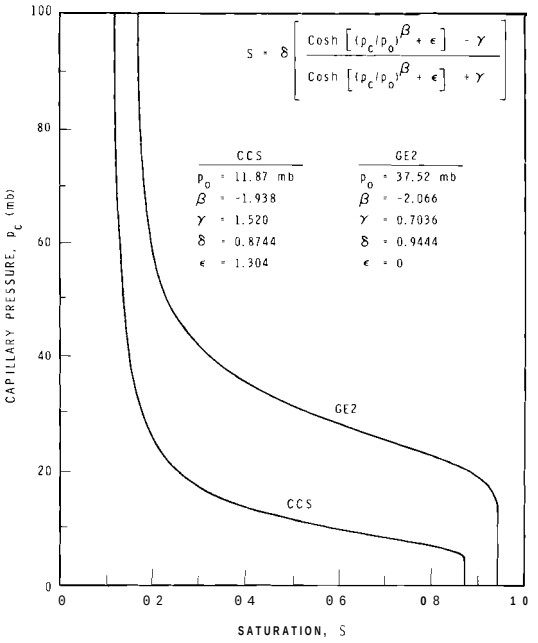

FIGURE 7. Saturation as a Function of Capillary Pressure

the gradient of potential. Such ratios calculated for t = 10^4 sec are shown in Figure 8. That is, if strictly linear horizontal flow could have occurred until 10^4 sec, conditions shown in Figure 8 would exist. Of course, in the actual flow system, the vertical components of flow would already have raised the saturation of the upper parts of the sample beyond the saturation given by linear flow. Hence, the entire wetted front would advance faster than predicted by linear horizontal flow with the boundary saturation at the centerline of the sample. Thus a contradiction is reached, and the assumption of strictly linear horizontal flow in such a system is invalid. Figure 8 shows that the tendency for upward flow is from three to four times more important in Crab Creek sand than in G. E. No. 2 sand. This explains why the results of Figure 6 agree more closely for the latter than for the former.

It is concluded that for precise prediction of the experimental flow system described herein, the boundary value problem must be solved in three space dimensions. If a rectangular rather than circular cross-section were used, the problem could be solved in two space dimensions. Methods of measuring soil characteristics based on linear horizontal flow systems can be significantly in error if the soil is coarse-textured and (or) the vertical depth is too large.

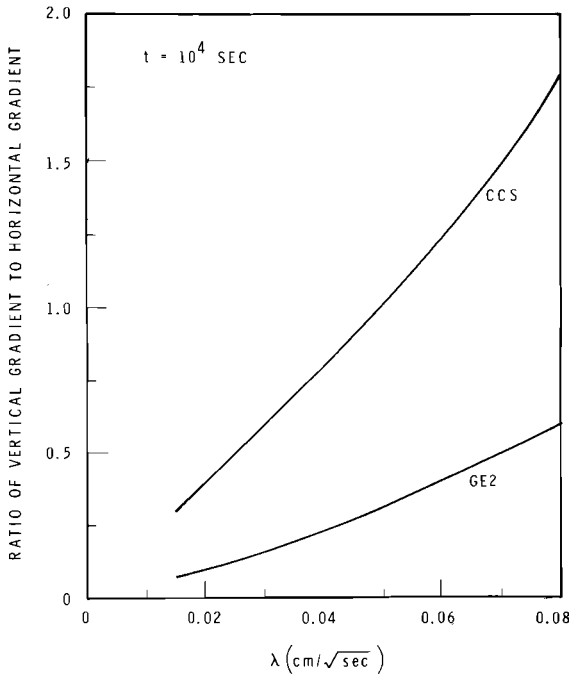

FIGURE 8. Ratios of Vertical to Horizontal Components of Potential as Functions of λ for t = 10^4 sec

"STREAM," A GENERAL ROUTINE FOR GETTING STEADY GROUND WATER FLOW PATHS AND TRAVEL TIMES— R. W. Nelson

A computer program is briefly described which uses the equations derived previously for streamlines in heterogeneous madia to provide useful results for waste transport analysis. The program generates paths of flow, determines the permeability along each path, gives the associated travel times for a very wide class of flow problems in porous media. Tests of the accuracy of the numerical results have indicated that very satisfactory answers are obtained with the programs.

In waste transport studies, the paths of ground water flow and times of travel along those paths are fundamental to an overall analysis.[7] Any method for determining this information must be very flexible in view of the variety of practical problems encountered. Earlier theoretical work[8] on steady paths of flow for heterogeneous media resulted in a general formulation for writing of the computer program capable of providing numerically the information needed for waste transport predictions. The programs have been prepared in Fortran 4 and are operational on the IBM 7090 and Univac 1107. Two programs were prepared, one for two-dimensional problems and the other for three-dimensional. Fundamentally, the programs are the same and were written separately only to save computing time for the former case.

Once the required starting coordinates, permeabilities, and potential functions, i.e., the potential equation and its first and second partial derivatives, are introduced the computer carries out numerically four operations as follows:

(1) Simultaneously solves the set of characteristic differential equations to determine the paths of water flow
(2) Evaluates the permeability integral along the path obtained in Step 1 to determine the permeability along the path
(3) Evaluates the travel time integral along the flow path using the permeability found in Step 2 and the potential
(4) Calculates the flux distribution in the flow system.

The first three operations are carried out in steps, a single path at a time, until all are completed; the flux indices are then evaluated for each of the steady path lines generated previously.

Careful evaluation of the numerical errors involved in the methods used in these steps has shown accuracies which far exceeded original expectation. The error analysis also showed the accuracy to be independent of the pathlength.

EXTENSION OF SOLUTION CAPABILITIES BY FINITE DIFFERENCES METHOD TO A LARGE CLASS OF STEADY-STATE FLOW PROBLEMS— A. E. Reisenauer

The Hanford-developed computer program STEADY DARICAN FLOW IN SOILS has been enlarged and extended to include capabilities for solving a large class of flow problems. These new features include a variable mesh size for the finite differences expression, a flux input independently control-Zed at every node, an enlarged number of node points, and the ability, in partially saturated soil, to vary the capillary conductivity completely by inputing soil type curves and varying the base permeability of the soil at any node.

The equations describing macroscopically a rather large class of steady-state flow problems in porous media were presented by Nelson,[9] along with a means of solution by computer techniques. The computer program was developed and its use and capabilities described by Reisenauer, et al. in 1964.[10-12]

Although the basic program is adaptable to many boundary value problems, certain closely related problems could not be modeled. The change to the Univac 1107 computer with its larger memory capacity and the development of advanced programming techniques permitted the expansion of the STEADY DARCIAN FLOW IN SOILS program. The new version has larger rapacity and greater flexibility to aid in encompassing a larger class of flow problems.

The basic partial differential equation (presented here in three-dimensions) developed from Darcy's Law and the proper equations of state and conservation of mass is as follows:

$$K\left[\frac{\partial^2\phi}{\partial x^2}+\frac{\partial^2\phi}{\partial y^2}+\frac{\partial^2\phi}{\partial z^2}\right]+\frac{\partial K}{\partial x}\frac{\partial\phi}{\partial x}+\frac{\partial K}{\partial y}\frac{\partial\phi}{\partial y}+\frac{\partial K}{\partial z}\frac{\partial\phi}{\partial z}+Q=0 \qquad (1)$$

where ϕ is the potential, K is the permeability, and Q is a flux quantity The x, y, and z are Cartesian coordinates. The expansion of the equation into its finite differences representation was made with $\Delta x \neq \Delta y \neq \Delta z$. This resulted in the following equation which allows for a grid with a variable mesh in all directions.

$$\phi_{i,j,k}=\frac{1}{\left[\frac{1}{\left(\frac{\Delta x_1}{\Delta z_2}\right)\left(\frac{\Delta x_1}{\Delta z_2}\right)}+\frac{1}{\left(\frac{\Delta y_1}{\Delta z_2}\right)\left(\frac{\Delta y_2}{\Delta z_2}\right)}+\frac{1}{\frac{\Delta z_1}{\Delta z_2}}\right]}\left\{\frac{\frac{\phi_{i+1,j,k}}{\frac{\Delta x_2}{\Delta z_2}}+\frac{\phi_{i-1,j,k}}{\frac{\Delta x_1}{\Delta z_2}}}{\frac{\Delta x_1}{\Delta z_2}+\frac{\Delta x_2}{\Delta z_2}}\right.$$

$$+\left.\frac{\dfrac{\phi_{i,j+1,k}}{\Delta y_2}+\dfrac{\phi_{i,j-1,k}}{\Delta y_1}}{\dfrac{\Delta z_2}{\Delta y_1}+\dfrac{\Delta z_2}{\Delta y_2}}+\frac{\phi_{i,j,k+1}+\dfrac{\phi_{i,j,k-1}}{\dfrac{\Delta z_1}{\Delta z_2}}}{\dfrac{\Delta z_1}{\Delta z_2}+1}\right)$$

$$+\frac{1}{2K_{i,j,k}}\left[\frac{\left(K_{i+1,j,k}-K_{i-1,j,k}\right)\left(\phi_{i+1,j,k}-\phi_{i-1,j,k}\right)}{\dfrac{\Delta x_1}{\Delta z_2}+\dfrac{\Delta x_2}{\Delta z_2}}\right]$$

$$+\frac{1}{2K_{i,j,k}}\left[\frac{\left(K_{i,j+1,k}-K_{i,j-1,k}\right)\left(\phi_{i,j+1,k}-\phi_{i,j-1,k}\right)}{\dfrac{\Delta y_1}{\Delta z_2}+\dfrac{\Delta y_2}{\Delta z_2}}\right]$$

$$+\left.\frac{1}{2K_{i,j,k}}\left[\frac{\left(K_{i,j,k+1}-K_{i,j,k-1}\right)\left(\phi_{i,j,k+1}-\phi_{i,j,k-1}\right)}{\left(\dfrac{\Delta z_1}{\Delta z_2}+1\right)^2}\right]\right\}$$

$$+\frac{Q_{i,j,k}}{2\Delta z_2{}^2K_{i,j,k}\left[\dfrac{1}{\left(\dfrac{\Delta x_1}{\Delta z_2}\right)\left(\dfrac{\Delta x_2}{\Delta z_2}\right)}+\dfrac{1}{\left(\dfrac{\Delta y_1}{\Delta z_2}\right)\left(\dfrac{\Delta y_2}{\Delta z_2}\right)}+\dfrac{1}{\dfrac{\Delta z_1}{\Delta z_2}}\right]}$$

where i, j, and k are the index integers of the grid points in the x, y, and z directions, respectively; and Δx_1, Δx_2, Δy_1, Δy_2, Δz_1 and Δz_2 are the distances to surrounding nodes, with the subscript 1 denoting the positive direction along the axis. Equivalent expressions for the one- and two-dimensional and axisymmetrical cases are used in the program when required. These equations may be obtained by appropriately modifying Equations (1) and (2).

The most significant use of the feature is that larger flow systems may be modeled with a close-mesh grid

in regions of greatest changes in potential and the mesh may be gradually expanded for movement into regions of small changes. The extended grid will permit flow models to reach distant fixed (known) boundaries rather than setting arbitrary, possibly erroneous boundaries close in.

Another feature changed in the equations is the addition of Q (flux) at any node where the potential changes during iteration. A list of Q values and the associated indices is stored for every node. Q may be used to simulate any flow which is constant yet does not maintain a constant potential.

The ability to model heterogeneous soil in partially saturated flow is greatly enlarged by allowing use of 15 soil-type curves of capillary pressure, capillary conductivity and a base permeability. Since the soil curves are dimensionless, a neri base permeability for each curve which may be varied from node to node adds great flexibility. Previous programs permitted blocking of soil types which resulted in sharp unrealistic changes in soil characteristics. This change will allow more natural blending across soil-type boundaries.

A THEORETICAL BASIS FOR USING ONLY THE PRESENT ENERGY DISSIPATION PATTERN TO PREDICT NEW GROUND WATER POTENTIAL DISTRIBUTION IN HETEROGENEOUS POROUS MEDIA—

R. W. Nelson

An equation is presented that allows including the effects of nonhomogeneous soils on new potential distributions without directly solving for the soil permeability distribution. In situations where the travel times or fluxes are not required to answer the problem at hand, then considerable economy in computational effort is brought about through use of the equations derived here.

In preceding papers[8,13-15] theoretical considerations were given to the more basic theory for steady flow in heterogeneous media. In-place measurement was shown to be possible. The search for effective solution methods for the permeability culminated in derivation of the "Permeability Integral,"[16] which was needed to determine travel times and which reappears in solving for the new potential distribution. Further study has shown that for steady flow systems, the permeability is required to obtain travel times. The new potential distribution can be determined using the equations derived here.

Consider an existing steady flow system in soil of permeability $k(x,y,z)$ and with an associated potential distribution $\phi(x,y,z)$. The partial differential equation describing the flow system[13-17] is (using the del operator, ∇):

$$k\nabla^2\phi + \nabla k \cdot \nabla\phi = 0 \qquad (1)$$

or

$$\nabla^2\phi + \nabla \ln k \cdot \nabla\phi = 0 \qquad (2)$$

which can be shown to reduce to the set of ordinary differential equations when k is considered as dependent:

$$\frac{\frac{dx}{ds}}{\frac{\partial\phi}{\partial x}} = \frac{\frac{dy}{ds}}{\frac{\partial\phi}{\partial y}} = \frac{\frac{dz}{ds}}{\frac{\partial\phi}{\partial z}} = -\frac{\frac{dk}{ds}}{k\nabla^2\phi} \quad . \quad (3)$$

Starting with the identity:

$$\nabla\phi \cdot \frac{d\underline{r}}{ds} = \frac{\partial\phi}{\partial x}\frac{dx}{ds} + \frac{\partial\phi}{\partial y}\frac{dy}{ds} + \frac{\partial\phi}{\partial z}\frac{dz}{ds} \quad . \quad . \quad . \quad (4)$$

and substituting from Equation (3) gives:

$$\nabla\phi \cdot \frac{d\underline{r}}{ds} = \left(\frac{\partial\phi}{\partial x}\right)^2 \frac{dy}{ds} + \left(\frac{\partial\phi}{\partial y}\right)^2 \frac{dy}{ds} + \left(\frac{\partial\phi}{\partial z}\right)^2 \frac{dy}{ds} \quad . \quad . \quad . \quad (5)$$

or,

$$\nabla\phi \cdot \frac{d\underline{r}}{ds} = |\nabla\phi|^2 \frac{\frac{dy}{ds}}{\frac{\partial\phi}{\partial y}} = -\frac{|\nabla\phi|^2}{\nabla^2\phi}\left(\frac{1}{k}\right)\frac{dk}{ds} \quad . \quad . \quad . \quad (6)$$

where the rightmost expression is a substitution again from Equation (3), using the one relationship not used previously. Rearranging Equation (6) gives:

$$\frac{1}{k}\frac{dk}{ds} = -\frac{\nabla^2\phi}{|\nabla\phi|^2}\nabla\phi \cdot \frac{d\underline{r}}{ds} \quad (7)$$

But,

$$\frac{1}{k}\frac{dk}{ds} = \frac{d(\ln k)}{ds} = \nabla \ln k \cdot \frac{d\underline{r}}{ds} \quad ; \quad (8)$$

therefore,

$$\nabla \ln k \cdot \frac{d\underline{r}}{ds} = -\frac{\nabla^2\phi}{|\nabla\phi|^2}\nabla\phi \cdot \frac{d\underline{r}}{ds} \quad . \quad (9)$$

But, the respective dot products of two vectors with the same vector $\frac{d\underline{r}}{ds}$ are equal only if

$$\nabla \ln k = -\frac{\nabla^2\phi}{|\nabla\phi|^2}\nabla\phi \quad (10)$$

which is the general relationship desired. If a new flow system is to be solved in the same soil mass then one would seek the new potential distribution, say $\Omega(x,y,z)$, which again must satisfy the form of Equation (2) in Ω:

$$\nabla^2\Omega + \nabla \ln k \cdot \nabla\Omega = 0 \quad . \quad (11)$$

Then, substituting Equation (11) for the permeability term gives

$$\nabla^2\Omega - \frac{\nabla^2\phi}{|\nabla\phi|^2}\nabla\phi \cdot \nabla\Omega = 0. \quad (12)$$

which shows that if the potential ϕ, for the present flow system is known then solution of Equation (12) for Ω, subject to the boundary conditions, provides the potential distribution directly in the new flow system. Hence, the permeability distribution <u>per se</u> need never be known to determine the potential in the new flow system.

EQUATIONS DESCRIBING THE SIMULTANEOUS FLOW OF TWO IMMISCIBLE FLUID PHASES IN HETEROGENEOUS POROUS MEDIA- R. W. Nelson

Theoretical work leading to the description of fluid flow in a heterogeneous porous medium has developed slowly and somewhat sporadically even though the areas of engineering applications predominantly involve flow in nonhomogeneous media. In providing a theoretically consistent basis for analysis, the special characteristics of macroscopically heterogeneoMs materials are discussed to provide accurate definitions. The definitions establish the functional dependence and make mathematical representation possible. The special implications of heterogeneity on Darcian-type dynamic relationships for each of the fluid phases are considered. The end result is a set of rather general Eulerian equations describing two-phase flow in a macroscopically heterogeneous medium. These equations and their reduced forms include description of some 40 different flow systems. Such a variety of flow conditions is categorized through the use of a special tabular scheme which makes it possible to write the appropriate equations very efficiently.

Analysis

A macroscopic description of fluid flow in nonhomogeneous media is needed. Precise statements of the properties of the fluids and porous media, along with a characterization of flow, provide the equations of state and dynamics. These equations, when combined with the equations of conservation of mass, provide a complete hydrodynamic description that yields the required fundamental expressions. Description of each fluid phase will be required, so twice the number of relationships will be involved for two phases.

Fluid Properties

The fluids are assumed to be effectively continuous and homogeneous in structure. This implies that the properties of the smallest subdivisions are the same as those of large samples. Strictly speaking this is not the case; but, in this application, the dimensions concerned are large compared to molecular structure, and the assumed continuum is both acceptable and useful. Accordingly, gross measurements of physical properties of density, visosity and surface tension are appropriate. The fluids are considered to be compressible and the flow system isothermal; therefore, the mass density, ρ, is at most a function of the pressure, p; that is:

$$\rho = f(p). \qquad (1)$$

Starting the formulation in a generalized form makes it possible to consider barotropic compressible fluids; yet incompressible fluids are handled automatically for the reduced case of constant density

Dynamic Equations

A statement of the physical principles governing motion is needed to develop the required basic equations. The usual working hypothesis that Darcy's Law is valid for each of the flowing phases will be the starting point here.[18]* Therefore, the dynamic relationship assuming isothermal flow

---

* *Although widely accepted for macroscopic description of flow in heterogeneous media, and certainly the author believes the Darcy expression to be*

for the wetting phase is:

$$\underline{q}_1 = - \frac{k_1 \rho_1}{\mu_1} \left(- \underline{g} + \frac{1}{\rho_1} \text{ grad } p_1 \right) . \quad (2)$$

The difference in pressure across the interface between the two phases is the capillary pressure, p_c, defined as

$$p_c = p_2 - p_1 . \quad (4)$$

The capillary pressure represents the pressure discontinuity across the interface separating the two immiscible fluids, and it thereby interrelates Equations (2) and (3). The permeability and fluid content characteristics of the porous media are related to the capillary pressure. Accordingly, the permeability, k, and fluid content on a pore-volume basis, s, are functions of the capillary pressure, p_c.

$$k = K(p_c), \; p_c \geq 0 \quad (5)$$

and

$$s = S(p_c), \; p_c \geq 0. \quad (6)$$

The functional relationships are uniquely dependent upon the properties of the material phases involved and the geometrical properties of the phase interfaces. The interfaces are in turn dependent on the pore geometry of the porous medium and the previous history of fluid content. The latter, hysteresis effect, will not be considered here since theoretical analysis is only now starting to emerge for homogeneous media.

The similarity of Equations (2) and (3) makes it convenient to drop the subscripts of the latfer compressible flow equation for the discussion of dynamic characteristics to follow. Since the incompressible flow result [Equation (2)] is a special case, any derived results can be written directly at the end of the analysis. Therefore,

$$\underline{q}_n = - \frac{k \rho_n}{\mu_n} \left(- \underline{g} + \frac{1}{\rho_n} \text{ grad } p_n \right) . \quad (7)$$

The special features in Equation (7) are in using it as the form for the dynamic equations for describing flow in heterogeneous porous media. Careful consideration of these features enables one to arrive at precise definitions which form the basis of the mathematical work to follow.

"Heterogeneous" as used here implies differing in kind, having unlike quantities, or possessing different characteristics. Accordingly, a heterogeneous porous medium has unlike quantities or differing characteristics at different locations. More precisely, if a porous medium is heterogeneous with respect to some property then that property is functionally dependent on the

---

valid, nevertheless it must be introduced here as a postulate, since no generalized statistical treatment for heterogeneous porous media is now available. In fact, only quite recently has the postulate basis for Carcian description of flow in homogeneous porous media been supported on theoretical grounds through statistical treatment starting from the Ergodic Hypothesis.[18,19] *Since the Ergodic Hypothesis in present form does not enable statistical consideration for heterogeneous porous media, we must be content at present to accept this postulate largely from intuitive and physical arguments. Specifically, the author would suggest careful consideration of the extrapolated functional properties in Hubbert's 1956 paper.*[20]

spatial location. Specifically considering the permeability, k, as heterogeneous then:

$$k \equiv \mu k(x,y,z), \tag{8}$$

or the permeability is a scalar function, μ, of the location. We note in passing that spatial variation of several other properties, of which porosity, dispersivity, and medium compressibility are but a few, is implied by the broad term "heterogeneous." In this work the phrase will be used, although not always stated, to imply only heterogeneity with respect to the permeability.

The mathematical result of defining heterogeneity, Equation (8), can be combined with the multiple phase effects of Equation (5) to provide a rigorous description of the permeability in Equation (7). That is:

$$k = F[p_c(x,y,z,t),x,y,z]. \tag{9}$$

The F denotes a function of the space coordinates x, y, and z, and the capillary pressure, p_c, which through Equation (4) is again dependent upon the coordinates x, y, and z, and time, t. The needed definitions are incorporated in the dependence Equation (9).

Equations of Continuity

The equations of continuity (conservation of mass) are the remaining requirement for a complete Eulerian formulation for this class of problems. Again consistent with the earlier practice, only the continuity equation for the more general compressible phase is discussed. The reduced forms for incompressible flow will be presented later with appropriate subscripts from the more general cases that are derived here.

For enclosing surface Σ, the integral of the instantaneous mass inflow and outflow must equal the change in saturation density. Therefore,

$$\iint_{\Sigma} \rho \underline{q} \cdot \underline{n}\, d\Sigma = -\frac{\partial}{\partial t}\iiint_{V} \rho P s\, dV \tag{10}$$

where I is the surface encompassing the volume V, and $\underline{n}$ is the unit vector normal to Σ. To change the surface integral to a volume integral, on the left side of Equation (10) (the macroscopic description assures conditions sufficient to allow interchanging the order of differentiation and integration) Gauss' theorem may be used; hence,

$$\iiint_{V} \operatorname{div} \rho \underline{q}\, dV = -\iiint_{V} P\frac{\partial(\rho s)}{\partial t} dV \tag{11}$$

or

$$\operatorname{div} \rho \underline{q} = -P\frac{\partial(\rho s)}{\partial t} \tag{12}$$

and after substituting Equation (7) into (12) the result is

$$\operatorname{div}\left(\frac{\rho^2 \kappa}{\mu} \operatorname{grad} \phi\right) = P\frac{\partial(ps)}{at}. \tag{13}$$

The functional dependence arising from the original definitions is fundamental to expanding Equation (13) properly. Define the potential, ϕ, of the form

$$\phi = \int \frac{dp}{\rho} + gz + C_1 \tag{14}$$

then expansion of Equation (13), consistent with Equations (1), (9), and (14), gives for use with Figure 9

$$\frac{\rho_n^{\angle} F_n}{"n} \operatorname{div} \operatorname{grad} \phi_n + \frac{2\rho_n F_n}{\mu_n}\frac{df}{dp_n} \operatorname{grad} p_n \cdot \operatorname{grad} \phi_n$$

$$+ \frac{\rho_n^{\angle}}{\mu_n}\left[\frac{\partial F_n}{\partial p_c} \operatorname{grad} p_c + \operatorname{grad} F_n\right] \cdot \operatorname{grad} \phi_n = P\left[S_n \frac{\partial f_n}{\partial t} + \rho_n \partial t\right. \tag{15}$$

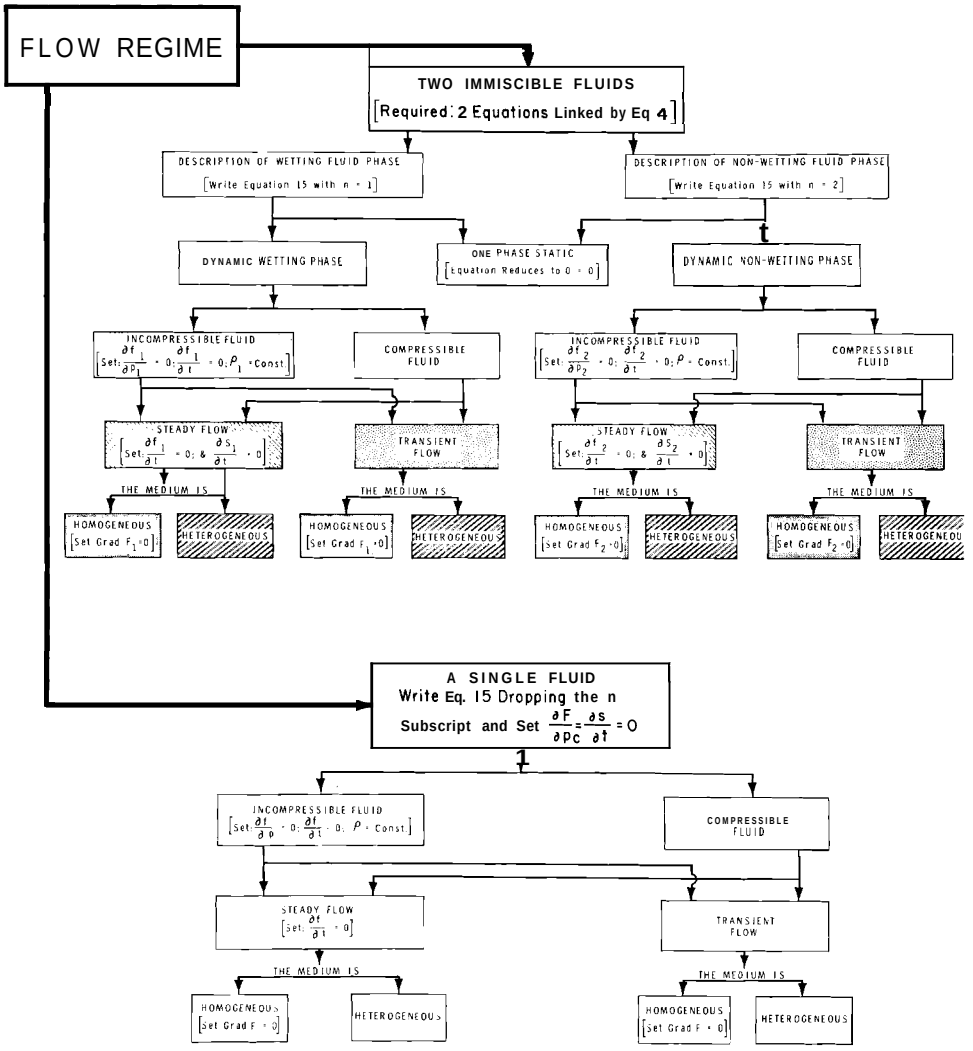

FIGURE 9. Outline of Flow Systems Considered and a Guide to Writing the Descriptive Equation.

where:

- ρ is the fluid mass density
- F is the functional describing intrinsic capillary permeability or reduced forms [see Equation (9)]
- f is the functional describing the pressure dependence of ρ
- K is the functional describing the permeability, k, dependence on capillary pressure, p_c [See Equation (5)]
- μ is the dynamic viscosity
- ϕ is the fluid potential of the phase denoted by the subscript used
- p is the fluid pressure of the phase denoted by the subscript used
- n used as a subscript denotes the fluid phase to which the variable that is subscripted applies, that is:
  - n=l denotes the fluid phase which wets the porous medium, and
  - n=2 denotes the fluid phase which does not wet the porous medium

  $p_c = p_2 - p_1$ is the capillary pressure
- P is the porosity, i.e., the volume of pores per unit volume

s is the fluid saturation on a pore volume basis

S is the functional describing the saturation dependence on capillary pressure, p_c, [See Equation (6)]

t is time.

Equation (15) is general and contains as special cases some 40 different types of flow systems. Such a large number of equations and the associated description is prohibitive to present here. However, they are obtained from Equation (15), through use of Figure 9. The special cases are given by performing the suggested operations indicated in the figure. The cross-hatching and shading used in the lower right part of the figure indicate the special compatibilities required between the wetting and nonwetting phases. If condition of shading type is used in the wetting phase, then the same shaded condition is required for the nonwetting phase. That is, if the wetting phase is transient then the nonwetting phase could not be steady but of necessity would be transient also. Similarly, the medium is either heterogeneous or homogeneous; hence it must be consistent for both phases (the same shading is used in Figure 9). This material is presented and discussed in more detail in Reference (21).

MINERAL CHEMISTRY

MONTMORILLONITE EXCHANGE EQUILIBRIA WITH STRONTIUM-SODIUM-CESIUM-J. R. Eliason

The ion exchange isotherms and the free energy changes of -2278, -331, and -4019 cal/mole for the cesium-sodium, strontium-sodium, and cesium-strontium systems respectively were determined for the Bayard, New Mexico montmorillonite. The same measurement gave -2035 cal/mole for the cesium-sodium system on the Chambers, Arizona montmorillonite. A surprising increase in selectivity for cesium and strontium at high loadings was observed in the cesium-sodium and strontium-sodium systems. The selectivity increases were presumed to be related to changes in the c-axis spacings.

Determination of the influence of clay minerals on the behavior of radioactive wastes in soil systems requires a better understanding of the cation exchange characteristics of the clay minerals. This study was to determine several exchange isotherms and associated free-energy changes for a montmorillonite of hydrothermal origin and to make a comparison of the exchange characteristics of two montmorillonites of different origin.

Studies of the ion exchange isotherms and the determination of the related free-energy changes on clay minerals are limited. The Chambers, Arizona, montmorillonite (reference Clay Mineral No. 23 of the American Petroleum Institute) has been studied, and the ion exchange isotherms and related free-energy changes were determined by Lewis and Thomas[22] and earlier by Frysinger and Thomas.[23] The Chambers, Arizona, montmorillonite is believed to[24] have originated

from volcanic tuff of a basic extrusive which was deposited as ash in a lake basin and altered in place. The montmorillonite chosen for this study was Reference Clay Mineral No. 30a of the American Petroleum Institute, from Bayard, New Mexico. The Bayard, New Mexico, montmorillonite is believed [24] to be of hydrothermal origin from solutions penetrating a rhyolitic and andesitic tuff.

The exchange isotherm and the free-energy change for the sodium-cesium system on the Chambers, Arizona, montmorillonite were redetermined for comparison with previous work. [22]

The exchange isotherms for the strontium-sodium, cesium-sodium, and cesium-strontium systems plotted in Figures 10, 11, and 12 respectively show that both montmorillonites have a preference for

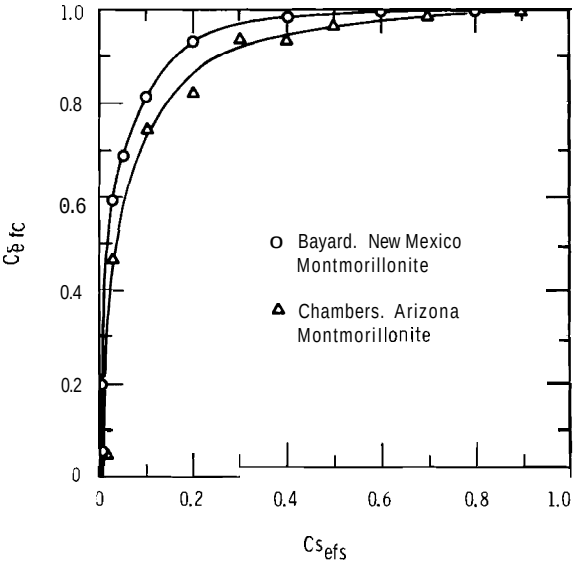

FIGURE 11. The 25 °C Isotherm for the Reaction $Cs_s + Na_c \rightleftarrows Na_s + Cs_c$ *on the Bayard, New Mexico, and Chambers, Arizona, Montmorillonites. Total Equilibrium Solution Normality was Constant at 0.05. (Subscript efc = Equivalent Fraction on the Clay; Subscript efs = Equivalent Fraction in the Solution.)*

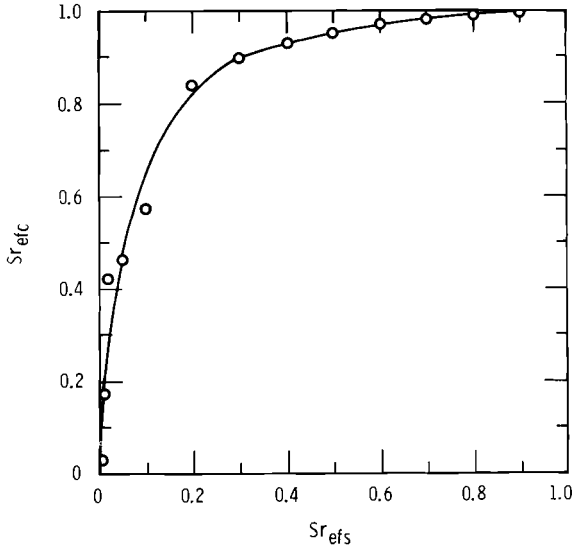

FIGURE 10. The 25 °C Isotherm for the Reaction $Sr_s + 2Na_c \rightleftarrows 2Na_s^+ + Sr_{2c}$ *on the Bayard, New Mexico Montmorillonite. Total Equilibrium Solution Normality was Constant at 0.05. (Subscript efc = Equivalent Fraction on the Clay; Subscript efs = Equivalent Fraction in the Solution.)*

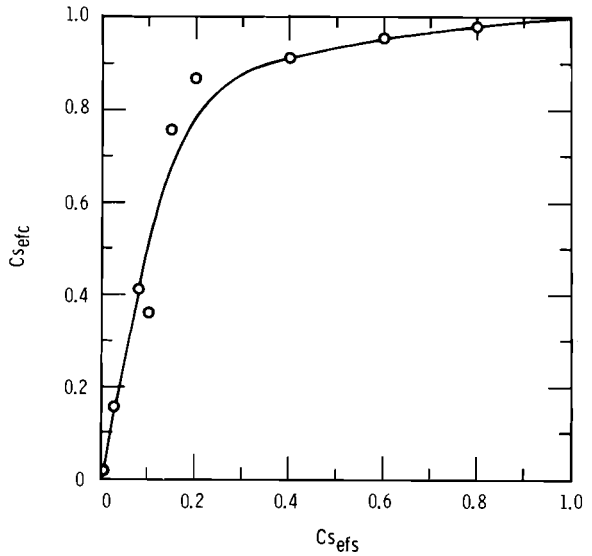

FIGURE 12. The 25 °C Isotherm for the Reaction $2Cs_s + Sr_{2c} \rightleftarrows Sr_s + 2Cs_c$ *on the Bayard, New Mexico, Montmorillonite. Total Equilibrium Solution Normality was Constant at 0.05. (Subscript efc = Equivalent Fraction on the Clay; Subscript efs = Equivalent Fraction in the Solution.)*

cesium over sodium and that a preference for strontium over sodium and for cesium over strontium is shown by the Bayard, New Mexico, montmorillonite.

The values of the Gibbs free-energy changes for the reactions studied on the montmorillonites are presented in Table 1.

The accuracy of the equilibrium results can be checked by balancing the Gibbs free-energy changes determined for three related reactions. From the equation

$$2\ \Delta F^\circ\ (Na_c \rightarrow Cs_c) - \Delta F^\circ\ (2Na_c \rightarrow Sr_{2c}) = \Delta F^\circ\ (Sr_{2c} \rightarrow 2Cs_c)$$

the free-energy change in the strontium-cesium system was predicted to be -4225 cal/mole, and the actual measured value was -4019 cal/mole. The free-energy of -2035 cal/mole determined for the Chambers, Arizona, montmorillonite also is in good agreement with the free-energy of -2152 cal/mole reported by Lewis and Thomas.

The ln Kc' values of the equilibrium reactions of the Bayard, New Mexico, montmorillonite are plotted in Figure 13. The ln Kc's values and the ln Kc' curve presented by Lewis and Thomas for the sodium-cesium system are shown in Figure 14. The sodium-cesium system of the Bayard, New Mexico, montmorillonite shows a surprising increase in the selectivity for cesium above 90% cesium loading. The selectivity for strontium increased over the entire range of strontium loading in the sodium-strontium system on the Bayard, New Mexico, montmorillonite. Over the range from 0 to 40% strontium loading the montmorillonite was sodium selective. Above 40% it became strontium selective, with a marked increase in strontium selectivity above 90% strontium loading. In the strontium-cesium system of the Bayard, New Mexico, montmorillonite, the initial selectivity for cesium was greater than in the sodium-cesium system, and a decrease in cesium selectivity was noted above 40% cesium loading.

In the sodium-cesium system of the Chambers, Arizona, montmorillonite a gradual decrease in selectivity for cesium, followed by a definite increase in cesium selectivity above 90% cesium loading, was observed. The increase in cesium selectivity above 90% cesium loading corresponds to the cesium selectivity change observed in the Bayard, New Mexico sample, but the increase was not

Table I. Free-Energies of Exchange at 25 °C

Reaction	ΔF°, cal/mole
Bayard, New Mexico, Montmorillonite	
$Cs_s + Na_c \rightleftarrows Na_s + Cs_c$	- 2278
$Sr_s + 2Na_c \rightleftarrows 2Na_s + Sr_{2c}$	- 331
$2Cs_s + Sr_{2c} \rightleftarrows Sr_s + 2Cs_c$	- 4019
Chambers, Arizona, Montmorillonite	
$Cs_s + Na_c \rightleftarrows Na_s + Cs_c$	- 2035

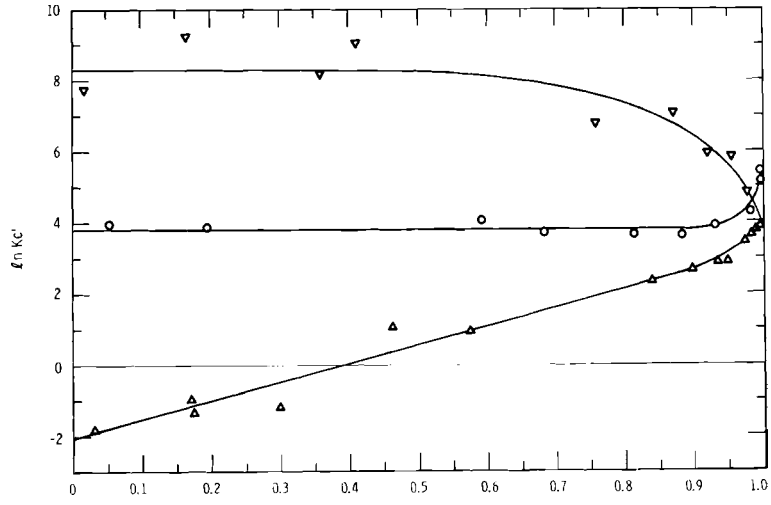

FIGURE 13. The Stoichiometric Equilibrium Coefficients on the Bayard, New Mexico Montmorillonite at 25 °C (Subscript efc = Equivalent Fraction on the Clay.)

A–$Srs + 2Na_c \rightleftarrows 2Na_s + Sr_{2c}$ ln Kc' Versus Sr_{efc}

o–$Cs^+_s + Na_c \rightleftarrows Na_s + Cs_c$ ln Kc' Versus Cs_{efc}

▽–$2Cs^+ + Sr_{2c} \rightleftarrows Sr_s + 2Cs_c$ ln Kc' Versus Cs_{efc}

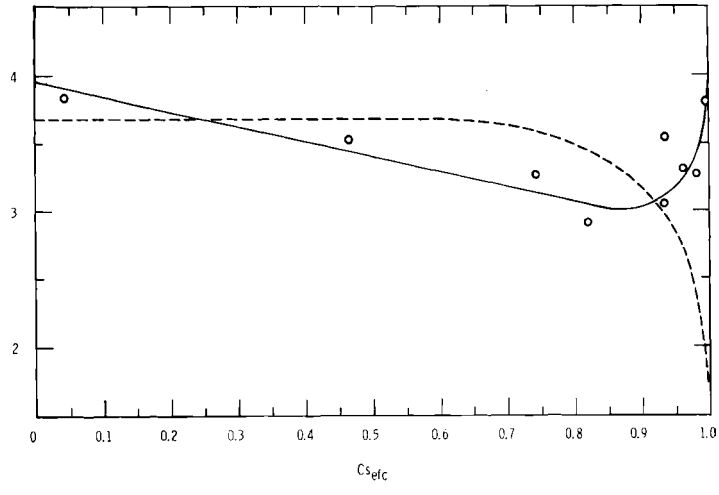

FIGURE 14. The Stoichiometric Equilibrium Coefficients on the Chambers, Arizona, Montmorillonite at 25 °C (Subscript efc = Equivalent Fraction on the Clay.)

o —— $Cs_s + Na_c \rightleftarrows Na_s + Cs_c$

– – $Cs_s + Na_c \rightleftarrows Na + Cs_c$ Lewis and Thomas (1963).

observed by Lewis and Thomas. The cesium selectivity above 90% cesium loading showed a marked decrease in the equilibrium results given by them. The difference in the cesium selectivity change reported by Lewis and Thomas, as compared to this study, may be due to differences in the clay samples, sample preparation methods, equilibrium column techniques, or other unknown differences between the two studies. Lewis and Thomas' treatment of the Chambers, Arizona, montmorillonite with sodium hexametaphosphate during sample preparation is a good example of the differences between the two studies.

The effect of increased selectivity with increased loading of cesium and strontium on the sodium clay may be due to the difference in the c-axis spacing noted in X-ray work with the Bayard, New Mexico, montmorillonite. Samples of that montmorillonite based with sodium, strontium, and cesium were air-dried at 25 °C. X-ray patterns indicated one molecular interlayer of water in each case. The sodium, strontium, and cesium X-ray mounts were equilibrated with a saturated glycol atmosphere at 70 °C and a normal spacing of about 17.7 Å was found. Samples of the sodium, strontium, and cesium-based clay were saturated with 0.05N chloride solutions of sodium, strontium, and cesium respectively and X-ray patterns indicated an interlayer spacing change from the air-dried samples. The strontium-based clay had approximately a 20 Å c-axis spacing and the sodium c-axis spacing was greater than 40 Å. The cesium-based clay maintained its one molecular interlayer of water or about 12.5 Å. Clay minerals with smaller c-axis spacings have been shown to be more selective for cesium by Tamura.[25] The increase in the selectivity for cesium over sodium at 90% cesium loading presumably corresponds to a decrease in the c-axis spacing from greater than 40 Å to 12.5 Å. A cesium selectivity increase does not occur until nearly 90% of the sodium has been exchanged, allowing a relatively rapid approach to the 12.5 A c-axis spacing for cesium. The increase in the strontium selectivity over sodium presumably corresponds to a c-axis spacing change from greater to 40 Å to 20 Å. The strontium exchange for sodium allows a progressive c-axis spacing change from greater than 40 Å to the 20 Å strontium spacing. The c-axis spacings of strontium and cesium are close enough (about 20 Å and 12.5 Å, respectively) to result in the "usual" type of isotherm in a cesium-strontium system where cesium selectivity decreases with increasing fraction of cesium on the clay.

SELF-DIFFUSION OF SODIUM IN VERMICULITE — B.F. Hajek and J. R. Eliason

Particle self-diffusion coefficients of sodium were determined in a fraction of nearly pure vermiculite utilizing a thin bed technique. The size fractions were obtained by sieving and sedimentation. The self-diffusion coefficient of sodium at exchange half-time was 0.56 x 10^{-7} cm^2/sec.

The fact that the rate-determining step in ion exchange is the interdiffusion counter ions has been established.[26] A comprehensive review of this problem and its significance to the mathematical treatment of ion exchange column performance is given by Helfferich.[27] Most research which shows the role of particle diffusion in ion exchange has been done on exchange resins and in natural and synthetic zeolites. Less effort has been given to the study of ion exchange kinetics in soils and clay minerals, although the need for such information has often been expressed.[28, 29]

This paper gives experimental results of sodium isotopic reaction rate measurements on a fraction of an essentially pure vermiculite. This mineral was selected because of its contribution to the exchange capacity of local and many other soils and because fractions larger than clay-size can be obtained by grinding. Calculated sodium self-diffusion coefficients are also reported.

A vermiculite sample which is essentially the pure magnesium end member of the mineral was studied.[30] The sample was wet-ground in a food blender, washed twice with sodium acetate solution at pH 5, freed of iron oxides[31] and dispersed in Na_2CO_3 solution. Fractionation was achieved by sieving and sedimentation.

Diffusion rates were determined by a shallow hed technique[27] with an apparatus described by Ames[32] and shown in Figure 15. The rates were determined by recording the removal of ^{22}Na from a thin bed column positioned in front of a NaI(Tl) scintillation crystal. A column technique was used to determine the cation exchange capacity which was similar to that described by Lewis and Thomas.[23]

The rate of isotopic exchange of sodium for a 20 to 53 μ fraction of vermiculite is shown in Figure 16 Time to completion is not shown although exchange was continued until the reaction was at least 99% complete. Reaction time to 99% completion was 1.5 min. The exchange capacity of this fraction was determined to be 236 meq/100 g.

The diffusions coefficients, C/C_i shown in Table I were determined from a solution of the diffusion equation given by Jost.[33]

$$\frac{\partial C}{\partial t} = \frac{1}{r} \frac{\partial}{\partial r}\left(r\ D\ \frac{\partial C}{\partial r}\right)$$

in which C = concentration, r = radius, t = time, and D = diffussion Coefficient. This equation describes radial diffusion in a cyclinder

TABLE II. Self-diffusion Coefficients of Sodium in the Interlayer Space of Vermiculite

Average Particle Size, μ	C/C_i	Diffusion Coefficient 10^{-7} cm^2/sec
34	0.6	0.57
34	0.5	0.56
34	0.4	0.49

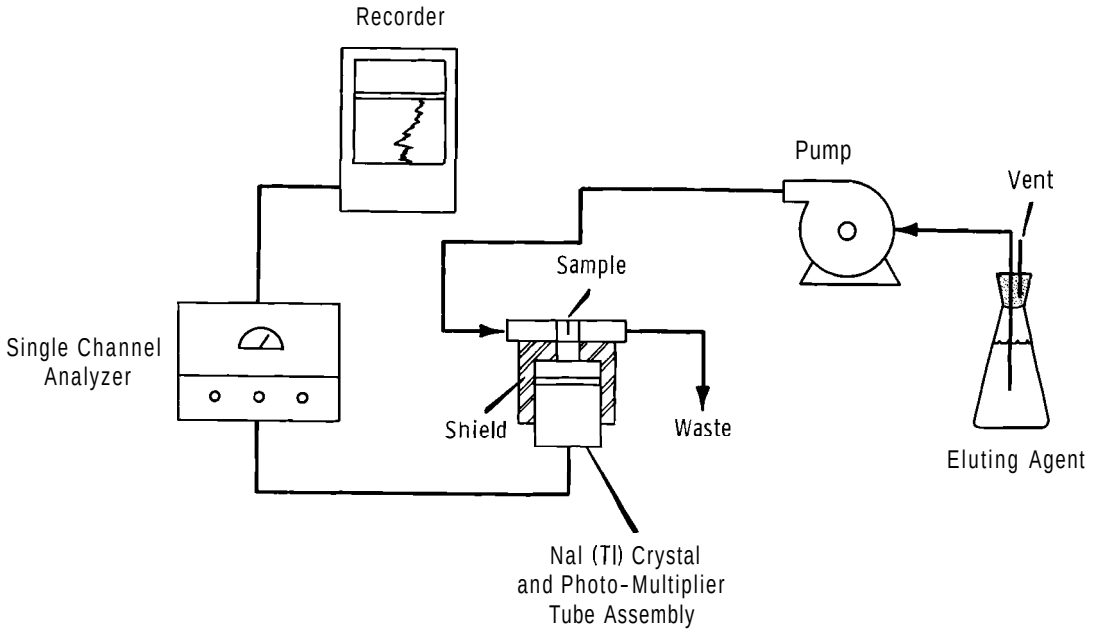

FIGURE 15. Experimental Apparatus Used to Obtain Kinetic Data

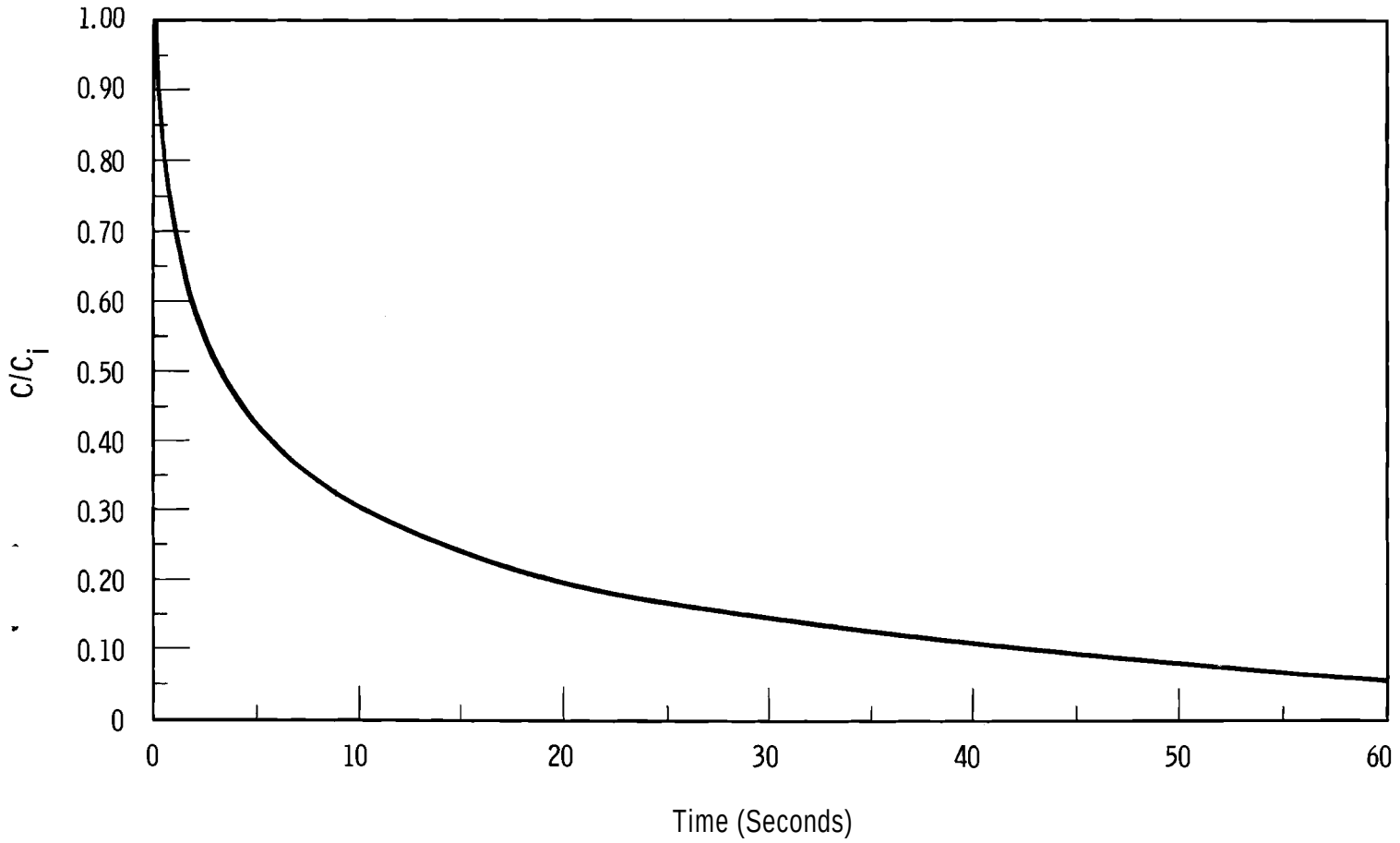

FIGURE 16. Rate of Isotopic Exchange of Sodium in Vermiculite

of infinite length or in a finite cylinder with sealed end faces. The solution of this equation given by Jost is

$$\frac{C - C_f}{C_i - C_f} = \sum_{1}^{\infty} \frac{4}{\xi_\nu} \exp - \frac{\xi_\nu^2 Dt}{r^2}$$

for the following initial and boundary conditions:

$C = C_i = 0$ for $0 < r < r$ and $t = 0$,

$C = C_f = 0$ for $r = r_o$ and $t > 0$.

In the solution, C_i = initial concentration in the cylinder, r_o = cylinder radium, C_f = final concentration which was zero in this study, and ξ_ν = roots of the equation $Jo(x) = 0$ where $Jo(x)$ is the Bessel function of zero order.

The first four terms of the summation and experimental values from Figure 16 were used in a graphical solution for D; however, little error would have been introduced if only the first term is used and the solution for D is made at $C/C_i = 0.5$. In this case, considering the half-time of exchange ($t_{1/2}$) D is readily estimated from

$$D = \frac{0.0557r^2}{t_{1/2}}$$

or, utilizing the first four terms,

$$D = \frac{0.0635r^2}{t_{1/2}}$$

By the use of an average sodium self-diffusion coefficient, the half-time of sodium isotopic exchange in this system can be related to particle radius by the expression

$$t_{1/2} = r^2 \times 10^6 .$$

Considering that the diffusion coefficient is the same for 2μ particles (clay size upper limit), the reaction time for 50% completion would be 10^{-2} sec. The reaction rates of clay fractions (0.2 to 2μ) from the A horizon of an Ephrata, Washington, soil (mostly montmorillonite and vermiculite) and from a New Mexico montmorillonite were too rapid to be measured accurately with this aoparatus; that is, the exchange was complete in less than 3 sec.

Despite a distribution of particle sizes within the fraction, the calculated particle self-diffusion coefficient of sodium is within the limits of expected diffusion coefficients.[31] Larger size fractions also were used, and variation between particle sizes was not considered great. The data further substantiate that ion exchange reactions in soil and clays can reach completion in a very short time. In fact, measurements of time in the millisecond range would be necessary to record some clay exchange rates if particle diffusion is the rate limiting step.

EXCHANGE OF ALKALI METAL CATIONS ON A NATURAL STILBITE - L. L. Ames, Jr.

Cation exchange reactions involving sodium, potassium, and cesium with a natural stilbite were investigated. Equilibrium constants of 7.03, 0.132, and 1.03 were derived from the 23 °C isotherms for sodium on the zeolite replaced by cesium, potassium on the zeolite replaced by sodium, and potassium on the zeolite replaced by cesium, respectively. The equilibrium constant for sodium on the zeolite replaced by cesium falls to 1.65 at 85 °C.

The stilbite used in this study was predominantly from the Bay of Fundy region in Nova Scotia. The stilbite was associated with basalt from which it was removed by hand before crushing. The 0.25 to 0.5 mm stilbite fraction was further purified by several passes through a high field strength magnetic separator, resulting in a final stilbite sample that was by X-ray and optical examination of greater than 95% purity. The purified stilbite sample was then ground in an alumina ball mill to -100 mesh, washed with distilled water, and air-dried. All equilibrium data are based on a given weight of the air-dried material with an average water content of 16.6% by weight. A chemical analysis of the purified stilbite is given in Table II.

Cesium and sodium cation exchange capacity determinations on the stilbite are given in Table III. Though the cesium capacity of the stilbite finally equalled the sodium capacity, the time required suggests that a portion of the stilbite structure through which cations must diffuse during exchange reactions approaches the diameter of the cesium cation in size. The slow cesium diffusion may take place through "stacking faults" or distorted eight-membered

Table III. Chemical Analysis and Derived Anhydrous Oxide Formula of the Purified, As-Received, Stilbite Sample.

Constituent	Weight	Formula
SiO_2	71.8	
Al_2O_3	19.6	(0.18 Na, 0.82 Ca) $O \cdot Al_2O_3 \cdot 6.2\ SiO_2$
Na_2O	2.1	
CaO	8.9	
	102.4	

Table III. Variation in Stilbite Capacity as a Function of Equilibration Time

Equilibration Time, hr	Sodium, Meq/g	Cesium, Meq/g
16	1.797	0.981
32	1.831	1.510
64	1.792	1.764

rings in the stilbite crystal structure. The structure of stilbite is, unfortunately, unknown[34] so that structural interpretation of the causes of the relatively slow cesium diffusion is not possible at this time. These results also show that up to 4 days is required to reach equilibrium when cesium is present in the system.

Isotherms at 23 °C for the systems sodium-cesium, sodium-potassium, potassium-cesium, and strontium-cesium with stilbite are given in Figures 17, 18, and 19 respectively. The 85 °C isotherm for sodium-cesium with stilbite also is included in Figure 17. The points in each system represent the experimental values while the line is the probable best interpolation between the experimental points. Graphs of ln K_C versus cation on the zeolite at 23 °C are shown for stilbite in sodium-cesium,

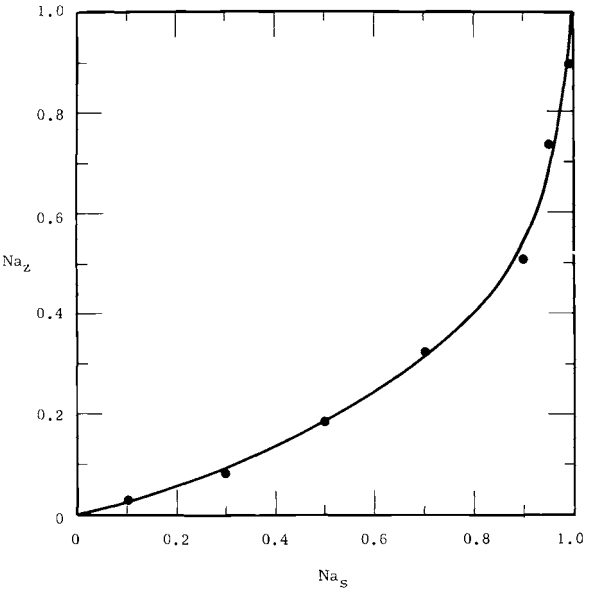

FIGURE 18. The 23 °C Isotherm for the Reaction K_z + Na_s ⇄ Na_z + K_s with Stilbite; Total Equilibrium Solution Normality was Constant at 1.0 (Na_z = Equivalent Fraction of Sodium on the Zeolite; Na_s = Equivalent Fraction of Sodium in the Equilibrium Solution.)

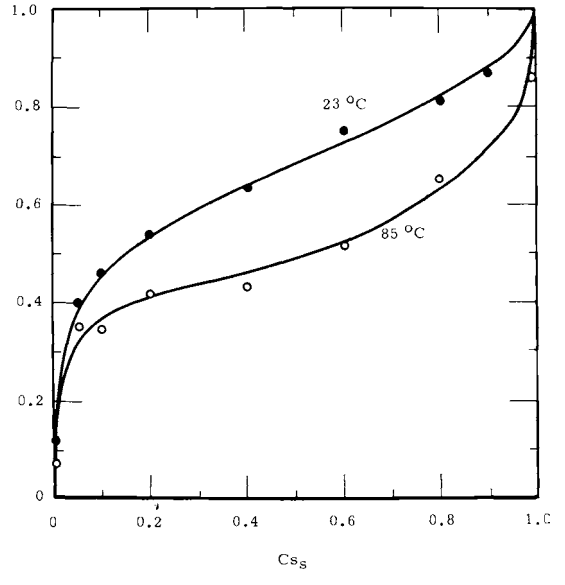

FIGURE 17. The 23 °C and 85 °C Isotherms for the Reaction Na + Cs_s ⇄ Cs_z + Na_s with Stilbite; Total Equilibrium Solution Normality was Constant at 1.0 (Cs_z = Equivalent Fraction of Cesium on the Zeolite; Cs_s = Equivalent Fraction of Cesium in the Equilibrium Solution.)

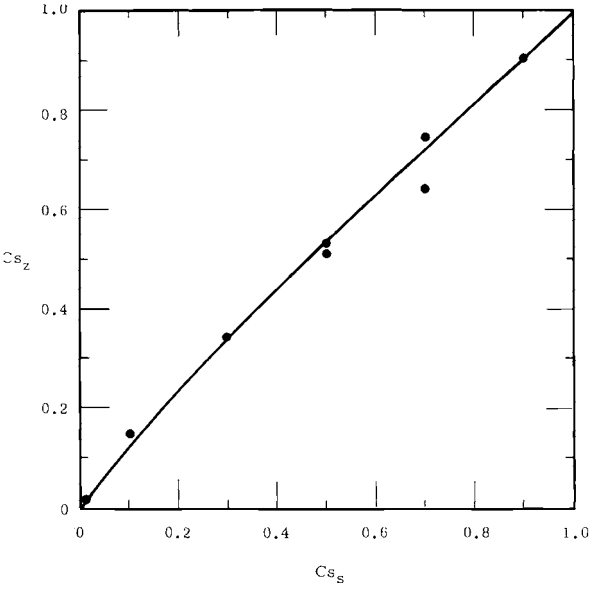

FIGURE 19. The 23 °C Isotherm for the Reaction K_z + Cs_s ⇄ Cs, + K_s with Stilbite; Total Equilibrium Solution Normality was Constant at 1.0 (Cs_z = Equivalent Fraction of Cesium on the Zeolite; Cs_s = Equivalent Fraction of Cesium in the Equilibrium Solution.)

sodium-potassium, and potassium-cesium systems in Figures 20, 21, and 22 respectively. The 85 °C plot also is given in Figure 21. Note that a straight line results in each case in Figures 20, 21, and 22. The rational thermodynamic equilibrium constant, κ, then is equal to the value of ln K_C at the fraction of cation on the zeolite of 0.5. A list of the κ values for the various systems is given in Table IV, along with related free-energy changes. Stilbite falls between Type X and phillipsite in the cesium selectivity data reported by Ames.[35] The free-energy changes for the various exchange reactions balance quite well. The ΔG^O for the reaction ($Na_Z + Cs_S \rightleftarrows Cs_Z + Na_S$) plus the $\Delta G°$ for the reaction ($Cs_Z + K_S \rightleftarrows K_Z + Cs_S$) should equal the ΔG^O for the reaction ($Na_Z + K_S \rightleftarrows K_Z + Na_S$), or (-1156) + (+15) = (-1204). The above balance is in error by 63 calories, a fortuitously small amount considering that such results are usually 100 to 200 calories from a balance.

According to Barrer and Meier,[36] curves of the type shown in Figures 20, 21, and 22 are described by the relationship ln κ = ln K_C + C(1 - 2B_Z), based on the Kielland equation, where B_Z is the fraction of cation B on the zeolite and C is a constant. The C values for each system were computed, and are listed in Table IV.

The single reaction enthalpy shown in Table IV for a stilbite in a sodium-cesium system would seem rather high; but, in view of the steric difficulties with cesium diffusion, the reaction enthalpy may tend to be high. Loss of cesium selectivity could result from thermal effects on a restricted cesium cavity or absorption site.

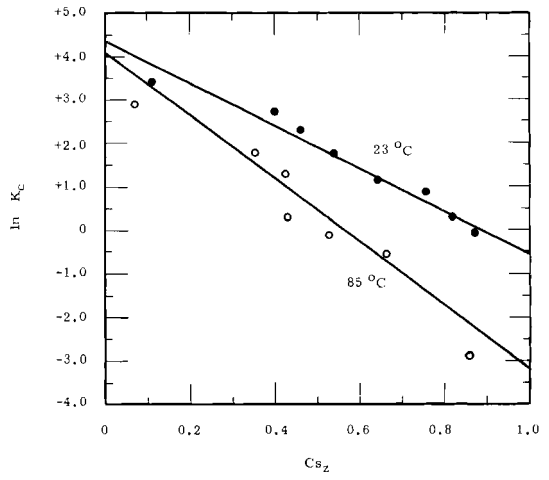

FIGURE 20. Corrected Selectivity Quotient, K_C, Versus the Equivalent Fraction of Cesium on the Zeolite, at 23 and 85 °C for the Reaction $Na_Z + Cs_S \rightleftarrows Cs_Z + Na_S$ with Stilbite

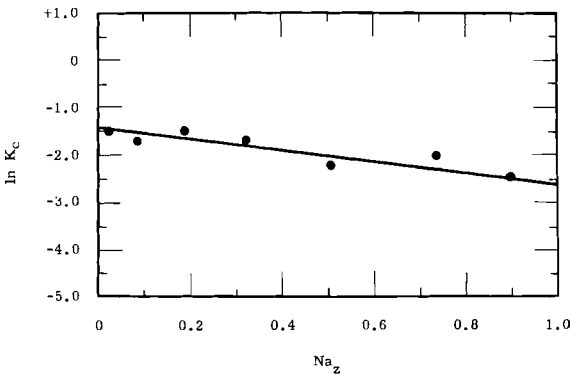

FIGURE 21. Corrected Selectivity Quotient, K_C, Versus the Equivalent Fraction of Sodium on the Zeolite, Na_Z, for the Reaction $K_Z + Na_S \rightleftarrows Na_Z + K_S$ at 23 °C with Stilbite

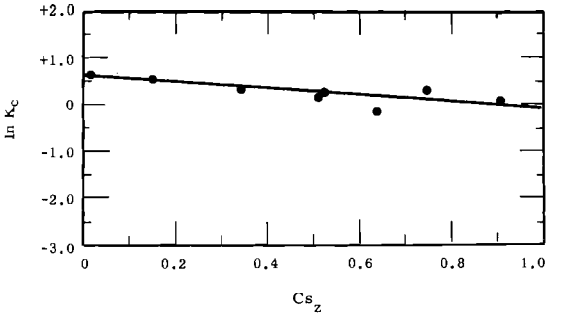

FIGURE 22. Corrected Selectivity Quotient, K_C, Versus the Equivalent Fraction of Cesium on the Zeolite, Cs_Z, for the Reaction $K_Z + Cs_S \rightleftarrows Cs_Z + K_S$ at 23 °C with Stilbite

Table IV. Stilbite Thermodynamic Data; κ is a Rational Thermodynamic Constant, ΔG^O is the Standard Gibbs Free-Energy Change, and ΔH^O is a Reaction Enthalpy (the Subscript "z" Refers to the Cation on the Zeolite and the Subscript "s" to the Cation in the Solution.)

Exchange Reaction	Temperature, °C	κ	ΔG^O, cal/mole	ΔH^O, cal/mole	C
$Na_z + Cs_s \rightleftarrows Cs_z + Na_s$	23	7.03	-1156	-4920	-2.5
$Na_z + Cs_s \rightleftarrows Cs_z + Na_s$	85	1.65	-297		-3.7
$K_z + Na_s \rightleftarrows Na_z + K_s$	23	0.131	+1204		-0.6
$K_z + Cs_s \rightleftarrows Cs_z + K_s$	23	1.03	-15		-0.5

ALKALI METAL CATION EQUILIBRIA WITH CHABAZITE— L.L. Ames, Jr

Chabazite euqilibria were studied in the systems sodium-potassium, sodium-cesium, and cesium-potassium at 23 °C. The Gibbs free-energy change derived from the isotherm for the reaction $Na_{zeolite} + K_{solution} \rightleftarrows K_{zeolite} + Na_{solution}$ showed good agreement with Barrer's chabazite results for the same system. Only 85% of the 3.53 sodium atoms per unit cell, or 3.00 cesium atoms, were contained in the chabazite cell at equilibrium. These equilibria can be explained in terms of the chabazite crystal structure given by Smith.

The chabazite used in this study was originally from the Bay of Fundy region of Nova Scotia. The as-received chabazite contained basalt rock as the major impurity. Consequently, the chabazite was hand picked free of basalt, as far as possible, and the clean fraction crushed. The 0.25 to 0.5 mm size of the clean, crushed fraction was passed through an electromagnetic separator several times to insure a basalt-free chabazite fraction for study. The resulting clean fraction was crushed to -100 mesh, washed with distilled water, and air-dried at room temperature. Water loss on ignition to 700 °C of the clean, powdered, air-dried zeolite was 19.1 wt %. All subsequent zeolite capacity determinations include the above weight percent water as a part of the zeolite weight. A chemical analysis of the as-received but purified chabazite is given in Table V.

Table V. Chemical Analysis of the Anhydrous Chabazite Sample Used in This Study and Derived Unit Cell Contents

Constituent	Wt %	Unit Cell Contents
SiO_2	66.6	
Al_2O_3	22.8	
CaO	12.3	$Na_{0.09}Ca_{1.72}Al_{3.47}Si_{8.51}O_{24}$
Na_2O	0.7	
	102.4	

The chabazite isotherm for sodium-potassium equilibrium at 23 °C is given in Figure 23. Note that the chabazite is highly unselective for sodium in the presence of potassium. The selectivity coefficients of the experimental points given in Figure 23 were determined, corrected with the appropriate mean activity coefficient ratio, and plotted as the natural log of the corrected selectivity quotient (ln Kc) versus the equivalent fraction of sodium on the zeolite (Na_z) as shown in Figure 24. The thermodynamic equilibrium constant (κ) derived from the data of Figure 24 was 0.0708, and the free-energy change was + 1570 cal/mole. The above values may be directly compared to values given by Barrer and Sammon[37] for a chabazite very similar in chemical composition to that utilized in this study. The comparable equilibrium constant given by Barrer and Sammon was 0.0752 (1/13.3) and a free energy change of +1530 cal/mole. Within the experimental error, they are the same values. The relationship $\ln \kappa = \ln Kc + C(1 - 2Na_z)$, based on the Kielland equation, describes the curve shown in Figure 24. Na_z is sodium on the zeolite and C is a constant, -0.42 in the above case.

Chabazite binary systems containing cesium were of special interest because the cesium capacity was not the same as the sodium or potassium capacity. Chabazite sodium and potassium capacities averaged 2.59 meq/g, while the cesium capacity was 2.20 meq/g. Extended equilibrations (up to 10 days) yielded cesium capacity results very similar to the 2 day equilibrations. Equilibrium was attained in a normal 2 day equilibration time, so that poor cesium kinetics were not a contributing factor to the low cesium capacity.

The plotting of cation exchange data in the standard form of an isotherm required modifications because of the different exchange capacities of the two cations.

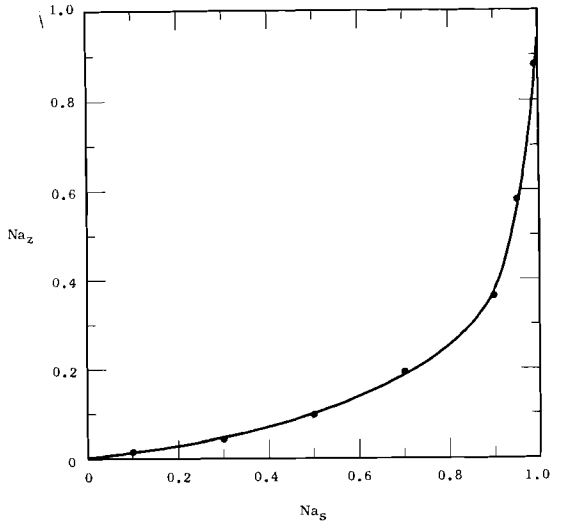

FIGURE 23. The 23 °C Isotherm for the Reaction $K_z + Na_s \rightleftarrows Na_z + K_s$ with Chabasite; Total Equilibrium Solution Normality was Constant at 1.0 (K_z, Na_z = Equivalent Fraction of Potassium or Sodium on the Zeolite; K_s, Na_s = Equivalent Fraction of Potassium or Sodium in the Equilibrium Solution.)

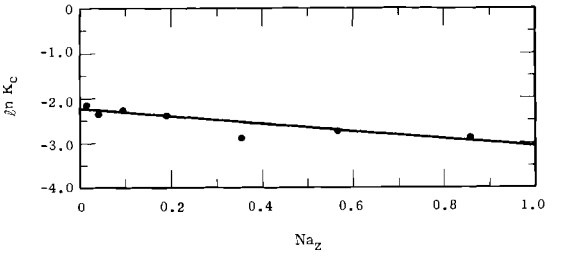

FIGURE 24. Natural Log of the Corrected Selectivity Quotients (ln Kc Versus the Equivalent Fraction of Sodium on the Zeolite (Na_z) for the Reaction $K_z + Na_s \rightleftarrows Na_z + K_s$ at 23 °C with Chabazite

Two scales were used for the equivalent fraction of cation on the zeolite as seen in the data of Figure 25. Cesium on the zeolite at 1.0 is 2.20 meq/g, and sodium on the zeolite at 1.0 is 2.59 meq/g. Note that cesium zeolite loading begins at 15% sodium loading, or the equivalent fraction on the zeolite at 1.0 cesium in the solution is 85% cesium on the zeolite plus 15% sodium on the zeolite. The potassium-cesium isotherm is presented in the same manner in Figure 26.

The failure of chabazite to exchange sodium for cesium completely can be explained on the basis of the structure of chabazite as elucidated by Smith.(38) The basic feature of the chabazite structure is a distorted ditrigonal prism of two six-membered rings. The main chabazite absorption cavity is 6 to 7 Å diam, 10 Å long, and contains four-, six-, and eight-membered rings. As Smith reported, some of the larger cations such as cesium should be able to occupy the 3 to 4 Å, eight-membered rings, bonding across the aperture. There are six eight-membered rings per unit cell so that the theoretical four exchangeable sodium cations per unit cell would be displaced by only three cesium ions per unit cell (each eight-membered ring is shared)

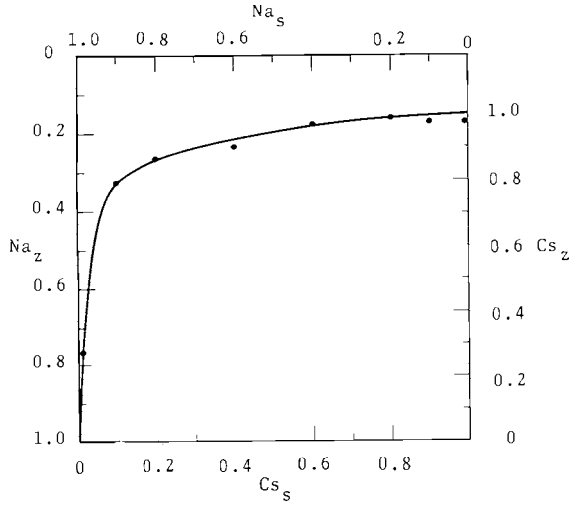

FIGURE 25. The 23 °C Isotherm for the Reaction $Na_z + Cs_s \rightleftarrows Cs_z + Na_s$ with Chabazite; Total Equilibrium Solution Normality was Constant at 1.0 (Cs_z, Na_z = Equivalent Fraction of Cesium or Sodium on the Zeolite; the Equivalent Fraction of Sodium on the Zeolite is Plotted as a Fraction of the Chabazite Sodium Capacity of 2.59 meq/g; the Equivalent Fraction of Cesium on the Zeolite is Plotted as a Fraction of the Chabazite Cesium Capacity of 2.20 meq/g; Cs_s. Na_s = Equivalent Fraction of Cesium or Sodium in the Equilibrium

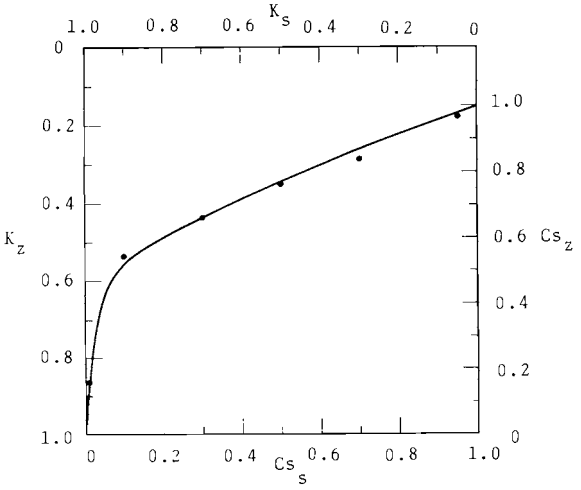

FIGURE 26. The 23 °C Isotherm for the Reaction $K_z + Cs_s \rightleftarrows Cs_z + K_s$ with Chabazite; Total Equilibrium Solution Normality was Constant at 1.0 (Cs_z, K_z = Equivalent Fraction of Cesium or Potassium on the Zeolite; the Equivalent Fraction of Potassium on the Zeolite is Plotted as a Fraction of the Chabazite Potassium Capacity of 2.59 meq/g; the Equivalent Fraction of Cesium on the Zeolite is Plotted as a Fraction of the Chabazite Cesium Capacity of 2.20 meq/g; Cs_s, K_s = Equivalent Fraction of Cesium or Potassium in the Equivalent Solution.)

plus a remaining sodium ion within the main adsorption cavity that could not be displaced because of the cesium spatial requirements. The unit cell contents of exchangeable sodium for the chabazite of this study is 3.53 atoms per unit cell, as shown in Table V. If the final cesium content of the chabazite unit cell is 85% of the original sodium content, the cesium content is 85% of 3.53 sodium atoms or 3.00 cesium atoms plus 0.53 sodium atoms per unit cell. It would seem, therefore, that the cesium atom does occupy the eight-membered ring aperture, while sodium and potassium, being smaller in diameter, probably occupy positions within the main adsorption cavity of chabazite.

UNIT CELL SIZE AND CESIUM LOADING ON TYPE A AND TYPE X ZEOLITES - L. L. AMES, JR.

A study was made to determine whether a correlation existed between cesium loading and zeolite unit cell size similar to a reported correlation between calcium loading and Type A unit cell size. The latter correlation was confirmed, but no pronounced cesium loading-unit cell size correlation was noted. The possibility exists that changes in water plus cation volume could give rise to a curve of the reflective sort.

Barrer and Sammon[37] and Barrer and Meier[39] have reported a maximum in unit cell dimensions of chabazite and Type A zeolites which reflects a maximum in the sodium-calcium exchange data. They have suggested that the distribution of cations with minimum free-energies exists for certain sodium plus calcium compositions in Type A and chabazite and explains the presence of reflective maxima. The present investigation was to confirm the presence of the maxima and to determine whether they also occured in sodium-cesium system with Type A or Type X.

The maximum in the Type A half-unit cell dimensions when plotted versus the fraction of calcium on the zeolite at 70 °C resembles the curve given by Barrer and Meier[39] at 100 °C as shown in Figure 27. The main difference is that the maximum of the curve shown in Figure 27 does not attain the maximum log κ_C value shown in Barrer and Meier's curve. The reasons for the curve may be temperature or zeolite compositional differences[35] (the 25 °C curve showed no maximum of the above type)[40] or different data treatment methods. The point to be made is that the maxima do exist and are approximately reflective.

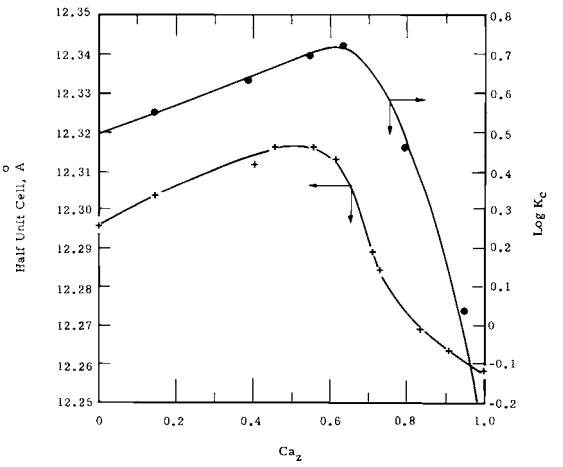

FIGURE 27. Log K_C Versus Ca and Half-unit Cell Dimensions versus Fa, for Type A Zeolite in a Sodium-Calcium System at 70 °C (K_C = a Mass Action Quotient Corrected for Equilibrium Solution Activities; Ca_z = an Equivalent Fraction of Calcium on the Zeolite.)

Barrer and Meier[36] give values of and 12.253 ± 0.003 Å for calcium-Type A, while the values found in this work were 12.296 ± 0.003 Å and 12.258 ± 0.003 Å for sodium and calcium-Type A, respectively. The agreement is good considering the probable differences in zeolite hydration states. The half-unit cell is used here because it is the dimension obtained in this instance rather than the unit cell.

The log κ_C versus cesium on the zeolite are shown for Type X in Figure 28. The two curves do not show maxima in a sodium-calcium system, but the curves are reflective in that they fall and rise together. The sodium-cesium curves for Type A are not reflective as seen in Figure 29. The curve of log κ_C versus cesium on the Type A falls rapidly while the curve of half-unit cell versus cesium on the Type A actually rises. If the relatively large magnitude changes in the curves shown in Figure 27 are caused by differences in cation plus water volume within Type A, at least an equally large effect of cation plus water volume change should be found in a cesium-sodium system. Barrer and Meier[39] consider the ion-exchanged forms of Type A but do not give data for the intermediate ion-exchanged forms with the exception of the sodium-calcium system compositions. Therefore, the shape of the curve of half-unit cell versus the intermediate sodium-cesium compositions was unknown. That there are slight differences in unit cell dimensions due to changes in the volume of cations plus water is probable from the data shown in Figure 29. The magnitude of the unit cell dimensions changes in Figure 29 are relatively small compared to the unit cell changes shown in Figure 27 for the sodium-calcium system. It is concluded, therefore, that the cation plus water changes of Type A are relatively small and cannot account for the relatively large unit cell

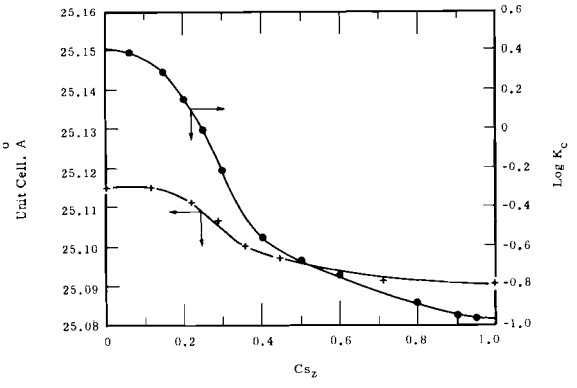

FIGURE 28. Log K_C Versus Cs, and Unit Cell Dimensions Versus Cs, for Type X Zeolite in a Sodium-Cesium System at 25 °C (K_C = a Mass Action Quotient Corrected for Equilibrium Solution Activities; Cs, = an Equivalent Fraction of Cesium on the Zeolite.)

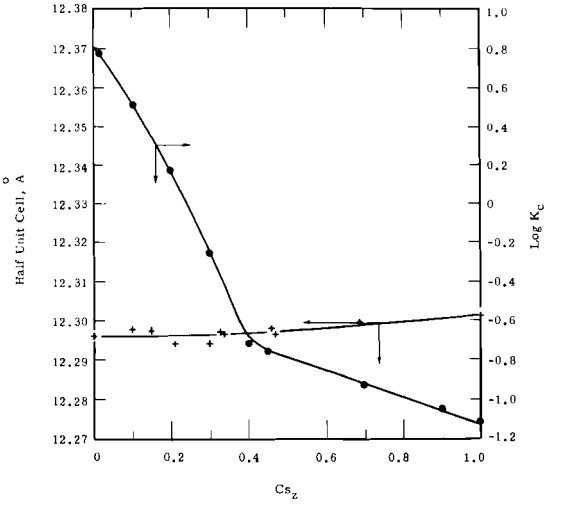

FIGURE 29. Log K_C Versus Cs_z and Half-unit Cell Dimensions Versus Cs_z for Type A Zeolite in a Sodium-Cesium System at 25 °C (K_C = a Mass Action Quotient Corrected for Equilibrium Solution Activities, Cs, = an Equivalent Fraction of Cesium on the Zeolite.)

size changes of Type A in a sodium-calcium system. Barrer and Meier's suggestion of a minimum free-energy for certain sodium-calcium compositions is still pertinent. On the other hand, the data for Type X shown in Figure 28 suggest that changes in water plus cation volume probably can give rise to curves of the reflective sort for other zeolites.

CATION EXCHANGE PROPERTIES OF WAIRAKITE AND ANALCIME - L. L. Ames, Jr.

Strontium and calcium based analcimes were synthesized and their cation exchange properties compared with those of natural and synthetic wairakites. Not even calcium self-exchange was exhibited by the wairakites. Strontium self-exchange was absent on calcium and strontium analcimes. Wairakite occupies a position in the analcime series analogous to pollucite.

Calcium- and strontium-based analcimes were made by a method similar to that reported by Hoss and Roy.[41] Sodium-based natural phillipsite from Nevada, approximately $Na_2O \cdot Al_2O_3 \cdot 4SiO_2 \cdot 5H_2O$, was based with calcium or strontium, placed in a 150 ml bomb with 2 g of calcium or strontium hydroxide, and held at 15,000 psi hydrostatic pressure and 280 °C for 7 days. Two such treatments were given the material in one instance, but the X-ray diffraction pattern showed little change as a result of the extra hydrothermal treatment.

The wairakite was synthesized from Ludox SM silica suspension and calcined nitrates of aluminum and calcium in a 150 ml bomb for 30 days at 315 °C and 15,000 psi hydrostatic pressure. The starting composition was $CaO \cdot Al_2O_3 \cdot 5SiO_2$.

The natural wairakite was from the 2750 ft level of Drillhole 218 at Wairakei, New Zealand. The wairakite occurrence at Wairakei was described by Steiner.[42,43] X-ray diffraction patterns of the wairakite and Nevada phillipsite used in this study are given in Figure 30.

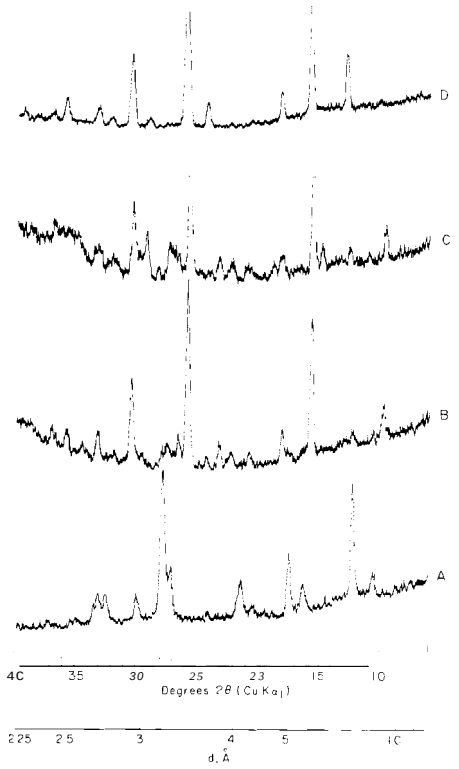

FIGURE 30. X-Ray Diffraction Tracings of (A) Nautral, Calcium-based, Nevada Phillipsite; (B) Synthetic, Calcium-based Analcime Derived from (A); (C) Synthetic, Strontium-based Analcime Derived from Strontium-based (A); and (D) Natural Wairakite Used in this Study

The analcime cation exchange capacities for different cations, such as sodium and strontium, are markedly dissimilar. While a previously employed, double-tracing technique for zeolite capacity determinations may be satisfactory for the determination of a composite binary system capacity, it would be of value in the present study to know the absolute zeolite capacity for each cation. Hence another technique, that of isotopic dilution, was used. Isotopic dilution as applied to exchange capacity determinations can be summarized as follows:

$$N_o = \frac{A_a \cdot N}{A_s} - N \qquad (1)$$

where

N_o = cation exchange capacity
N = milliequivalents of cation in the equilibrating solution
A_a = original tracer counts in the equilibrating solution
A_s = final tracer counts in the equilibrating solution.

The zeolite sample is first based using tne cation with which the capacity is to be measured. The zeolite is then washed clean of extraneous basing cations and contacted with a solution containing a known number of milliequivalents of basing cation plus the same radioactive tracing cation. For sodium, for example, the zeolite is based with sodium, washed until sodium-free wash water is obtained, and contacted with a solution containing sodium plus ^{22}Na. The capacity for the given cation is determined by using the relationship given in Equation (1).

The exchange capacities, as determined with sodium, caicium, and strontium, of the analcimes and wairakites are given in Table VI. The pure synthetic analcime had a negligible calcium and strontium capacity, as reported previously by Barrer.[8] Cation diameter rises from 1.88 Å for Na^+ to 2.24 Å for Sr^{2+}. Cation size is not the whole explanation since potassium-, ammonium-, rubidium-, and thallium-based analcimes are known,[44] containing twice as many cations as a strontium-based analcime and often of larger diameter than Sr^{2+}

"able VI. The exchange capacities of the carious analcimes and wairakites as measured by an isotopic dilution method at 25 °C (The synthetic analcimes were made by hydrothermal treatment of natural phillipsite.)

Zeolite Sample	Cation Exchange Capacity, meq/g		
	Na^+	Ca^{2+}	Sr^{2+}
Wairakei Wairakite (natural)	nd(a)	nd	nd
Calcium-based analcime (synthetic)	1.5	1.5	nd
Strontium-based analcime (syntheticj	1.1	1.1	nd
Wairakite (synthetic]	nd	nd	nd

(a) nd = less than 0.03 meq/g

According to W. H. Taylor,[45] the aperture size of analcime is 2.8 Å, certainly large enough to accommodate a 2.24 Å diameter strontium cation. Perhaps a combination of unfavorable cation size and cation spatial distribution is responsible for the low strontium capacity of natural analcime, as suggested by Barrer.[44] The results of this study suggest, in addition, that the cause of analcime having calcium capacity at all is the presence of calcium or strontium during the formation of the analcime.

Calcium-based analcime, however, shows the same sodium and calcium capacity but a negligible strontium capacity. Strontium-based analcime likewise has the same sodium as calcium capacity as well as a negligible strontium capacity (less than 0.03 meq/g). Assuming that the cation exchange behavior of the calcium- and strontium-based analcimes also is influenced by a combination of cation size and spatial distribution in respect to the anionic sites, certain structural differences among the analcimes are apparent. The spatial positions of the calcium and strontium in their respective analcimes can be specifically "tailored" to held those cations when synthesized with calcium or strontium only, This "tailoring" probably results in a distorted sodium-analcime structure.

The lack of strontium-strontium exchange by even the strontium-based analcime probably Indicates that the strontium cation is too large. considering the structural "tailoring" necessarily imposed on the normal analcime structure by synthesis from strontium cations only, to allow two-way strontium self-diffusion and self-exchange. The smaller calcium and sodium cations can diffuse and exchange with the strontium. Wairakite is another structure, entirely adapted to accommodate divalent calcium ions only. Further, the calcium ions are not exchangeable--as indicated by lack of a measurable calcium or sodium cation exchange capacity. Wairakite, then, occupies a position in the alkaline earth metal cation series analogous to pollucite in the alkali metal cation series. Based on the X-ray data and apparently metastable character of Barrer and Marshall's strontium analcime, it is doubtful that a stable strontium-analcime exists. The ion exchange character of strontium- and calcium-based analcimes is apparent from the isotherms presented in Figure 31. Note that while the sodium and calcium exchange capacities of the two analcimes are not the same, their exchange isotherms are quite similar when plotted on fractional scales as shown in Figure 31. The strontium-analcime was exchanged to calcium-analcime before equilibration with sodium-calcium solutions. The preference of both zeolites for sodium is marked indicating, in the author's opinion, that analcimes of this type are distorted sodium-analcimes that partially revert to the simple cubic structure of sodium-analcime when contacted with sodium cations. The occurrence of calcium- or strontium-based analcimes in nature would be

highly unusual because of their tendency to revert to a normal, but non-cubic, sodium-analcime. These cation exchange results support the view of Steiner[43] and of Coombs[46] who suggested that if an analcime-wairakite series existed, isomorphous substitutions of calcium for sodium were very limited.

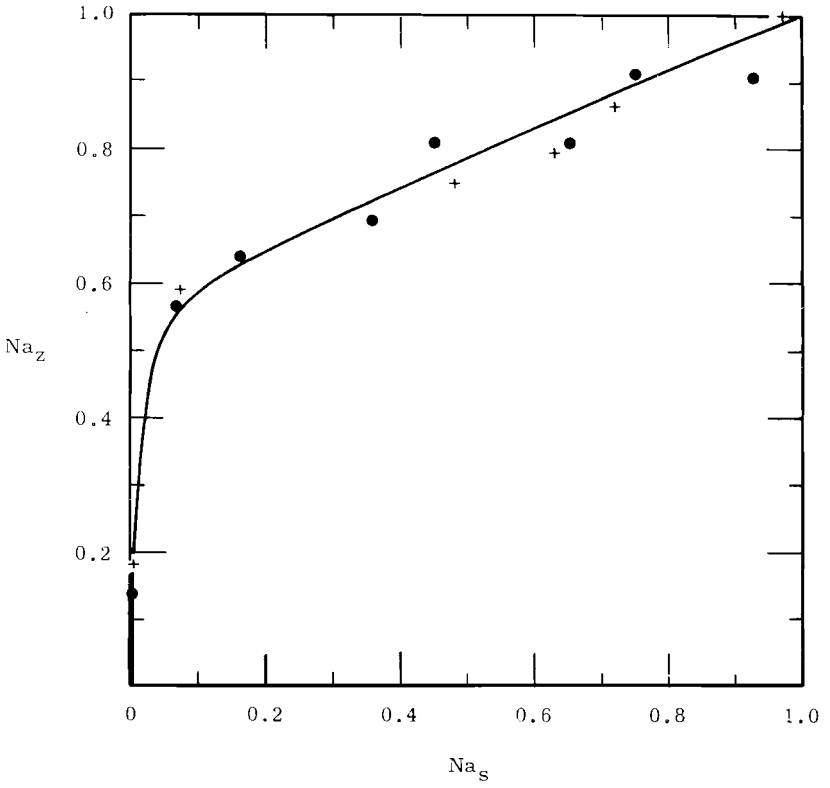

FIGURE 31. The 25 °C Isotherm for the Reaction Ca, + $2Na_s \rightleftarrows 2Na_z$ + Ca_s (Total Equilibrium Solution Normality was Constant at One; Na_z = the Equivalent Fraction of Sodium on the Zeolite; Na_s = the Equivalent Fraction of Sodium in the Equilibrium Solution.l

- ● = *Equilibrium Composition of Calcium-based Analcime and Solution with the Analcime Made by Hydrothermal Treatment of Calcium-based Phillipsite; Cation Exchange Capacity = 1.5 meq/g.*
- \+ = *Equilibrium Compositions of Calcium-based Analcime and Solution with Analcime Made from Calcium Exchange of Strontium-based Analcime, in Turn Made from Hydrothermal treatment of Strontium-based Phillipsite; Cation Exchange Capacity = 1.1 meq/g.*

RADIONUCLIDE MIGRATION IN SOIL COLUMNS - DEVELOPMENT OF A COMPUTER PROGRAM -

B. F. Hajek

A method to predict radionuclide distribution and breakthrough concentrations was developed for simple soil-solution systems. Input data consist of the equilibrium distribution coefficient, weight of soil and volume of soil solution. Experimental and calculated ^{32}P breakthrough curves agreed satisfactorily with the relative breakthrough concentration of 60%.

A method to predict radionuclide distribution and breakthrough concentrations in soil columns has been developed for simple systems. The method is similar to one developed by G. R. Dutt to predict the quality of percolating water.[47] A program of the method has been prepared, and calculated results have been compared to an experimental phosphate (^{32}P) breakthrough curve. Reaction rates and flow rate variables have not been included; however, when expressions for these effects are developed, they can be included.

The method considers the soil column to be made up of n segments Δx in length. The total column length is given by the expression

$$L = \sum_{i=1}^{n} \Delta x_i \qquad (1)$$

where i designates the particular segments. If C is the initial concentration of the radionuclide in solution and q is the amount of solution in each segment i, the final concentration C' in the first aliquot, q, coming from the column will be

$$C' = C + \sum_{i=1}^{n} \Delta C_i \qquad (2)$$

where ΔC_i is the change in concentration of the radionuclide when the allquot q is passed through segment i. As $n \to \infty$ the last term in Equation (2) would be the integral of the change in radionuclide concentration from 0 to L, and ΔC_i would approach the difference between the concentration resulting when the entering solution was brought into equilibrium with segment i.

A method for calculating equilibrium solution concentrations of radionuclide is available from the equilibrium distribution coefficient (K_d) expression,

$$K_d = \left(\frac{C - C_1}{C_1}\right)\left(\frac{ml}{W}\right) \qquad (3)$$

in which W is the weight of soil, ml is the volume of solution, and C_1 is the equilibrium concentration. Equation (3) can be written to include an initially adsorbed quantity, that is

$$K_d = \frac{Q + y}{b - \frac{yW}{ml}} \qquad (4)$$

in which y is the amount of activity per gram of soil leaving or entering the soil exchange complex when brought into contact with a solution with initial concentration b, and Q is the initial adsorbed concentration per gram of soil. It is evident that at equilibrium Q + y is adsorbed activity or

$(C - C_1)$ ml/W and b - yW/ml = equilibrium solution concentration or C_1. The computer program was developed to compute C_1 and Q values for each segment i. Input data consisted of values for the initial concentration, K_d, tile weight of soil per segment, and the volume of solution per segment.

Figure 32 shows the agreement between experimental and calcuiated results. Agreement to C/C_o = 0.6 is satisfactory; however, prediction of breakthrough beyond this concentration will necessitate the addition of terms to the Kd expression.

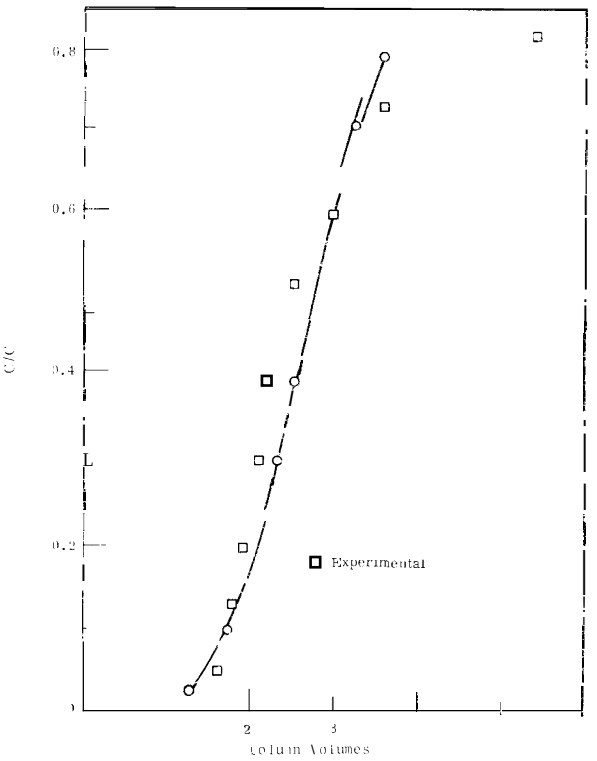

FIGURE 32. Calculated and Experimental $^{32}PO_4^{\equiv}$ Breakthrough

DISPERSION CHARACTERISTICS OF STRONTIUM IN SOIL COLUMNS - B, F. Hajek

Dispersion experiments were conducted with strontium in soil columns. A mathematical madel was compared to the experimental data and was found to predict adequately the strontium distribution in soil columns.

The dispersion characteristics were studied of a 0.1N strontium solution, traced with ^{85}Sr, which replaces and is replaced by a 0.1N calcium solution in soil columns. The experiments were conducted to ascertain the usefulness of a mathematical model in predicting the distribution within columns and the shapes of breakthrough curves. The distribution of strontium was determined, after various intervals of flow, by scanning the column with a NaI(Tl) scintillation crystal coupled to a single-channel analyzer. The activity was recorded as a function of distance from the column influent end.

The differential equation often used to describe the concentration distribution of a solute in a one-dimensional porous medium flow system[48] is Equation (1).

$$b \frac{\partial C}{\partial t} + v \frac{\partial C}{\partial x} = D \frac{\partial^2 C}{\partial x^2} . \qquad (1)$$

The solution of this equation with initial and boundary conditions corresponding to those in this study has been given[49] as

$$\frac{C}{C_o} = 1/2 \left[\left(\operatorname{erfc} \frac{x - \frac{v}{b} t}{2\sqrt{\frac{Dt}{b}}} \right) \right] + \left[\exp \frac{vx}{D} \operatorname{erfc} \left(\frac{x + \frac{v}{b} t}{2\sqrt{\frac{Dt}{b}}} \right) \right] \qquad (2)$$

in which:

D = dispersion coefficient

v = seepage velocity

x = distance

t = time

$b = 1 + \frac{X}{N} \theta$

θ = porosity

X = volumetric exchange capacity

N = solution normality

Dimensionless quantities can be introduced and the equation can be expressed as:

$$\frac{C}{C_o} = 1/2 \left[\operatorname{erfc} \left(\frac{1 - \xi}{2\sqrt{\xi\kappa}} \right) + \exp \operatorname{erfc} \left(\frac{1 + \xi}{2\sqrt{\xi\kappa}} \right) \right] \qquad (3)$$

in which

$$\xi = \frac{\bar{v}t}{x}$$

$$\kappa = \frac{D_{Ca}^{Sr}}{vx}$$

$\bar{v} = \frac{v}{b}$ = solute velocity

It has been shown that for values of $\kappa < 0.1$, the second term in the bracket is negligible.[48] Then the equation reduces to:

$$\frac{C}{C_o} = 1/2 \operatorname{erfc} \left(\frac{1 - \xi}{2\sqrt{\xi\kappa}} \right) \qquad (4)$$

and a logarithmic probability plot of C/C_o versus ξ gives essentially a straight line for all values of $\kappa < 0.1$.

Values of D may be obtained by matching experimental data to a family of C/C_o curves plotted for various values of κ in equation (3).

Measured and calculated distribution curves of strontium after 210 and 270 min of flow at 0.176 ml/cm^2/min are shown in Figure 33. The dispersion coefficient was obtained from the measured distribution after 60 min flow.

Figure 34 shows a measured and calculated distribution of a 60 min pulse of 0.1N strontium followed by a 0.1N calcium eluting solution. Dispersion coefficients of both the invading and elution fronts were determined from separate loading and elution experiments.

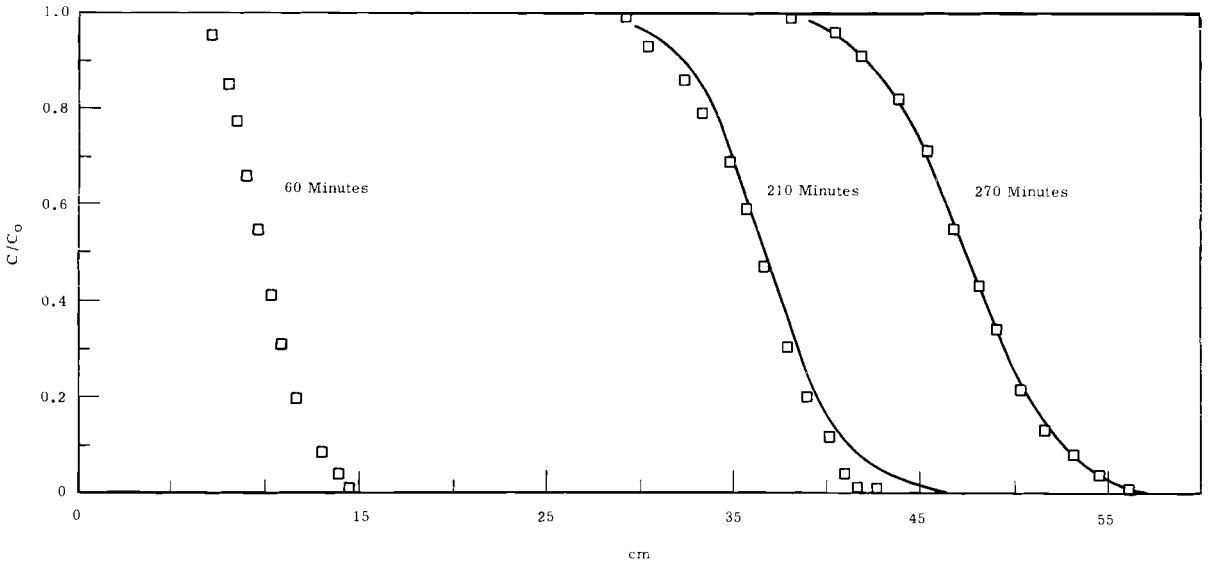

FIGURE 33. Calculated Curves and Experimental Points for Strontium Distribution in Soil Column

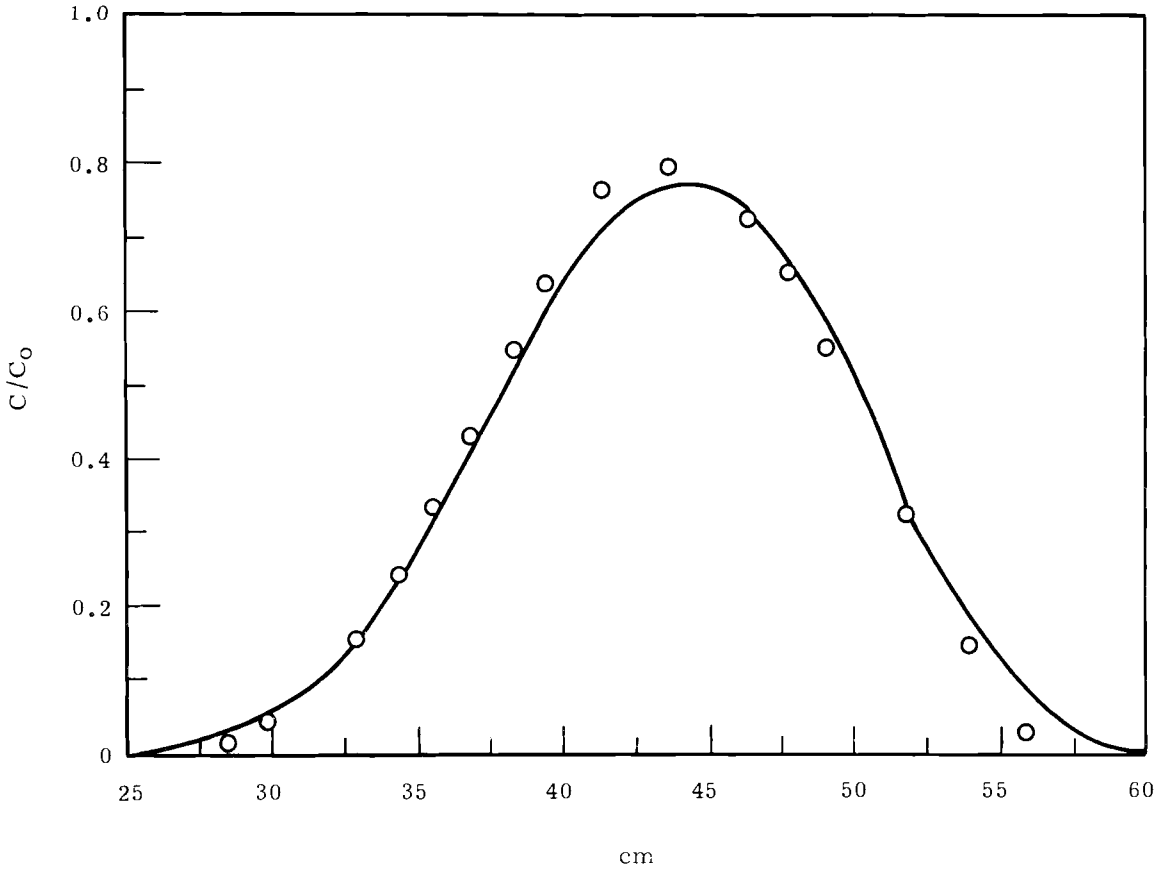

FICURE 34. Calculated and Experimental Strontium Distribution Following a Slug Injection into Soil Column

The distribution curve shown in Figure 34 was calculated for a slug injection where the solute is injected for a finite time t', i. e., from zero to t_o. By introducing this time into Equation (3) the equation for breakthrough of a slug injection is,

$$\frac{C}{C_o} = \left[1/2 \text{ erfc } \left(\frac{1 - \xi'}{2\sqrt{\xi'\kappa'}}\right) - \text{erfc}\left(\frac{1 - \xi}{2\sqrt{\xi\kappa}}\right)\right]$$

$$+ 1/2 \exp \frac{1}{\kappa} \left[\text{erfc}\left(\frac{1 + \xi'}{2\sqrt{\xi'\kappa'}}\right) - \text{erfc}\left(\frac{1 + \xi}{2\sqrt{\xi\kappa}}\right)\right] \qquad (5)$$

where $\xi' = \frac{t'v}{bx}$

$$\kappa' = \frac{D^{Ca}_{Sr}}{vx}$$

The agreement between measured and calculated distributions is satisfactory; however, previous studies[50] have indicated that the dispersion coefficient is not a constant at all flow velocities. For this reason further studies are needed for other systems and at various flow rates.

CESIUM FND STRONTIUM DISTRIBUTION BENEATH LIQUID WASTE DISPOSAL SITES—
J. R. Raymond

Investigation was made of radiocontaminant concentrations and distribution beneath selected liquid waste disposal facilities. Additional wells were drilled and core samples taken of the earth materials for laboratory analysis. The bulk of the long-lived radioisotopes, such as ^{137}Cs and ^{90}Sr, was found retained high in the soil column some 100 ft or more above the regional water table. Thus the effectiveness of the soil in removing certain radioisotopes by absorption and ion exchange is confirmed.

Low and intermediate level liquid radioactive wastes have been disposed to the ground at Hanford for the past 22 years. Studies of the areal and vertical distribution of the radiocontaminants in the subsoils at disposal sites have generally oeen qualitative. Predisposal monitoring wells are logged with scintillation detection equipment to determine location of gross gamma emitting isotopes, and the well water is routinely sampled to detect presence of radioactivity in the ground water adjacent to the disposal sites. The logging and sampling give little or no information about the distribution of the radioisotopes in the ground and only relative gross gamma concentrations. Several waste disposal locations were selected for further investigation to determine the migration, location and

concentration of critical isotopes (mainly ^{137}Cs and ^{90}Sr) in the subsoils. The waste facilities for study were chosen on the bases of wastes received, operational history, and potential hazard from radioisotope breakthrough.

Investigation was conducted by drilling wells through or very near the disposal cribs and by sampling and analyzing the soil. The drilling was done with a cable-tool machine, utilizing a drive-type core barrel. The hollow core sampling barrel was driven into the ground with the drill stem and jars and then extracted. The soil material remained in the core barrel and was removed at ground surface. No fluid or extraneous materials were added to the hole during drilling to assure that the subsurface samples were uncontaminated and largely undisturbed. A clean hole technique was used by keeping casing driven very near to hole bottom to minimize cross contamination of the soil material. Samples were taken routinely at 5 ft depth intervals with additional samples taken where formation material size or composition changed or where a change occurred in radiation level.

Drilling samples were sent to the laboratory for radiometric analysis when the field survey indicated presence of radiocontaminants. Determination of sample radioactivity in the field was made with portable survey instruments when radiation levels were relatively high and with a shielded scintillation sample-counter for low radiation levels. Laboratory radiometric analyses were made for gamma-emitting isotopes by direct scintillation counting in a well crystal with a multichannel spectrum analyzer. ^{90}Sr analysis was made by soil fusion, chemical separation, and beta counting.

Well locations were selected by analysis of scintillation probe data from existing monitoring wells and by evaluation of facility input histories. In general, well placement was designed to sample the worst condition at each facility and to penetrate zones of highest radioactivity density.

Figure 35 shows the ^{137}Cs and ^{90}Sr concentrations in samples from test well E33-2A adjacent to one crib in an eight-crib disposal facility that received a moderate volume of a high-salt, intermediate level waste. The disposal site was in service from December, 1954, to December, 1955, and received 3.4×10^7 liters and 4.1×10^5 gross beta Ci of scavenged waste. The waste contained 3300 Ci of ^{137}Cs and 12,900 Ci of ^{90}Sr. Concentration in microcuries per gram of soil (Ci/g) is plotted against depth below ground surface. The radioactivity content is plotted on a logarithmic scale because of the large range of values. ^{137}Cs was first detected at 17 ft below ground surface (approximate crib bottom) at a concentration of 18.4 Ci/g of soil. The ^{137}Cs contamination rises to a high of 28.7 Ci/g at 20 ft and then rapidly decreases with depth. Several additional maxima occur lower in the soil column but only on the order of 1×10^{-3} to 1×10^{-4} of the peak concentration. Ground water is 220 ft below ground surface at this

site, ^{90}Sr-^{90}Y follows the same general pattern as cesium with a high concentration of 44 Ci/g of soil occurring at 24.8 ft below ground surface. Samples below 75 ft contain less than 5 x 10^{-3} Ci/g of ^{90}Sr. ^{106}Ru-^{106}Rh, a major input isotope, was not detected, which indicates almost complete decay during the 10 year period that the facility has been out of service.

Figure 36 shows the subrurface radioactivity concentration at well site E24-1A adjacent to a 35 ft square crib that received a large volume of low level, low-salt process condensate waste from hovember, 1955, to October, 1961. Total disposal was 3400 gross beta Ci (mostly ^{106}Ru-^{106}Rh) including only an estimated 4 Ci each of ^{90}Sr and ^{137}Cs. However, column volume throughput was the highest of any waste disposal facility on the Hanford Project (1.8 x 10^{9} liters or 180 column volumes). Figure 36 shows that ^{137}Cs decreases rapidly from a moderate level of 5.4 x 10^{-3} Ci/g at 35 ft to a low level of 1 x 10^{-5} Ci/g at about 65 ft. Throughout the rest of the soil column, ^{137}Cs values are at or below the detection limit of 10^{-6} Ci/g. ^{106}Ru-^{106}Rh concentration, though of no concern because of the short half-life, is plotted to show the relationship to ^{137}Cs concentration. ^{90}Sr was not detected in any of the samples at this site. Ground water occurs at 314 ft below ground surface.

Figure 37 shows the subsurface cesium and strontium concentration at well E13-3A adjacent to one crib of a six-crib facility that received a moderate volume of intermediate level, high-salt scavenged waste from 1956 to

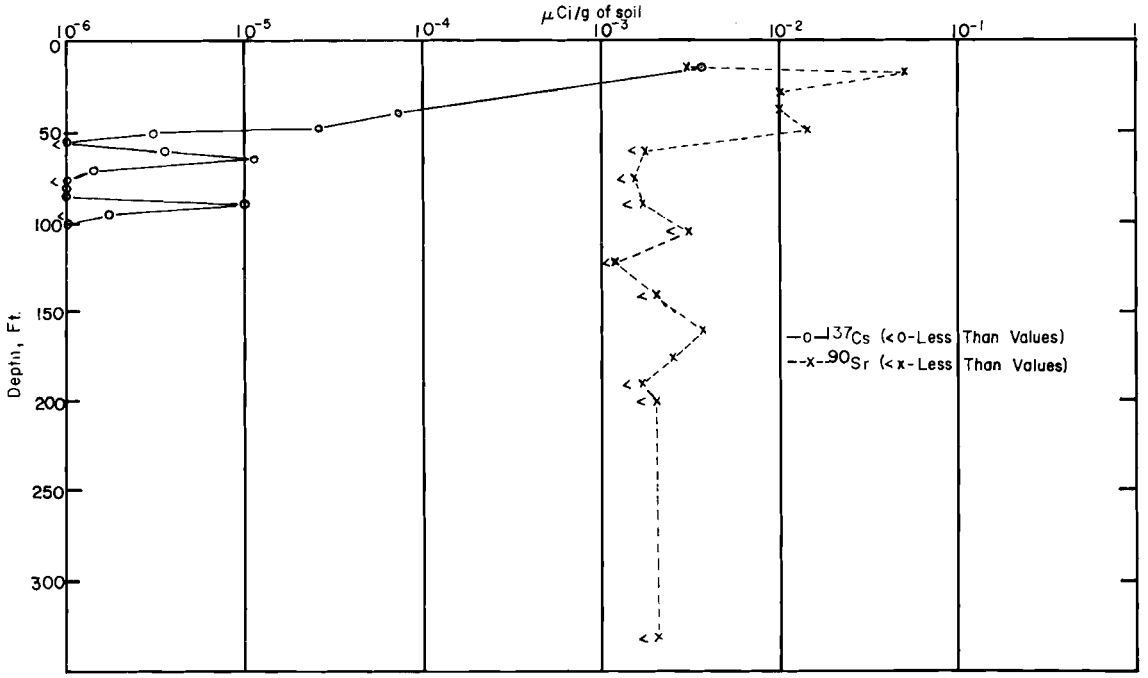

FIGURE 35. Well E33-2A Radioisotope Concentration

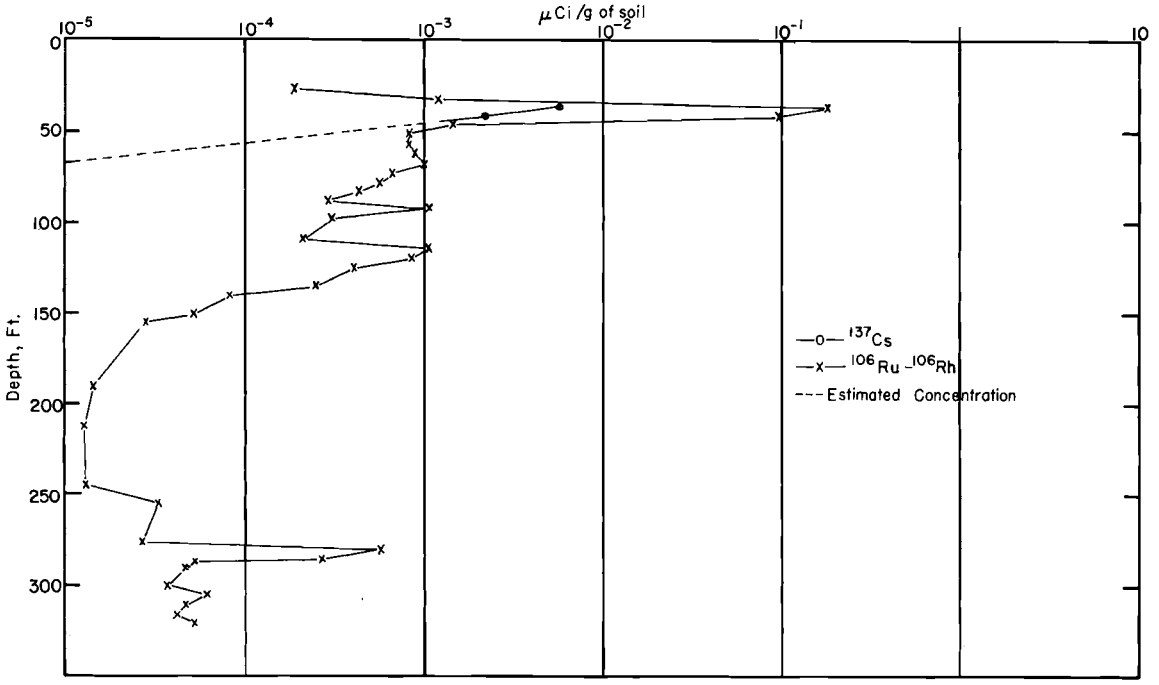

FIGURE 36. Well E24-1A Radioisotope Concentration

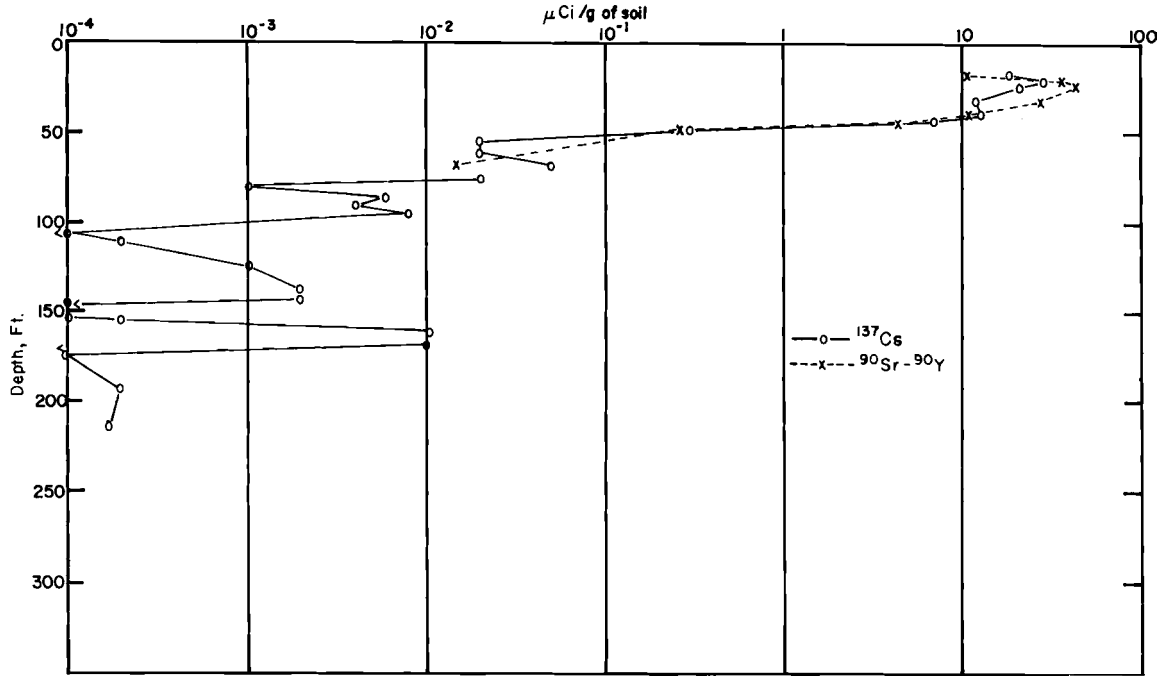

FIGURE 37. Well E13-3A Radioisotope Concentration

1957. Total disposal was 3.9 x 10' liters and 3.2 x 10^5 gross beta Ci, including 1560 Ci of ^{137}Cs and 1700 Ci of ^{90}Sr. Figure 37 shows that ^{137}Cs decreases rapidly from a moderate level of 3.5 x 10^{-3} µCi/g at 12 ft below ground surface to less than 1 x 10^{-6} µCi/g at 55 ft. Two minor concentration peaks of about 1 x 10^{-5} µCi/g occur at 65 and 90 ft. Cesium is below detection limits in the rest of the soil column. A ^{90}Sr high of 4.7 x 10^{-2} µCi/g occur at 65 and 90 ft. Cesium is below detection limits in the rest of the soil column. A ^{90}Sr high of 4.7 x 10^{-2} µCi/g occurs at 15 ft and drops to less than 1.8 x 10^{-3} µCi/g at 60 ft. ^{90}Sr concentration remains at about 2 x 10^{-3} µCi/g throughout the rest of the soil column. Ground water is 335 ft below ground surface at this location.

Data from waste disposal site field investigations generally support laboratory soil column studies which show that long-lived radioisotopes such as ^{137}Cs and ^{90}Sr are retained high in the column by adsorption and ion exchange. Essentially all of the cesium and strontium are stored some 100 ft or more above the water table.

PARTICLES AND GASES

APPLICATION AND PERFORMANCE OF A SPINNING DISC AEROSOL GENERATOR - G. A. Sehmel

A spinning disc aerosol generator was applied in studies of the turbulent deposition of monodisperse particles. Uranine and methylene blue solutions were used as the material to generate particles from 1 to 10 µ. Observations regarding the calibration and use of this instrument are reported. The relative humidity of the sweep air is an important factor in determining the final moisture content of the particles generated and it materially influences the physical quality of the particles. The spinning disc generator continued to prove its worth as a valuable tool in the study of behavior of particles in the 1 to 10 µ size range.

The spinning disc aerosol generator designed[51] and fabricated locally was used to generate particles for evaluation of particle deposition in long vertical conduits. The generator consists basically of a 1 in. diam disc driven by an air motor up to speeds of about 70,000 rpm. Alcoholic solutions of methylene blue and uranine are metered at about 0.7 ml/min through a number 22 hypodermic needle to the center of the disc. Droplets of this solution are formed at the spinning disc edge and evaporate in the air to form particles of controlled size. The particles are swept from the generator with filtered ambient air into a 7 ft^3 chamber from which the particles are drawn for experimental use.

During the course of this research the operating conditions were better defined and some of the limitations of the generator were determined.

Table VII. Typical Solution Concentrations

Particle Size, μ	Solute: Uranine, g	Solute: Methylene Blue, g	Solvent: CH_3OH, ml	Solvent: C_2H_5OH, ml	Disc Speed, rpm
1	0.026	0.014	5	995	64,000
2	0.19	0.093	30	970	67,000
4	0.50	0.27	90	910	35,000
6	0.58	0.28	100	900	23,000
10	0.90	0.48	300	700	20,000

The particle size was determined as a function of feed concentration and disc speed. Results of this calibration are shown in Table VII.

A cascade impactor was used to collect particles on an oil coated collector to spot check primary particle size. It was apparent that the particles would differ in moisture content as judged by the hardness and compressibility of the particles. If particles contained sufficient moisture, they would crystallize and lose their spherical form when collected on membrane filters. Dry particles, however, would remain spherical and "hard." Humidity of the ambient air was an important factor in determining whether particles would retain their shape after sampling. Particles would retain sphericity and appear "hard" and dry at ambient relative humidity of about 65%. On days when the humidity exceeded about 65% the particles would be soft and would crystallize after collection.

More detailed size distribution studies were made by sampling from the chamber on membrane filters during 5-hr generation periods. Samples were collected at times when dry particles were assured, hence detailed size measurements could be made. The particle size distribution of several samples is shown as histograms in Figure 38. The size distributions are quite narrow. A small fraction of "satellite" particles is created from the tail of primary droplets upon leaving the spinning disc. For

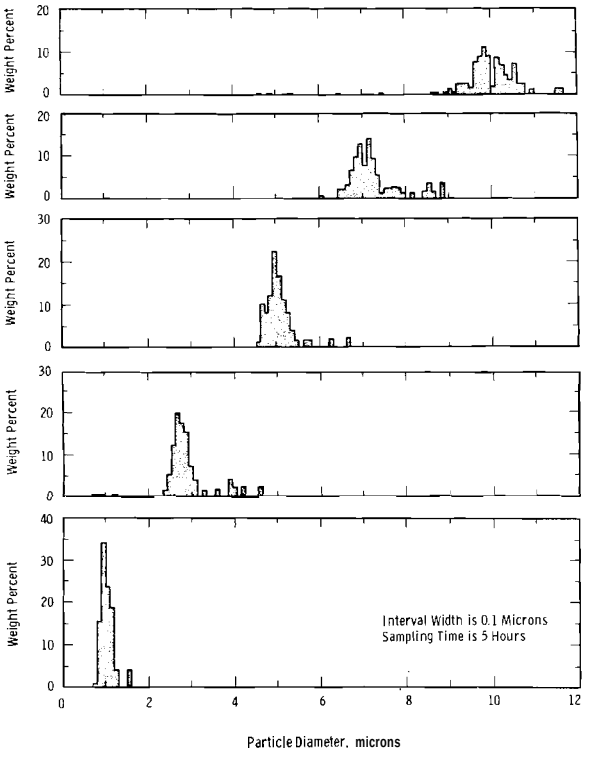

FIGURE 38. Typical Weight Frequency Histograms for Methylene Blue-Uranine Particles Produced by the Spinning Disc Aerosol Generator for Nominal Particle Diameters of About 1, 3, 5, 7, and 10 μ

the most part these are pulled out of the system and trapped before they can enter the main aerosol stream. Occasional aggregates of the primary particles are present. The size range should be narrowed for a shorter sampling period during which there would likely be less change in generator variables.

SUBISOKINETIC SAMPLING OF PARTICLES IN AN AIR STREAM - G. A. Sehmel

The errors associated with sampling at filter face velocities much below the carrying stream velocity (subisokinetic) were further studied. For relatively high approach velocities and when the filter face velocity is only a fraction of isokinetic, larger particles are collected primarily by impaction. Should the air concentration be computed from collected particles and flow volume through the filter, the indicated air concentrations will be much higher than the actual concentration. A relationship was established which permits reasonable estimates of corrections as a function of subisokinetic flow and the approach velocity. The relationship is based upon impaction data obtained for the filter. Data are shown for air velocities from 2.7 to 30 mph and particle sizes from 4 to 21μ

A representative sample of an aerosol-laden air stream is obtained only if the collected aerosol has the same size distribution and the same relative concentration as the air stream. Sampling under these conditions is termed isokinetic and requires that the sample be withdrawn parallel to the air stream flow and that the sample be withdrawn at an air velocity identical to that of the air stream. Sampling may be either remotely through a tube, as in a duct, or directly through a filter placed in the air stream. The latter is the case in atmospheric diffusion and washout studies[52] which have employed fluorescent ZnS as the tracer material. The ZnS is collected on filters located in the field and at several fixed flow rates from 0.3 to 4 ft/min which frequently are less than isokinetic (subisokinetic)—in some situations, far less.

When the sampling rate is subisokinetic, some air initially in the projected area upstream of the filter collector will be deflected around the collector. Larger and heavier particles will not be able to follow the air path and will impact on the filter. A nonrepresentative number of larger particles will be collected. In the extreme case all large particles approaching the collector in a cylinder of air of diameter equal to the filter diameter would be caught on the filter regardless of the amount of air drawn through the filter. Very small particles will follow the air paths because of their very low inertia.

The purpose of this study was to establish correction factors for various particle sizes and subisokinetic sampling rates for ZnS particles. The membrane filters and the polyethylene holders used in the local atmospheric

diffusion studies were to be employed in these measurements. The filter holder consists of a polyethylene filter support and its components: a base with its cup-like cavity, a backing for the filter, the membrane filter, and a retaining ring to seal the filter edge. The backing consists of a strip of crepe paper continuously wound around a central wooden dowel about 1/2 in. diam.

Theory can be used to set up the generalized dimensionless equation of motion for particles. That is,

$$\mathrm{Stk}\,\frac{d^2\vec{\psi}}{d\tau^2} + \frac{d\vec{\psi}}{d\tau} = \vec{V}_o(\psi) \qquad (1)$$

in which the dimensionless coordinate of the particle is $\vec{\psi} = \frac{\vec{r}}{R}$. R is the radius of the filter, $\vec{V}_o(\psi) = v/v_\infty$ is the dimensionless fluid velocity as a function of the dimensionless fluid velocity as a function of the dimensionless particle coordinate, v_∞ is the undisturbed air stream velocity, $\tau = \frac{V_\infty t}{R}$ is the dinlensionless time, and Stk is the Stokes number defined by

$$\mathrm{Stk} = \frac{\rho_p d^2 v_\infty}{18\mu R} . \qquad (2)$$

The Stokes number contains the physical properties of the system: the particle density, ρ_p; particle diameter, d; air viscosity, μ; and filter radius, R. In theory, integration of Equation (1) would yield the outer most trajectories of particles which would be collected on a filter and thus the sampling error problem would be solved. Unfortunately, the air flow patterns are unknown, and the required integration could not be performed.

For particle impaction on a filter, the correlating parameter for various particle sizes is the Stokes number, Stk, for any air velocity since similarity exists between aerosol systems, and Equation (1) is applicable. The Stokes number is related to the stop distance, S, defined as the distance a particle with an initial velocity, u_o, would travel in the horizontal direction in a still gas before coming to rest. For particles obeying Stokes law, the Stokes number is the ratio of the stop distance divided by the filter radius. For particles with Reynolds numbers as high as 18, the particle. drag coefficient is more highly dependent on Reynolds number than indicated by Stokes law, and hence the Stokes number is greater than the ratio of the stop distance divided by the filter radius. In the range of stop distances of interest, the variable drag is important. For example, the Stokes stop distance is 1.6 times the true stop distance for a 20 μ ZnS particle initially in a 30 mi/hr air stream. Adjusted Stokes numbers were calculated by dividing the true stop distance by the filter radius. The adjusted Stokes numbers are used as the correlating parameter for impaction data.

The experimental measurement of the sampling error involves introducing the particles into an air stream circulating in a closed loop duct at a given velocity. Within the duct are two adjacent collectors: one filter sampling at an isokinetic flow rate and the second sampling at a subisokinetic flow rate. After sampling is

complete, the number of particles in several size increments is determined microscopically for the two filters. The quantity, N/N_o, for a given particle size is determined. N_o is the number of particles collected for a given size range on the isokinetic sample; N is the number found of the same size on the subisokinetic sample. If there is no error in the sampling method, this ratio should be identical to the ratio of the air flows through the subisokinetic filter, u, to the air flow through the isokinetic filter, u_o. The factor by which the concentration ratio

$$\frac{C}{C_o} = \left(\frac{N}{N_o}\right)\left(\frac{u_o}{u}\right) \qquad (3)$$

exceeds one is the correction (divisor) to be applied to the apparent air concentration, C, determined from a subisokinetic sample to obtain the true air concentration, C_o.

As lower and lower ratios of $\frac{u}{u_o}$ are used, the fraction of particles collected eventually becomes equal to the impaction efficiency, defined as the number of particles collected of those approaching the filter in an area equal to the cross section of the filter, when the flow through the filter is zero. The experimental impaction efficiencies,[53] a_{u_o}, are shown in Figure 39 for air speeds from 2.7 to

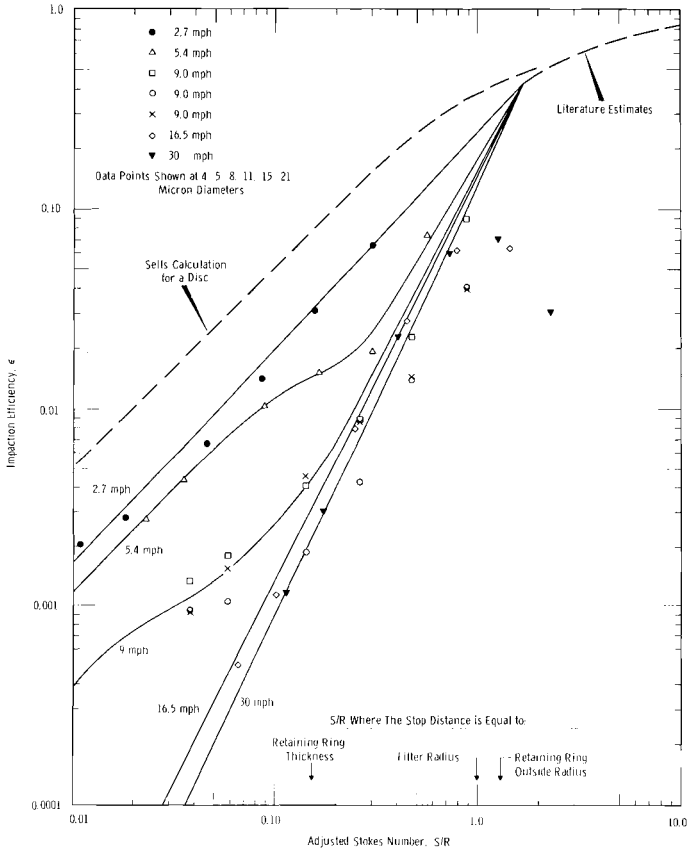

FIGURE 39. Inertial Deposition of Particles on Filters as a Function of Windspeed

30 mi/hr. For finite sampling rates the assumption is justifiably made that the particles in the air drawn through the filter would be collected with an efficiency of 1.0 In contrast, the collection of particles from the deflected air would be determined by an inertial impaction efficiency. For a given approach velocity one might approximate the actual impaction efficiency for particles in air not passing through the filter by using actual impaction efficiency a_{u_o} for this approach velocity. Thus, an expression for the ratio of particles collected by sampling at a face velocity, u, when the approach velocity is u_o might be expected to be

$$\frac{N}{N_o} = \frac{u}{u_o} + \alpha_{u_o}\left(1 - \frac{u}{u_o}\right) \qquad (4)$$

in which $\frac{u}{u_o}$ represents a fraction of particles collected in the volume of air passing <u>through</u> the filter. The second term, $\alpha_{u_o}\left(1 - \frac{u}{u_o}\right)$, represents the fraction of particles ccllected by impaction from the air which approaches the filter but is deflected around the filter holder.

The experimental and calculated collection ratios from the above equation are shown in Figure 40 for a 9 mi/hr windspeed. Similar types of curves were obtained for windspeeds of 2.7, 5.4, 16.5, and 30 mi/hr. As may be seen from the figure, we could not accurately support experimentally nor theoretically the assumption that for all sampling rates the impaction efficiency from the deflected air will remain constant for particles of a given size at a given approach velocity, u . The data obtained in this study, however, agree better with the assumptions stated above than with other theories proposed. Even so, considerable difference between experimental corrections and those predicted from this simple model do exist. These differences are believed to result from the inherent difficulties in achieving accurate particle sizing and counting, achieving uniform particle distribution in the air, and achieving flow patterns meeting the assumptions.

One of the early observations in this study, for example, was that the particle deposit on the subisokinetic filters was frequently not uniform, although generally symmetrical. Visual examination of many filters showed a general relationship between the appearance of the deposit and flow conditions prevailing during sampling. A regime of windspeeds and sampling rates exists within which heavy collection occurs near the periphery of the filter. Outside these combinations of windspeeds and sampling flows the particle collection is uniform from the edge of the 1/2 in. diam low-flow center area to the edge of the retaining ring. These conditions are shown in Figure 41. A transition region identifies a band of conditions within which collection may show some intermediate or undifferentiated pattern. It is further recognized that each windspeed-sampling rate combination may be preferentially affecting larger particles present with respect to where on the filter they come to rest. These observations are evidences of the complex nature of the collection mechanisms during subisokinetic flow.

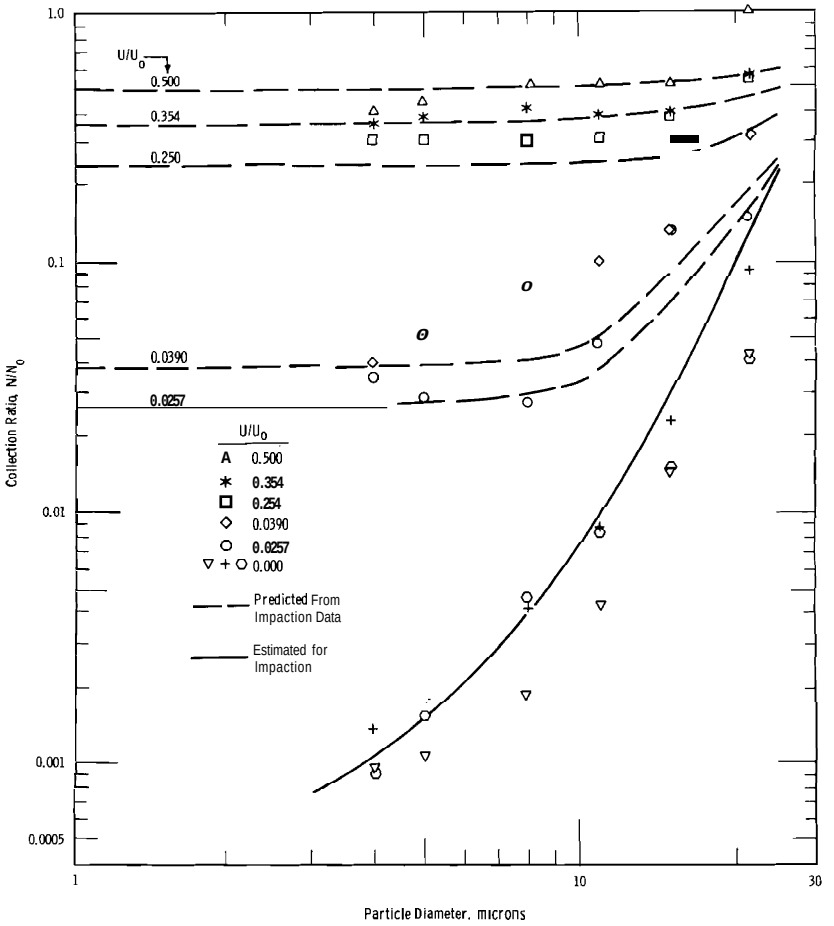

FIGURE 40. Collection Ratio for Each Particle Size as a Function of Sampling Ratio (U/U_o) for a 9 mi/hr Windspeed

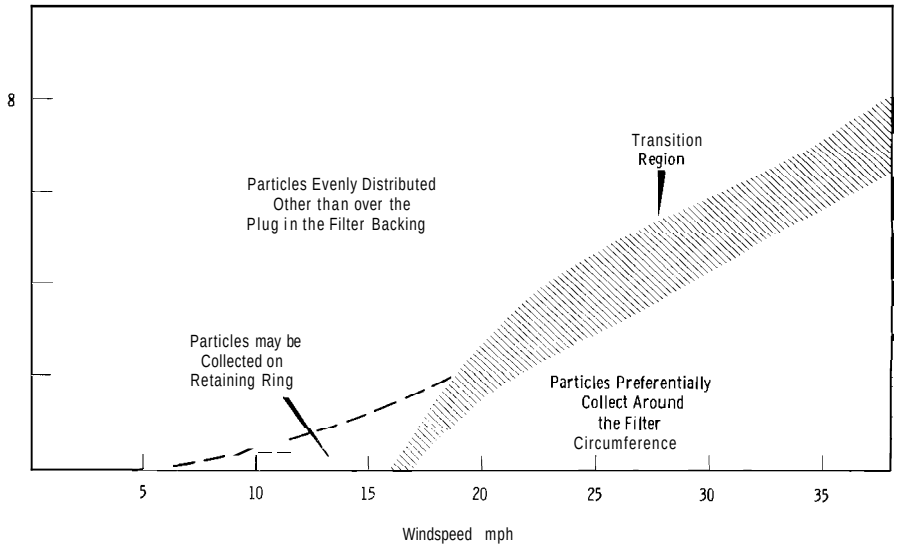

FIGURE 41. Effect of Velocities on Visually Determined Particle Distributions on Filter for Particle Size Distributions

Although the model used in this study is oversimplified since it is being applied to a collector of fairly complex geometry, it does, nevertheless, currently permit sampling errors to be estimated from Equation (5).

Values of the impaction efficiency α_{u_o} are those taken from the smoothed curves in Figure 40.

$$\frac{C}{C_o} = \left(\frac{N}{N_o}\right)\left(\frac{u_o}{u}\right)$$

$$= \left[\frac{u_o}{u} \cdot \frac{u}{u_p} + \alpha_{u_o}\left(1 - \frac{u}{u_o}\right)\right]$$

$$= 1 + \alpha_{u_o}\left(\frac{u_o}{u} - 1\right). \qquad (5)$$

ERRORS IN SAMPLING WITH NOZZLES DESIGNED TO ACHIEVE ISOKINETIC FLOW - G. A. Sehmel

Nozzles were used to obtain isokinetic samples of ZnS particles at air velocities from 5.4 to 30 mi/hr. Particle deposition on the nozzle walls was measured and is reported as the fraction deposited of those entering the nozzle. The deposition increased with particle size and velocity up to 70%.

To determine accurately the concentration and nature of an aerosol in an air stream one must sample isokinetically to assure a representative sample or have available the necessary correction factors to apply to samples obtained non-isokinetically. Sampling situations frequently arise in which a sample must be withdrawn from an air stream of relatively high velocity. When isokinetic sampling is attempted, it is quickly realized that the face velocity through the filter face held in the air stream can never be made to match the stream velocity because of the high pressure drop through the filter. In such cases a tapered inlet section preceding the filter has frequently been used. This transition section (nozzle) will theoretically allow a lower total flow through the filter and permit the isokinetic condition to be achieved at the inlet of the nozzle. Air at high velocity at the nozzle entrance will be slowed in the expanding section to a velocity at the filter face compatible with the permissible pressure drop through the filter. Sampling nozzles were required in recent studies of errors in subisokinetic sampling. It was soon found, however, that particle losses in the nozzles used would be significant. It is the purpose of this report to present the observations and conclusions regarding the use of these sampling nozzles.

Brass nozzles shown schematically in Figure 42 were used to obtain isokinetic samples of ZnS particles in a wind tunnel operating at air velocities ranging from 5.4 to 30 mi/hr. The larger exit end of the nozzle was sized for a press fit onto a polyethylene filter holder 1.6 in. diam at the filter face. The filter retaining ring was seated against a shoulder in the brass nozzle. A smooth unbroken surface wall surface

from nozzle inlet to the filter face was thus provided. Membrane filters of 0.8 μ pore size were used.

After each run the nozzle was carefully removed and visually examined using ultraviolet illumination of the fluorescent particles. This examination gave a qualitative estimate of the deposition pattern. Visual examination showed, for example, that at the lower flow rates used gravity deposition was significant and resulted in a heavier deposit on the lower portion of the nozzle. At higher flow rates turbulence becomes more important and particles appeared to be uniformly deposited throughout the nozzle.

The fraction and size distribution of particles collected on the wall were determined. The nozzle, after being gently removed, was replaced on the same filter holder into which had been inserted a fresh filter. Air was drawn through the filter and nozzle. Air from a small glass jet was played against the internal surfaces of the nozzle until all the particles were air-washed onto the filter. The internal surface of the filter retaining ring was considered part of the nozzle wall and was also air-washed onto the filter. Curing the air-washing, particles removed collected preferentially near the periphery of the filter and relatively few particles were collected in the central area of the filter. The particles on the filter were microscopically sized and counted. The fraction deposited on the walls of those initially entering the nozzle was determined by comparing the number of nozzle-deposited particles with the sum of particles found in the nozzle and on the original filter.

The fraction of particles deposited on the nozzle wall is shown in Figure 42 as a function of the upper limit of each of the seven ranges into which the particles were sized. The collection is a marked function of particle size; the larger particles are deposited to a much greater degree than the smaller particles. In the extreme case represented by the data as many as 70% of the particles were deposited on the walls. Particles smaller than 5 μ are not seriously deposited (< 1%) except for the highest flow rate used of 30 mi/hr.

This study emphasized the importance of errors which may be introduced through using nozzles preceeding a filter to achieve isokinetic flow.

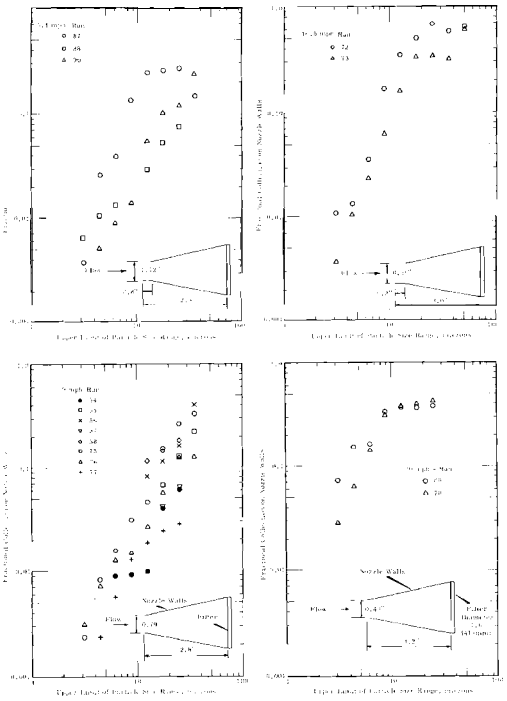

FIGURE 42. Collection of Particles on Nozzles at Isokinetic Entrance Velocities

PARTICLE DEPOSITION AND RE-ENTRAINMENT IN LONG VERTICAL CONDUITS—G. A. Sehmel

The deposition of 1- to 10μ diam particles was measured in vertical, 50-ft long aluminum tubes of 0.52, 1.15, and 2.81 in. I. D. Uranine-methylene blue particles of narrow size range generated with a spinning disc aerosol generator were used. Significant differences from earlier deposition data are believed to be due to the better resolution achieved with the nearly monodisperse particles from the spinning disc. The significantly lower density of the uranine-methylene blue particles than of particles used previously may also contribute to the apparent difference. The deposition ratio, K/V, is shown to be a more complex function of the "reduced stopping distance," S^+, than formerly indicated. Flow conditions which result in significant re-entrainment were identified and shown to be consistent with a conclusion that eddy fluctuations penetrate deeply into the laminar sublayer.

Representative samples from gaseous streams containing fine particles of radioactive materials are commonly required in plants which process nuclear materials. Since the sample delivery lines are usually unavoidably long, information on the impaction, deposition, and re-entrainment of these particles is required to interpret the sample results in terms of the concentration in the gaseous streams. Identification of the parameters controlling deposition on surfaces will also contribute to a better understanding of deposition of airborne particles on terrain and vegetation. The retention of particles on surfaces is also of interest in evaluating contamination spread and the degree of hazard from unusual incidents releasing appreciable quantities of radioactive aerosols.

It is the purpose of this study to determine the quantitative relationships among the variables governing particle deposition in conduits and to establish deposition models which are supported by the data.

Particle deposition is characterized by a deposition velocity, K, defined as the number of particles deposited per unit area per second per unit concentration in the gas over the surface. Particles carried in an air stream through a conduit are deposited on the walls to a degree depending upon the deposition velocity, tube length, diameter, the average velocity in the stream, and perhaps other variables. The deposition velocity may be calculated from a particle mass balance around the tube from the model,

$$\ln \frac{C}{C_o} = -4\left(\frac{K}{V_{av}}\right)\left(\frac{L}{D}\right) \qquad (1)$$

in which C is the average concentration of particles in the air at a distance, L, downstream of initial entering concentration, C_o; V_{av} is the average air velocity; and D is the tube inside diameter.

Deposition was measured by Friedlander and Johnstone[54] who predicted

that, in turbulent flow, the deposition ratio, K/V_{av}, should be a function of the particle reduced stopping distance

$$S^+ = \frac{d^2 \rho_p V_{av} \rho_g f}{40 \mu^2} \qquad (2)$$

in which

d = particle diameter
f = Fanning friction factor
V_{av} = average air velocity
μ = air viscosity
ρ_P = particle density
ρ_g = air density.

These authors developed equations to predict the deposition velocity. The equations required validity of the Reynold's analogy and that eddy diffusivity equations could be used to express mass flux of particles to within one stopping distance of the wall. The radial component of vel-city was assumed to carry the particle the remaining distance to the wall. Each of the relations required for the synthesis of the final equations for the deposition velocity was empirically derived from other workers' experimental observations. The resulting derived equations reflect the limitations, assumptions, and experimental uncertainties and interpretation of the earlier data. It is thus understandable that the equations developed for this complex phenomenon agree only qualitatively with the measurements of deposition velocity. Later deposition studies, nevertheless, have been interpreted making use of the equations of Friedlander and Johnstone with further empirical modifications to improve correlation.[55] The current work is an effort to establish firmly correlations which will permit reliable predictions of deposition under a wide range of conditions.

In the present study particle deposition was measured in 50 ft long vertical tubing of 0.62, 1.15 and 2.81 in. I. D. Long tubes were used to improve sensitivity and to permit identification and measurement of variables such as joint effects, which would not be apparent from data for single short tubes. The total length consisted of 12-ft or shorter sections of tubing which were carefully butted and clamped together within stiff rubber sleeves at the joints. Monodispersed uranine-methylene blue particles from a spinning disc generator[51] were passed into the tube and the particles passing through were collected on a filter. After a deposition experiment the tubing was cut into sections 1 in or longer and the internal surfaces were washed. The dissolved uranine was measured fluorimetrically, and Equation (1) was used to calculate the deposition velocity.

Data obtained in the current experiments are shown in Figure 43. A line best[56] representing the combined earlier data of Friedlander and Postma and Schwendiman[57] is also shown for comparison. The independent variable shown is S^+ as earlier defined, since to date this has permitted the best correlation notwithstanding the experimental data scatter. We note that the experimental methods employed in the current studies are more straightforward than any of the earlier methods.

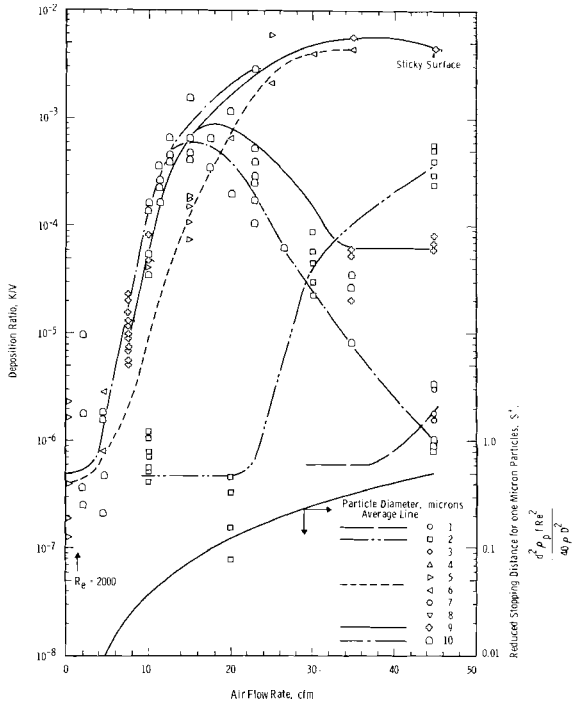

FIGURE 43. Deposition Ratio as a Function of Air Flow Rate for Methylene Blue-Uranine Particles in 1.152 in ID Vertical Tubes

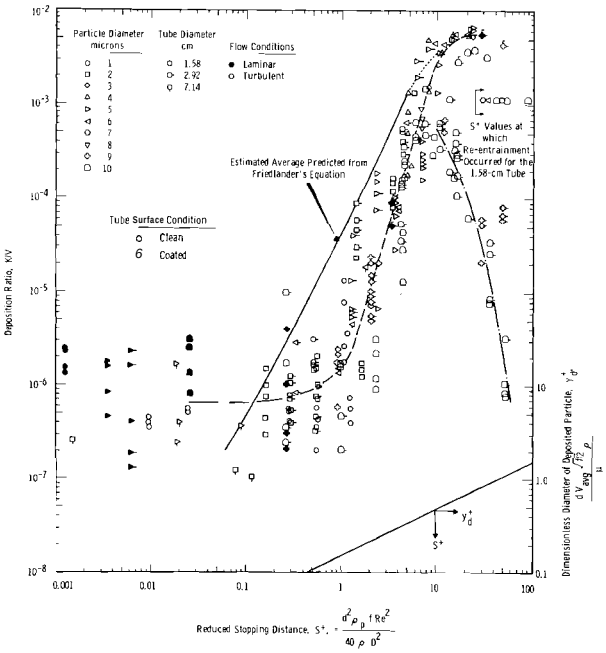

FIGURE 44. Deposition Ratio as a Function of one Correlating Parameter— the Reduced Stopping Distance

It is readily apparent that the current data differ from earlier reported data when S^+ is used as the correlating parameter. At an S^+ of about one, the current data yield a deposition ratio, K/V, of about 1/50 that of the earlier experiments. It may be significant that the particles used in the current study had a density of very nearly one, considerably less than particles previously used. A tenable conclusion is that the defined reduced stopping distance, S^+, may not represent the proper grouping of the variables involved, or may exclude a significant variable. The series of experiments included several conducted under flow rates deliberately chosen to permit re-entrainrnent. The net result was that the apparent deposition ratio, K/V, reached a maximum with S^+, then fell rapidly. The curves for 10μ particles in Figure 43 illustrate this.

Since rather inadequate correlations with S^+ were established for the current experiments taken as a group, the data for each diameter tube were considered separately. The deposition ratio, K/V, is shown as a function of flow rate and particle sizes for one tube size in Figure 44. The curves of deposition ratio for equal particle sizes show that particle deposition at equal turbulent flow rates increases until re-entrainment occurs. As shown, re-entrainment does not readily occur if the tube surface is made "sticky." In general the data for these curves for

individual tube diameters are more consistent than shown in Figure 43 and show expected trends. It was also found that when deposition ratios read from the smoothed curves were subsequently plotted against S^+, the inadequacies of S^+ as a correlating parameter became apparent. An improved correlation parameter beyond S^+ is needed which will more fully consider the effects of particle and tube properties upon any deposition velocity correlation.

To illustrate the magnitude of deposition and the conversion of deposition velocities to actual deposition, an air flow rate of 16 ft^3/min in a 1.15 in. I. D. tubing will be considered for uranine-methylene blue particles. Using the deposition ratios from Figure 44, the following throughputs were calculated from Equation (1)

THROUGHPUTS, C/C_o, AS A FUNCTION OF TUBE LENGTH

Particle Size μ	K/V	Tube Length, ft 10	50
2	4.8×10^{-7}	0.999	0.999
5.5	2.0×10^{-4}	0.92	0.66
10	1.1×10^{-3}	0.63	0.10

The throughput is seen to increase rapidly with increase in particle size and tube length. Experimentally, throughputs have been measured which are less than 1% in a 50 ft length of tubing.

Parameters determining the onset of re-entrainment were sought from the limited data. A significant conclusion was reached that, at the onset of re-entrainment, turbulent eddies must be penetrating deeply into the "classical" laminar sub-layer. The following consideration led to this conclusion.

The laminar sub-layer depth is generally conceded to be that distance from the tube wall which makes the dimensionless parameter, y^+, equal to 5, with y^+ defined by

$$y^+ = \frac{y\, V_{av}\, \rho_g \sqrt{f/2}}{\mu} \qquad (2)$$

in which y is the distance from the wall to the point being considered in the fluid.

A distance from the wall equal to the particle diameter, d_p, may be specified and expressed in terms of y^+; then,

$$d_p = \frac{y^+_{d_p} \cdot \mu}{V_{av}\, \rho_g \sqrt{f/2}} \qquad (3)$$

This relation is merely a statement that the dimensionless $y^+_{d_p}$ has been calculated at a position away from the wall equal to d_p. If d_p in this relation is substituted in Equation (2) for

$$S^+ = \frac{d^2 \rho_p V_{av}^2 \rho_g f}{40 \mu^2},$$

then an expression for $y^+_{d_p}$ follows:

$$y^+_{d_p} = \left[\frac{20 \rho_g S^+}{\rho_p}\right]^{1/2}. \qquad (4)$$

This equation permits the calculation of a $y^+_{d_p}$ corresponding to a distance from the wall equal to d_p in terms of a stated S^+. This relation is plotted at the bottom of Figure 43.

Re-entrainment was found to occur at S^+ values of about 10. From Equation (5), $y^+_{d_p} \cong 0.5$. The significance of this result is that a y^+ of 0.5 represents a point about 1/10 the distance from the wall to the boundary of the laminar sublayer ($y^+ = 5$). Unless turbulent eddies penetrate to within about one particle diameter, it is unlikely that the particles will be re-entrained. A necessary conclusion is that the laminar sub-layer must be frequently deeply penetrated by eddies with sufficient energy to re-entrain 10μ particles. From the data developed, a criterion for re-entrainment is that $y^+_{d_p}$ be greater than about 0.5. Others have concluded also that eddies penetrate the laminar sub-layer, (58) and the current data on onset of re-entrainment and its interpretation support this conclusion.

Although the use of monodisperse aerosols from the spinning disc generator has permitted a very straightforward experimental approach in these studies, the results confirm that deposition and re-entrainment are complex phenomena, sensitive to many variables, some of them very subtle in their effect. A consistent, definitive model supported by data for the several wide ranging variables is yet to be described.

AN ^{131}I GENERATOR FOR FIELD RELEASE STUDIES — L. C. Schwendiman

Studies of atmospheric dispersion and deposition of ^{151}I recuire a source which gives a steady evolution of the vapor form of the isotope over a selected period of time. The oxidation of I^- in acidified $NaNO_2$ was chosen as a suitable reaction to liberate iodine in the desired form. Steady evolution was obtained by metering iodide carrier and the tracer ^{131}I at a fixel known rate into an excess of the oxidizing agent which was continously sparged with N_2 or air. The sparging gas flow rate was selected so that the ^{131}I was released at a rate determined effectively by the transfer of the carrier and tracer to the reaction vessel. Although tracer level runs were successfully completed on a laboratory scale, a first attempt in a field dispersion study resulted in a partial release, which was traced primarily to plating of the high level spike during the waiting period onto the stainless steel walls of the reservoir, A second run with an all-glass reservoir was successful.

Several methods have been suggested and applied in studies requiring the release of molecular iodine. The solid element and several compounds containing iodine have been used, frequently by employing thermal decomposition. One of the limitations of most methods is the difficulty in controlling the rate of release which is an important requirement in dispersion experiments. Another qualification of a generator is that the ^{131}I released be molecular vapor with a negligible quantity associated with particles. Proper shielding and ease of manipulation in the field situation are other important considerations.

A generator designed to meet the requirements was studied in the laboratory. In principle, the generator system transfers the traced iodine as I^- at a fixed rate from a reservoir to a reaction vessel. In the reaction vessel the I^- is quickly and continuously oxidized to elemental iodine which is rapidly sparged from the vessel. Warmed air directed through and around the delivery nozzle insures that moisture carried out does not condense and eliminates retention of ^{131}I on the nozzle. Several oxidants might be used provided that the oxidation conditions would not result in higher valence states of iodine being formed. Sodium nitrite and sulfuric acid were chosen because it is known that I^- is effectively oxidized to I_2 by nitrous acid.

The concept of the generator was demonstrated in scouting studies by pumping an iodide solution traced with ^{131}I into a vessel containing 50 cm^3 of 0.1N $NaNO_2$ to which 2 ml of 6N H_2SO_4 was added just before the run. Dried and filtered air was bubbled through the solution at a rate either 3 or 5 liters/min. Essentially linear evolution of I_2 was shown by trapping the evolved iodine on a charcoal trap and continuously recording the radioactivity buildup. Iodine was evolved immediately at start-up; however, a few minutes were needed to reach the steady release rate. Similarly, near the end of the run a slight trailing was shown, as expected. The sparge-out rate was such that a half-time in the generator of about 30 sec was estimated. The rate is controlled primarily by the sparge rate since reaction is rapid in the excess of oxidant present.

Several experiments were later performed in the apparatus essentially as shown in Figure 45, but using a stainless steel reservoir with stainless steel ball valves. The ^{131}I as iodide

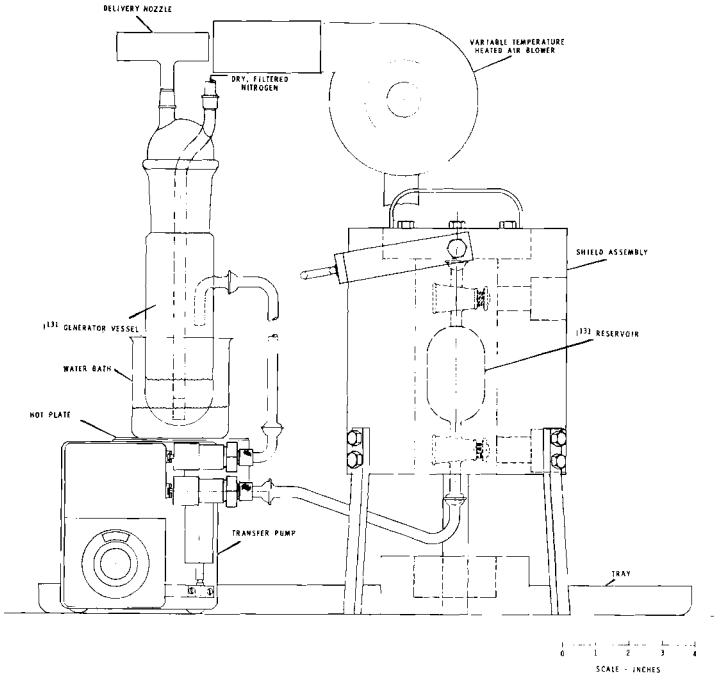

FIGURE 45. ^{131}I Generator

solution is pipetted into the shielded reservoir which is connected to the pump at the appropriate time. Small bore tubing with ballsocket connectors is used for the transfer lines. The valves can be opened through ports in the shield. A Beckman* piston pump, adjusted to deliver 2.0 ml/min, was used to transfer the iodide solution from the reservoir to the generator vessel. A medium frit bubbler was provided to insure good mixing and rapid flushing of the iodine generated.

These later experiments were in essential agreement with the scouting experiments, but suggested some changes to increase the rate of release after entry of the I^- into the vessel. Sparge rate was increased, the generation vessel was warmed in a water bath, and 0.3N $NaNO_2$ used with 10 ml 6N H_2SO_4.

The form of the iodine released was studied by taking samples with a Maypack** from a 45 liter aluminum aerosol chamber through which the generated ^{131}I was passed. Retention on the silver plated screen ranged from 78 to 96%; the remaining iodine was trapped on the charcoal paper and the charcoal bed. There was virtually no iodine associated with particles as judged by less than 0.3% of the iodine removed by the membrane filter preceding the silver plated screens. These experiments did not prove to be unequivocal tests for the iodine in the free atmosphere upon release from the solution; this is so because it was established that the aerosol chamber walls collected some iodine and later released it at a significant rate. The quantitative aspects of this interaction was not studied.

A field release experiment was conducted with the apparatus as described. A source of 2.8 Ci ^{131}I in 40 ml was delivered to the stainless steel reservoir with 5 mg I^- carrier and 10 mg of sodium bisulfite added to insure a reducing atmosphere. More than 2 weeks elapsed before the atmospheric conditions were favorable. The apparatus operated exactly as in the laboratory, yet only a fraction of the iodine appeared to have been released to the field grid. A negligible fraction remained in the generator vessel, a few millicuries in the delivery glass lines and pump. Over half was found through subsequent analyses to be retained on the walls of the stainless steel reservoir.

Preparations were expedited for a second release with glass reservoir substituted for the stainless steel. Fifty milligrams of carrier iodide and 50 mg of sodium sulfite were added, and the pH was adjusted to 8 to 10. Two releases were performed under field conditions using about 3 mCi in each to assure the success of the next full scale release. The iodine released was trapped in a Maypack at the nozzle outlet. In the first of the two runs in which the ^{131}I was delivered to 50 ml 0.3N $NaNO_2$ to which had been added 10 ml

---

* *Registered trade name of Beckman Instruments, Inc., Fullerton, Calif*

** *The Maypack is a collector made up of media in the following sequence: 1, membrane filter 2, four or more 200-mesh silver plated copper screens 3, charcoal impregnated filter paper 4, activated cocoanut charcoal.*

6N H_2SO_4, the radioactivity buildup on the Maypack leveled off at a radiation reading below that anticipated for 100% release. Virtually complete release was accomplished by adding assitional $NaNo_2$. A provision for delivering additional $NaNO_2$ remotely was made, a more concentrated $NaNO_2$ solution was used, and the second trial release of 3 mCi under field conditions was performed. The iodine release was linear with time and complete within about 2 min of the calculated spike pumping time. Some 25 ml of 1N $NaNO_2$ was added during the last half of the run using a remote syringe and interconnecting plastic tubing.

Laboratory analyses of the Maypacks on which the ^{131}I was collected are shown in Table VI.

A field release of 1.92 Ci of ^{131}I was accomplished using conditions as nearly identical as possible to the second trial run described above. The run progressed as planned with transfer of the ^{131}I to the reaction vessel accomplished in 20 min and the release completed in 22 to 24 min.

^{131}I retained on the component parts of the system after the release was measured by washing and laboratory assay and found to be 40 mCi with a distribution as follows:

	mCi
Washed from pump	26
Residual on pump	∿5
Generator residual	4
Glass lines	∿0.4
Reservoir residual	5
	∿40

Experience gained in this study should be of considerable benefit in future dispersion and deposition studies. The method for releasing iodine was proven in principle and a set of conditions established for effective release. The method should be studied at greater length for full understanding of the kinetics of the system.

TABLE VIII. Maypack Analyses

Location	Run 1 ^{131}I(a), dis/min	Run 1 Percent	Run 2 ^{131}I, dis/min	Run 2 Percent
MP Filter	0.13 × 10^7	neg.	0.6 × 10^7	neg.
Silvered Screens	465 × 10^7	80.2	600 × 10^7	89.2
Charcoal Paper	8.4 × 10^7	1.5	16.8 × 10^7	2.5
Charcoal	106 × 10^7	18.3	56 × 10^7	8.3
	579.4 × 10^7	100.0	673 10^7	100.0

(a) Corrected to original assay time of the prepared ^{131}I source.

RELEASE OF NOBLE GASES FROM AQUEOUS SOLUTION* - A. K. Postma

Release rate of a dissolved noble gas from a pool of water is effectively governed by the transport rate through the liquid film adjacent to the air-water interface. A theoretical study which made use of the limited available data showed that a half-time of release may vary from about 7 to over 1000 hr for a pool 5 ft deep. Better definition of liquid film transport coefficients through experimental studies is required to better define the release rate.

The rate at which radioactive noble gas isotopes are released from pools of water is an important consideration in an accident analysis for nuclear reactors in which water is released from the confinement zone. Water used for emergency cooling in N-Reactor, for example, may contain significant quantities of these noble gases after flowing through channels containing failed fuel elements. Although the solubilities of xenon and krypton are relatively low, the discharge of this water to an open basin provides the potential for a significant ground level release and exposure to people downwind. The seriousness of the exposure depends to a large extent on the rate at which the dissolved gases escape from the water. For release rates corresponding to duration of release of many hours, the potential hazard is reduced by normal changes in wind direction which would afford dispersion over a wider area and lower downwind concentrations. High release rates would give rise to higher noble gas concentrations in the atmosphere and would result in a more serious situation.

An initial theoretical study was undertaken to establish the rate at which noble gas dissolved in water would escape when the partial pressure of the gas over the water was reduced essentially to zero.

From a mass transfer standpoint, the release of dissolved noble gas from aqueous solutions would be classified as an absorption problem involving a slightly soluble gas. The release rate from a water pool would be governed by the gas transport rate through a thin liquid film adjacent to the air-water interface, or equivalently, by the liquid film coefficient. The magnitude of the liquid film coefficient depends on the rate at which the surface layers are mixed with the bulk of the liquid. Thus, important factors would he pool geometry, flow rate, temperature difference between the liquid surface and the atmosphere, and surface disturbances caused by wind.

For a given basin or pool an accurate average liquid film coefficient can be obtained only through experimental measurements carried out on a similar basin. Since the scope of the study precluded experimental investigation, we estimated film coefficients from a rather few published small scale laboratory experi-

*Not charged to the Division of Biology and Medicine.

ments. Based on these few experiments, the liquid film coefficients in an open basin would be expected to fall between 0.1 cm/hr and 15 cm/hr.(59) For a basin having a constant depth of 5 ft and for the situation where there is no input or output of water, these liquid film coefficients correspond to release half-times of 1070 hr and 7 hr, respectively.

Although these estimates leave a wide margin for error, the investigation showed that the release may be slow enough to effectively reduce the potential for serious consequences from a ground level release of noble gases from a pool or basin. The very limited published data of direct application to this problem emphasizes the need for further experimental work.

REFERENCES

1. L. G. King. "Description of Soil Characteristics for Partially Saturated Flow." Soil Sci. Soc. Am. Proc., Vol. 29, pp. 359-362. 1965.

2. J. R. Philip. "Numerical Solution of Equations of the Diffusion Type With Diffusivity Concentration-Dependent," Trans. Faraday Soc., Vol. 51, pp. 885-892. 1955.

3. J. R. Philip. "Numerical Solution of Equations of the Diffusion Type With Diffusivity Concentration-Dependent. I." Australian J. Phys., Vol. 10, pp. 29-42. 1957.

4. J. R. Philip. "The Theory of infiltration: %. The Profile at Infinity." Soil Sci. Vol. 83, pp. 435-448. 1957.

5. L. G. King. "Horizontal Infiltration of Liquids into Porous Solids." (This Report)

6. L. G. King. "Prediction of Vertical Infiltration as Influenced by Errors in Measuring Capillary Pressure." (This Report)

7. R. W. Nelson. "A Sequence for Predicting Waste Transport by Ground Water," A. E. C. Research and Deve Zopment Report BNWL-63. April, 1965.

8. R. W. Nelson. "Stream Functions for Three-Dimensional Flow in Heterogeneous Porous Media." Proc. XIII General Assembly International Union of Geodesy and Geophysical Section of International kssn. of Scientific Hydrology, Pub. No. 64, p. 290, Berkeley, 1963.

9. R. W. Nelson. "Steady Darcian Transport of Fluids in Heterogeneous Partially-Saturated Porous Media - Part I Mathematical and Numerical Formulation, HW-72335 PT I. January 16, 1962.

10 A. E. Reisenauer, R. W. Nelson, and C. N. Knudsen. Steady Darcian Transport of Fluids in Heterogeneous Partially-Saturated Porous Media - Part 11 The Computer Program, HW-72335 PT II. October, 2963.

11. A. E. Reisenauer. "Methods for Solving Problems of Multidimensional, Partially-Saturated Flow in Soils," J. Geophys. Res. 68, pp. 5725-5733. 1963.

32 A. E. Reisenauer. "Effects of Partially-Saturated Flow Parameters on Infiltration Rate." Hanford Radiological Sciences Research and Development Annual Report for 1962, HW-77609. January, 1963.

13. R. W. Nelson. "In-Place Measurement of Permeability in Heterogeneous Media. I. Theory of a Proposed Method," J. Geophys. Res., vol. 65, No. 6. June, 1960.

14. R. W. Nelson. "In-Place Measurement of Permeability in Beterogeneous Media. II. Experimental and Computational Considerations," J. Geophys. Res., vol. 66, No. 8, August, 1961.

15. R. W. Nelson. "Conditions for Determining Areal Permeability Distributions by Calculation," Journal of the Society of Petroleum Engineers. September, 1962.

26. R. W. Nelson. The Permeability Integral - A Key to Measurement in Heterogeneous Porous Media. Hanford Radiological Sciences Research and Development Annual Report for 1964. A.E.C. Research and Development Report BNW-36. January, 1965.

17. R. W. Nelson. "Flow in Heterogeneous Porous Media. I. Darcian Description of Two-Phase Systems." Water Resources Research, Am. Geophysical Union, Vol. 2, 1966.

18. H. L. Frisch, V. A. Vysotsky, S. B. Gordon, and J. M. Hammersley. "Critical Percolation Probabilities (Bond Problem)" The Physical Review, 23, 123, No. 5, 1566-1567, 1961.

19. Stephen Prager. "Viscous Flow Through Porous Media," Physics of Fluids, 4, No. 12, 1477-1482, 1962.

20. M. K. Hubbert. "Darcy's Law and The Field Equations of The Flow of underground Fluids," Trans. Amer. Inst. of Mining and Metallurgical and Petrol. Engnrs., 207, 222-239. 1956.

21. R. W. Nelson. "Flow of Fluids in Heterogeneous Porous Media. I. Darcian Type Description of Two-Phase Systems." Water Resources Research, Vol 2. 1966.

22. G. R. Frysinger and H. C. Thomas. Absorption Studies on Clay Minerals. VII. Yttrium-Cesium and Cerium (III)-Cesium on Montmorillonites, Jour. Chem. Phys., Vol. 64, 224-228. 2960.

23. J. R. Lewis and H. C. Thomas, 1963. Adsorption Studies on Clay Minerals. VIII. A Consistency Test of Exchange Sorption in the Systems Sodium-Cesium-Barium Montmorillonite, Jour. Phys. Chem., Vol. 67, 1781-1783.

24. P. F. Kerr, M. S. Main, and P. K. Hamilton, 1950b, Occurrence and Microscopic Examination of Reference Clay Mineral Specimens, U.S. Am. Petroleum Inst., Project 49. Clay Mineral Standards Preliminary Report No. 5: New York, Columbia University Press.

25. T. Tamura and D. G. Jacobs, 1960. Structural Implications in Cesium Sorption, Health Physics, Pergamon Press, Vol. 2, 391-398.

26. G. E. Boyd, A. W. Adamson, and L. S. Myers, 1947. The Exchange Absorption of ions from aqueous Solutions by Organic Zeolite: II. J. Am. Chem. Soc. 67: 2836-2848.

27. F. Helfferich, 1962. Ion Exchange. McGraw-Hill Book Co., Inc., New York.

28. J. Keay, and A. wild, 1961. The Kinetics of Cation Exchange in Vermiculite, Soil Sci. 92: 54-60.

29. C. E. Marshall, 1964. The Physical Chemistry and Mineralogy of Soils, Vol. 1: Soil Materials. John Wiley & Sons, Inc., New York.

30. W. A. Bassett, 1963. The Geology of Vermiculite Occurrences. Clays and Clay Minerals, Vol. 12: 61-69.

31. M. L. Jackson, 1956. Soil Chemical Analysis-Advanced Course. Published by the Author. Madison, Wisconsin.

32. L. L. Ames, 1963. Mineral Reaction Work at Hanford. The Use of Inorganic Exchange Materials for Radioactive Waste Treatment. U.S. AEC, TID-7644.

33. W. Jost, 1960. Diffusion in Solids, Liquids, Gases, Academic Press, Inc., New York.

34. J. V. Smith. "Structural Classification of the Zeolites", Mineral. Soc. of Am. Special Paper 1, p. 288. 1963.

35. L. L. Ames, Jr. 'Zeolite Cation Selectivity", Canadian Mineral., Vol. 8, pp. 325-333. 1965.

36. R. M. Barrer and W. M. Meier. "Exchange Equilibria in a Synthetic Crystalline Exchanger', Trans. Faraday Soc., Vol. 55, p. 130-141. 1959.

37. R. M. Barrer and D. C. Sammon. "Exchange EquiZibria in Crystals of Chabazite", Jour. Chem. Soc. London, pp. 2838-2849. 1955.

38. J. V. Smith. "Crystal Structures With a Chabazite Framework. Part V. Interpretation of Physiochemical Properties in Terms of Crystal Structure", Jour. Chem. Soc. London, pp. 3759-3770. 1964.

39. R. M. Barrer and W. M. Meier. "Structural and Ion Sieve Properies of a Synthetic Crystalline Exchanger", Trans. Faraday Soc., Vol. 54, pp. 1074-1085. 1958.

40. L. L. Ames, Jr. "Some Zeolite Equilibria with Alkaline Earth Metal Cations", Am. Mineral, Vol. 49, pp. 1099-1110. 1964.

41. H. Hoss and R. Roy. "Zeolite Studies. I. Synthesis and Stability of the Calcium Zeolites", Jour. Geol., Vol. 68, pp 41-53. 1960.

42. A. Steiner. "Hydrothermal Rock Alteration at Wairakei, New Zealand", Econ. Geol.. Vol. 48, pp. 1-3. 1953.

43. A. Steiner. "Wairakite, Ca-analog of Analcime, a New Zeolite Mineral", Mineral. Mag., Vol. 30, pp 641-698. 1955.

44. R. M. Barrer. "Ion-Exchange and Ion-Sieve Processes in Crystalline Zeolites, Jour. Chem. Soc. London, pp. 2346, 2350. 1950.

45. W. H. Taylor. "The Structure of Analcite ($NaAlSi_2O_6$)", Zeits. fur Krist., Vol. 74, pp 1-19. 1930.

46. D. S. Coombs. "X-ray Observations on Wairakite and Noncubic Analcime", Mineral Mag., Vol. 30, pp 699-708. 1955.

47. G. R. Dutt. Quality of Percolating Waters No. 2. Water Resources Center Contribution No. 50, Department of Irrigation, University of California, Davis.

48. R. B. Banks and S. Jerasate. Dispersion in Unsteady Porous Media Flow. J. Hydraulic Div., Proc. Am. Soc. Civil Engineering, May 12, 1962.

49. H. S. Carslaw and J. C. Jaeger, Oxford University Press, London, 2nd. Ed., 1959. P. 388.

50. J. L. Nelson. Soil Column Studies with Radiostrontium. II Effects of Soil Column Length and Diameter, HW-63930. Feb. 15, 2960.

51. L. C. Schwendiman, A. K. Postma and L. F. Coleman. "A Spinning Disc Aerosol Generator." Health Physics. Vol. 10, pp 947-53 (1964)

52. R. J. Engelmann. Rain Scavenging of Particulates, HW-79382, December 1, 1963.

53. G. A. Sehmel. Subisokinetic Sampling of Particulates in an Air Stream, BNWL-217. March 1, 1966.

54. S. K. Friedlander and H. F. Johnstone. "Deposition of Particles from Turbulent Gas Streams," Ind. Eng. Chem., Vol. 49, p. 1152, (1957)

55. L. C. Schwendiman, G. A. Sekmel, and A. K. Postma. Radioactive Particle Retention in Aerosol Transport Systems, International Conference on The Radioactive Pollution of Gaseous Media, Saclay, France, November 12-16, 1963, HW-SA-3210. October, 1963.

56. G. A. Sehmel and L. C. Schwendiman. The Turbuzent Transport and Deposition of Particles Within Vertical Tubes, Eighth AEC Air Cleaning Conference, Oak Ridge, Tennessee, October 22-25, 1963, HW-SA-3183. 2963.

57. A. K. Postma and L. C. Schwendiman. Studies in Micromeritics, I. Particle Deposition in Conduits as a Source of Error in Aerosol Sampling, HW-65308, May, 1960.

58. M. Corn and F. Stein. "Re-entrainment of Particles From a Plant Surface," American Industrial Hygiene Association Journal, Vol. 26, p. 325 (1966).

59. A. K. Postma. "Release of Noble Gases From Aqueous Solutions", BNWL-CC-484, January, 1966.

DISTRIBUTION

Number of Copies

325 Division of Technical Information Extension

1 AIF Task Force
MPR Associates, Inc.
815 Connecticut Ave. NW
Washington D. C. 20006

1 Air Force Cambridge Research Laboratory
Bellford, Massachusetts
D. A. Hargen

1 Atomic Energy of Canada Limited
Chalk River, Ontario
C. A. blawson

2 Atomic Energy Establishment Trombay
Bombay 73, India
P. N. Krishnamoorthy
K. T. Thomas

2 Atomic Energy Research Establishment
Harwell, Berks., England
R. H. Burns
E. Glueckauf

Australian A.E.C.
Post Office Coogee
New South Wales, Australia
A. W. R. Wilson

Brookhaven National Laboratory
L. P. Hatch

Center for Nuclear Studies
P. O. Box 6, Fontenay-aux-Roses
(Seine) France
A. de Calmes

Center for Nuclear Studies
P. O. Box 2, Saclay
Gif-sur-Yvette (S & 0), France
F. Duhamel
A. Menoux

Number of Copies

2 Douglas United Nuclear
T. W. Ambrose
P. C. Jerman

2 duPont Company
Aiken, South Carolina
W. B. Scott

1 duPont Company
Wilmington, Delaware
V. R. Thayer

1 ENEA (OECD) Health and Safety Office
38, Blvd. Suchet,
Paris XVI, France
E. Wallauschek

Eurochemic Library
Mol, Belgium

2 General Electric Company
M. C. Leveritt
R. T. Trumbull

General Electric Company
Advanced Technology Laboratories
1 River Road Schenectady 5, New York
J. W. Healy-Consultant Technical Hazards

Geological Survey of the United Kingdom
Water Division
Stevenson Buchan, Chief Geologist

Geological Survey of the United States
Washington 25, D. C.
M. King Mubbert
C. V. Theis

George Washington University
Washington, D. C.
C. R. Naeser

Geotechnical Corporation
Box 28277, Dallas 28, Texas
W. B. Heroy

DISTRIBUTION (Contd)

Number of Copies	
1	Gesellschaft Kernforschung mbH Karlsrhue 5 West Germany Dr. H. Krause
2	Hanford Occupational Health Foundation W. D. Norwood P. A. Fuqua
2	International Atomic Energy Agency Vienna 1, Kaerntnerring 11, Austria H. Seligman J. Servant
3	Isochem, Inc. R. E. Tomlinson R. Hill D. J. Brown
1	Johns Hopkins University Baltimore, Maryland W. A. Patrick
2	Lawrence Radiation Laboratory Livermore, California G. H. Higgins J. B. Knox
2	National Institute of Radiological Sciences 250, Kurosuna-Cho, Chiba-shi, Japan M. Saiki M. Suzuki
2	N. V. Belchim 200 Boeretang Mol, Belgium Paul Dejonghe Leo H. Baetsle
9	Richland Operations Office J. T. Christy J. P. Derouin P. G. Holsted C. L. Robinson R. K. Sharp (2) Technical Information Library (2) R. D. Wildman

Number of Copies	
2	Oak Ridge National Laboratory K. Z. Morgan E. G. Struxness
1	University of Arizona Tucson, Arizona Department of Geology E. S. Simpson
1	University of California Berkeley, California Department of Civil Engineering W. J. Kaufman
1	University of Illinois Department of Agronomy M. B. Russell
1	University of North Carolina Chapel Hill, N. C. Department of Chemistry H. C. Thomas
1	University of Wisconsin Department of Chemistry H. Gladys Swope
9	U. S. Atomic Energy Commission Washington. D. C. Division of Biology and Medicine N. F. Barr H. D. Bruner W. D. Claus C. L. Cunham, Dir. H. Hollister A. W. Klement S. A. Lough J. R. Totter J. N. Wolfe
1	Division of Naval Reactors R. S. Brodski
1	Division of Production W. L. Lennemann
1	Division of Reactor Development W. G. Belter

DISTRIBUTION (Contd)

Number of Copies

1 Health and Safety Laboratory
New York City
John Harley, Dir.

1 U. S. Atomic Energy Commission Savannah River Operations Office
K. K. Brown

1 U. S. Public Health Service
Division of Health Mobilization
Washington, D. C.
J. J. Lang, Research Branch

1 World Health Organization
Geneva, Switzerland
R. L. Dodson, M. D.

167 Battelle-Northwest
G. J. Alkire
F. W. Albaugh
W. J. Bair
C. A. Bennett
R. J. Brouns
L. J. Chockie
W. J. Clarke
R. F. Dickerson
R. L. Dillon (2)
W. L. Dotson
C. E. Elderkin
R. J. Englemann
S. L. Fawcett
E. H. Finney
R. F. Foster
P. A. Fuqua

Battelle-Northwest (Contd)

J. J. Fuquay(50)
J. K. Green (5)
W. A. Haney
J. F. Honstead
F. P. Hungate
E. R. Irish (50)
R. T. Jaske
R. L. Junkins
D. R. Kalkwarf
A. R. Keene
H. A. Kornberg
C. R. Lagergren
K. H. Larson
R. E. Nakatani
C. E. Newton
J. M. Nielsen
R. F. Palmer
H. M. Parker
R. S. Paul
D. W. Pearce
R. W. Perkins
I. C. Roberts
W. C. Roesch(6)
L. C. Schwendiman
W. G. Spear
C. L. Simpson
A. J. Stevens
M. F. Sullivan
R. C. Thompson
C. R. Tipton, Jr.
E. E. Voiland
M. T. Walling
W. E. Wilson
3. C. Worlton
Biology Library (21
Technical Information Files (5)
Technical Publications (2)